UNIVERSITY OF CALIFORNIA

Santa Barbara

Electrically Injected and Optically Pumped III-Nitride Devices for Polarized White Light Emission

A dissertation submitted in partial satisfaction of the requirements for the degree Doctor of Philosophy in Materials

by

Stacy Jean Kowsz

Committee in charge:

Professor Shuji Nakamura, Chair

Professor Steven P. DenBaars

Professor James S. Speck

Professor Umesh K. Mishra

June 2016

The dissertation of Stacy Jean Kowsz is approved.

_____

Steven P. DenBaars

_____

James S. Speck

_____

Umesh K. Mishra

_____

Shuji Nakamura, Committee Chair

June 2016

Electrically Injected and Optically Pumped III-Nitride Devices

for Polarized White Light Emission

by

Stacy Jean Kowsz

I dedicate this dissertation to my mom and dad

for instilling in me an interest in science

and for teaching me to be hard-working.

ACKNOWLEDGEMENTS

"If I have seen further, it is by standing on the shoulders of giants." –Isaac Newton

First, I'd like to thank my advisor, Professor Shuji Nakamura, with whom it has been an honor to work. Of course, I appreciate his support and contributions, without which this work would not exist, but what I admire most and hope to emulate in my own career is his predilection for saying "yes," which is empowering and enabling. I'd also like to acknowledge and thank my committee members, Professors Steve DenBaars, Jim Speck, and Umesh Mishra. In addition, I am grateful for guidance offered by Bob Farrell, Dan Cohen, Stacia Keller, Erin Young, and Danny Feezell.

"Alone we can do so little; together we can do so much." –Helen Keller

All the members of the III-nitrides community at UCSB have contributed to improving this work and me personally. I'd especially like to thank Erin Kyle, Matt Laurent, Ben Yonkee, David Hwang, Thomas Malkowski, Andrew Espenlaub, David Browne, Nathan Young, Dan Haeger, Brian McSkimming, Nathan Pfaff, John Haberstroh, and Christopher Pynn.

I would be remiss if I did not also thank the staff who trained me, taught me, helped me, and answered the phone when I still had more questions. This work could not have happened without the people who maintained and repaired the tools in lab. Thank you to all of the cleanroom staff, Tom Mates, Mark Cornish, the XRD lab staff, and the MOCVD lab staff.

"You are the sum total of everything you've ever seen, heard, eaten, smelled, been told, forgot—it's all there. Everything influences each of us, and because of that I try to make sure that my experiences are positive." –Maya Angelou

I would not be who I am today if not for the experiences I've had and the people I've known. I am thankful for the positive experiences enabled by the people I've called friends throughout my life. Grad school brought me to Santa Barbara, where I've met new friends. In particular, my life was made better by knowing John B., Chelsea, Myley, Greg, Robert, Sean, John E., Ellie, Karen, Martha, Roxana, Jessica, Michael, Justin, James, Lou, Kristin, Chance. Special thanks to Christopher for his love, support, forgiveness, and understanding. And I'd like to acknowledge Chikwindu, as he's been an important part of my life.

I'd also like to acknowledge having benefited greatly from the Technology Management Program and the people I met through TMP.

Last but most certainly not least, I thank my family for their support and the privileges that they've provided for me. Thank you, Mom, Dad, Erica, and Lynn.

VITA OF STACY JEAN KOWSZ
June 2016

EDUCATION

University of California, Santa Barbara
Doctor of Philosophy in Materials Engineering — June 2016
Advisor: Professor Shuji Nakamura
Dissertation Topic: Electrically Injected and Optically Pumped III-Nitride Devices for Polarized White Light Emission
Committee: Professors Shuji Nakamura, James S. Speck, Steven P. DenBaars, and Umesh K. Mishra
Master of Arts in Economics — June 2014
Certificate in Graduate Program in Management Practice — June 2016

Rochester Institute of Technology
Bachelor of Science in Chemistry — May 2010
Minor in Microelectronics and Nanofabrication

RESEARCH AND WORK EXPERIENCE

University of California, Santa Barbara
Materials Department
Solid State Lighting and Energy Electronics Center — Santa Barbara, CA
Graduate Researcher — September 2010–present

Applied Materials
Varian Semiconductor Equipment — Gloucester, MA
Ph.D. Intern — June–September 2015

Rochester Institute of Technology
Microsystems Engineering Department — Rochester, NY
Undergraduate Researcher — March–August 2010

Xerox Corporation
Organic Photoconductors Group — Webster, NY
Co-op — June–November 2009

Rochester Institute of Technology
Imaging Science Department — Rochester, NY
Undergraduate Researcher — December 2009–March 2010

Rochester Institute of Technology
Chemistry Department — Rochester, NY
Undergraduate Researcher — September 2008–March 2010

Pfizer Inc.
Pharmaceutical Sciences, Research Formulations — Groton, CT
Intern — June–August 2009

Rochester Institute of Technology
Biological Sciences Department — Rochester, NY
Undergraduate Researcher — September 2006–March 2008

TEACHING EXPERIENCE

University of California, Santa Barbara — April–June 2012
Materials Department/Department of Electrical and Computer Engineering
Teaching Assistant
Course: MATRL 215C/ECE 220C Semiconductor Device Processing with lab section
Instructor: Professor Shuji Nakamura

National Nanotechnology Infrastructure Network — June–August 2013
University of California, Santa Barbara
Research Experience for Undergraduates Mentor
Student: Eric Reichwein, University of California, Santa Cruz

PUBLICATIONS

- **S. J. Kowsz**, C. D. Pynn, S. H. Oh, R. M. Farrell, S. P. DenBaars, and S. Nakamura, "Using band engineering to tailor the emission spectra of trichromatic semipolar InGaN light-emitting diodes for phosphor-free polarized white light emission," submitted to Journal of Applied Physics (2016).
- **S. J. Kowsz**, C. D. Pynn, F. Wu, R. M. Farrell, J. S. Speck, S. P. DenBaars, and S. Nakamura, "Designing optically pumped InGaN quantum wells with long wavelength emission for a phosphor-free device with polarized white light emission," Proceedings SPIE 9748, Gallium Nitride Materials and Devices XI, 97481Z (February 26, 2016).
- **S. J. Kowsz**, C. D. Pynn, S. H. Oh, R. M. Farrell, J. S. Speck, S. P. Denbaars, and S. Nakamura, "Demonstration of phosphor-free polarized white light emission from monolithically integrated semipolar InGaN quantum wells," Applied Physics Letters **107**, 101104 (2015).
- L. Cao, A. Aboketaf, K. Narayanan, A. Elshaari, **S. Kowsz**, E. Freeman, S. McDermott, S. Preble, J. Bickford, and N. Bambha, "Direct observation of DC Kerr electro-optic modulation using silicon nanocrystals," Frontiers in Optics/Laser Science Technical Digest FTu1A.5 (2012).
- Merzlikine, Y. A. Abramov, **S. J. Kowsz**, V. H. Thomas, and T. Mano, "Development of machine learning models of β-cyclodextrin and sulfobutylether-β-cyclodextrin complexation free energies," International Journal of Pharmaceutics **418**, 207 (2011).

CONFERENCE PRESENATIONS

- **S. J. Kowsz**, C. D. Pynn, R. Farrell, J. S. Speck, S. DenBaars, and S. Nakamura, "Designing optically pumped InGaN quantum wells with long wavelength emission for a phosphor-free device with polarized white light emission," paper presented at SPIE Photonics West, February 2016, San Francisco, CA.
- **S. Kowsz**, C. D. Pynn, T. Margalith, R. Farrell, J. S. Speck, S. DenBaars, and S. Nakamura, "Progress towards a monolithic III-nitride device for polarized white light emission," oral presentation to be delivered at Materials Research Society Fall Meeting, November 2015, Boston, MA.
- **S. Kowsz**, E. Perl, J. Speck, S. DenBaars, and S. Nakamura, "Progress towards monolithic optically pumped and electrically injected III-nitride light emitting diodes," oral presentation at International Symposium on Compound Semiconductors, June 2015, Santa Barbara, CA.
- **S. J. Kowsz** and S. Nakamura, "Investigation of Eu-doping in InGaN grown by metal organic chemical vapor deposition," oral presentation at Electronic Materials Conference, June 2014, Santa Barbara, CA.
- **S. J. Kowsz** and M. L. Illingsworth, "Enabling the use of pendent polymers in optoelectronic devices," oral presentation at American Chemical Society's Undergraduate Research Symposium, April 2009, Rochester, NY.
- **S. J. Kowsz** and M. Savka, "Maize genotypes modulate quorum-sensing regulated virulence in Pantoea stewartii subsp. stewartii," poster presentation at Annual Meeting of the American Society of Plant Biology, June 2008, Merida, Mexico.

PATENTS

- **S. Kowsz**, R. Farrell, B. Yonkee, C. Pynn, T. Margalith, S. Nakamura, S. DenBaars, "Tunnel junction devices with monolithic optically-pumped and electrically-injected III-nitride layers," provisional US patent filed February 2016.
- **S. Kowsz**, R. Farrell, T. Margalith, C. Pynn, S. Nakamura, and S. DenBaars, "Device utilizing varying doping profiles to enable long wavelength emission from optically-pumped III-nitride layers," provisional US patent filed April 2015.
- **S. Kowsz** and S. Nakamura, "Optically-pumped and electrically-injected III-nitride light-emitting devices for white light," provisional US patent filed June 2014.
- K. T. Dinh, E. C. Savage, M. J. LiVecchi, R. W. Hedrick, L. L. Ferrarese, S. A. Toates, and **S. J. Kowsz**, "Binderless Overcoat Layer," US Patent 8883384 B2 filed September 2009.

ABSTRACT

Electrically Injected and Optically Pumped III-Nitride Devices for

Polarized White Light Emission

Stacy Jean Kowsz

Despite the advantages of growing III-nitrides on semipolar planes, challenges still remain for achieving long visible wavelength emission from InGaN layers. The growth of high indium content InGaN required for long wavelength emission is difficult to achieve. First, high indium content InGaN has a large lattice mismatch with GaN, and the large stress in strained InGaN layers acts as a driving force for relaxation. Second, high indium content InGaN layers require low growth temperatures or fast growth rates, which lead to decreased adatom diffusion and desorption and can result in increased impurity concentrations, a breakdown of surface morphology, and growth errors. Third, subsequent high temperature growth steps have been shown to degrade high indium content InGaN layers.

We report device designs in which an electrically injected blue light-emitting diode (LED) optically pumps quantum wells (QWs) with long wavelength emission. Optically pumping offers several advantages over electrically injecting QWs for long wavelength emission. Optically pumped QWs do not have to be confined within a *p-n* junction, and carrier transport is not a concern. Thus, thick GaN barriers can be incorporated between multiple InGaN QWs to manage stress. Optically pumping long wavelength emitting QWs also eliminates high temperature steps that degrade high indium content InGaN but are

required when growing *p*-GaN for an LED structure. Additionally, by eliminating electrical injection, the doping profile can instead be engineered to affect the emission wavelength.

A device that monolithically integrates a blue LED and optically pumped QWs for long wavelength emission can be optimized to emit white light. This is an alternative to white light created using blue or violet III-nitride LEDs or laser diodes to pump powdered phosphors that emit yellow or red wavelengths. In addition, white light created by nonpolar or semipolar InGaN QWs with varying bandgaps offers the benefit that the emitted light is optically polarized, compared to the unpolarized emission that results from *c*-plane LEDs, powdered phosphors, and scattered light. This is of significant interest because polarized light has unique applications in, for example, backlighting liquid-crystal displays.

We present demonstrations of electrically injected and optically pumped III-nitride device designs for polarized white light emission. A first device monolithically incorporated a blue $(20\bar{2}\bar{1})$ LED and yellow optically pumped $(20\bar{2}1)$ QWs. This device produced polarized white light emission with peaks at 440 nm and 560 nm from the electrically injected and optically pumped QWs, respectively, and an optical polarization ratio of 0.40. A second device monolithically incorporated a blue $(20\bar{2}\bar{1})$ LED and optically pumped $(20\bar{2}1)$ QWs for long wavelength emission, where the doping profile was intentionally engineered to red-shift the emission of one of the optically pumped QWs by creating a built-in electric field that acted in the same direction as the polarization-induced electric field in the QW. This device produced polarized white light emission with a peaks at 450 nm from the electrically injected QW and at 520 nm and 590 nm from the optically pumped QWs, which were grown in *n*-*i*-*n* and *p*-*i*-*n* structures, respectively. The optical polarization ratio was 0.30. A third device was grown on $(20\bar{2}1)$ using a tunnel junction to incorporate

optically pumped QWs for long wavelength emission above an electrically injected blue LED. Use of NH_3 molecular beam epitaxy enabled the growth of the tunnel junction in this device, while use of metalorganic chemical vapor deposition enabled the growth of InGaN with high radiative efficiency. By increasing the ratio of yellow to blue emission, future devices can be used to produce polarized white light. Our initial device produced emission peaks at 450 nm and 560 nm from the electrically injected and optically pumped QWs, respectively. The optical polarization ratio was 0.28. Overall, using electrically injected and optically pumped III-nitrides devices, we have demonstrated the first devices with polarized white light emission.

TABLE OF CONTENTS

Chapter 1

Introduction

1.1 III-Nitrides

1.1.1 Properties of III-Nitrides

III-nitride materials are direct bandgap semiconductors with bandgaps that span the visible spectrum. By changing the alloy composition, the bandgap of $In_xGa_{1-x}N$ can be tuned from 0.7 eV to 3.5 eV, the bandgaps of InN and GaN, respectively. One of the biggest challenges in realizing alloys that span this range is that there is a large lattice mismatch between GaN and InN, which produces stress in strained InGaN layers that are pseudomorphic with respect to the GaN on which they are grown. The hexagonal *a* and *c* lattice parameters of GaN are 3.186 Å and 5.186 Å, respectively, while the *a* and *c* lattice parameters of InN are 3.545 Å and 5.703 Å, respectively. Because InGaN layers of increasing indium content grown pseudomorphically on GaN are stressed, when the InGaN layer reaches a critical thickness, it becomes energetically favorable for defects to from that allow the InGaN layer to partially relax. The critical thickness of relaxation decreases as a function of increasing indium content.

InGaN layers coherently strained to GaN are further complicated by piezoelectric polarization. [1], [2] The III-nitride materials most commonly have the wurtzite crystal structure, which is non-centrosymmetric, making III-nitride materials piezoelectric with a polar *c*-direction. In addition, because the III-nitrides have a lower *c*/*a* ratio than the ideal

c/*a* ratio, these materials also have a spontaneous polarization. The total polarization in a layer is given by a sum of the spontaneous and piezoelectric polarizations. A sheet charge is induced at the interface between layers, with the magnitude of the sheet charge determined by the difference in the total polarizations of the layers that are adjacent at the interface. Ultimately, these sheet charges at interfaces produce electric fields in QWs, where the polarization-induced electric field can be decomposed into spontaneous and piezoelectric components:

$$E_{QW} = E_{SP,QW} + E_{PZ,QW} = \frac{P_{SP,B} - P_{SP,QW}}{\epsilon_{QW}} - \frac{P_{PZ,QW}}{\varepsilon_{QW}} \quad (1.1)$$

where E_{QW} is the electric field in a QW, $P_{SP,B}$ and $P_{SP,QW}$ are the spontaneous polarizations in the barrier and QW, respectively, $P_{PZ,QW}$ is the piezoelectric polarization in the QW, and ε_{QW} is the dielectric constant in the QW. Because the spontaneous polarization is approximately equivalent for InGaN and GaN, the electric field in an InGaN QW grown pseudomorphically on GaN is determined by the piezoelectric polarization. [3]

The magnitude and direction of piezoelectric polarization in the growth direction depends on the growth plane. [2], [3] The piezoelectric polarization in the growth direction is at a maximum for growth on the polar *c*-plane or –*c*-plane, which have opposite directions of the piezoelectric polarization. Piezoelectric polarization in the growth direction is absent for growth on the nonpolar *a*-plane or *m*-plane. Semipolar growth planes result in decreased piezoelectric polarization compared to growth on the polar planes. The advantages of different growth planes are further discussed in Section 1.1.2.

Because InGaN QWs have significant strain due to the large lattice mismatch between InN and GaN, there can be large piezoelectric polarization in InGaN QWs. The polarization-induced electric fields in InGaN QWs result in quantum-confined Stark effect

(QCSE). Electric fields produce a tilting of the energy bands that produce an accumulation of electrons close to one of the QW interfaces and an accumulation of holes at the opposite interface of the QW. This physical separation of the electrons and holes results in poor overlap of the electron and hole wavefunctions. This is problematic because radiative recombination depends on the overlap of the electron and hole wavefunctions. Additionally, a decrease in radiative recombination increases the carrier concentration corresponding to a given current density, which increases nonradiative Auger recombination at a given current density because Auger recombination dominates at high carrier densities, as it scales with the third power of the carrier density. [4]–[6]

Auger recombination is nonradiative recombination that results when and electron and hole recombine and instead of producing a photon, energy is transferred to excite a third carrier. Thus, the Auger recombination rate is represented by Cn^3 in the ABC model

$$An+Bn^2+Cn^3=R \tag{1.2}$$

where An is the Shockley-Read-Hall recombination rate, Bn^2 is the radiative recombination rate, and R is the total recombination rate. Auger recombination may occur via indirect processes, which are assisted by scattering. [4] Electron−phonon coupling is particularly strong in III-nitrides and can assist indirect Auger recombination. Alloy disorder results in reduced symmetry and alloy scattering, which can also contribute to indirect Auger recombination. Auger recombination is also detrimental to device performance because hot Auger electrons can escape the QW active region. Auger electrons that escaped the active region and relaxed to the L-valley have been measured by electron emission spectroscopy to experimentally confirm Auger recombination. [7]

An additional challenge with III-nitride materials is that it is difficult to dope for *p*-type materials. There are a lack of elements that act as acceptors. Magnesium is used as an acceptor, but because it is a deep acceptor with a state that is 170 meV above the valence band, only approximately 1 % of the acceptors are ionized at room temperature. [8] Another challenge is that Mg-doped layers grown by metalorganic chemical vapor deposition (MOCVD) are passivated due to the formation of a Mg−H complex. A post-growth anneal in a low hydrogen environment liberates hydrogen from the complex, but the Mg-doped layer must be exposed at the surface in order to successfully remove the hydrogen. This requirement constrains epitaxial device design.

Despite many challenges, the III-nitride materials system has been researched extensively for optoelectronic applications, including light-emitting diodes (LEDs) and laser diodes (LDs). One significant reason for the success of these light-emitting devices is that III-nitrides have been found to emit light despite threading dislocation densities on the order of 10^9 cm^{-2}. Such high threading dislocation densities would be catastrophic for light emission in other materials systems. It has been hypothesized that indium fluctuations in InGaN alloys result in carrier localization that prevents carriers from recombining nonradiatively at threading dislocations.

InGaN LEDs and LDs are commercially available today. These commercial devices are grown by MOCVD. MOCVD is a favorable growth technique for high throughput, and more importantly, MOCVD yields InGaN layers with high radiative efficiency compared to the low radiative efficiency of molecular beam epitaxy (MBE) InGaN layers, though the reason for the low radiative efficiency of MBE InGaN is still unknown.

1.1.2 III-Nitride Growth Planes

Currently available commercial devices are typically grown on the polar *c*-plane of wurtzite GaN. Because native substrates are expensive and of limited size, commercial devices are grown on sapphire or SiC substrates. However, if large area bulk GaN substrates become economically viable, they will offer several advantages. First, bulk GaN substrates offer reduced threading dislocation densities compared to GaN templates grown on sapphire or SiC. Second, bulk GaN substrates allow for growth on semipolar or nonpolar planes.

Devices grown on the polar *c*-plane of GaN are affected by large piezoelectric polarization-induced electric fields in strained heterostructures, as discussed in Section 1.1.1. [1] Growth on semipolar and nonpolar planes is of interest because these planes reduce or eliminate piezoelectric polarization-induced electric fields, which is advantageous for device performance. [2] Reducing the polarization-induced electric fields in InGaN quantum wells (QWs) allows for increased radiative recombination and decreased nonradiative Auger recombination, both of which can decrease efficiency droop and enable higher efficiencies at high current densities. [5] Increased radiative efficiency results from improved overlap between the electron and hole wavefunctions. Decreased Auger recombination results because higher radiative efficiency leads to lower carrier concentrations at a given current density, and Auger recombination is dominant at high carrier densities since it scales with the third power of the carrier density, as discussed in Section 1.1.1. [4]–[6] Additionally, the improved wavefunction overlap on semipolar and nonpolar planes enables wider QWs compared to *c*-plane, which can also serve to lower the carrier concentration at a given current density. [9] Research has demonstrated high performance nonpolar and semipolar LEDs and LDs. [10]–[12] In particular, semipolar and

nonpolar LEDs have demonstrated improved efficiency droop as a function current density compared to *c*-plane LEDs. [10]

As will be discussed further in Section 1.3, semipolar and nonpolar growth planes also enable optically polarized emission normal to the surface from InGaN QWs, compared to the optically unpolarized emission from *c*-plane InGaN QWs. [13]–[19] A further benefit of growth on semipolar planes is improved surface morphology compared to *c*-plane. Growth on *c*-plane is commonly afflicted by formation of V-defects, which are inverted hexagonal pyramid-shaped pits with $\{10\bar{1}1\}$ facets forming the sidewalls of the pits. V-defects can nucleate on preexisting threading dislocations and propagate outwards to increase in size with continued growth. [20]

Growing on semipolar planes does present new challenges compared to growth on *c*-plane. For example, oxygen incorporation has been found to be higher on semipolar planes compared to *c*-plane. Additionally, critical thickness of relaxation is plane dependent, with growth on semipolar planes having decreased critical thickness compared to *c*-plane, so growth on semipolar planes is constrained by the need for stress management to a greater degree than growth on *c*-plane. [21]

This decreased critical thickness of relaxation on semipolar planes compared to *c*-plane results because strained semipolar III-nitride layers have been observed to relax by the formation of basal plane misfit dislocations (MDs), which act to relieve the resolved shear stress on the *c*-plane. However, for growth on *c*-plane or nonpolar planes, there is an absence of resolved shear stress on the *c*-plane to act as a driving force for the formation of basal plane MDs. Experiments studying basal plane MD formation on semipolar planes have

been found to agree well with a Matthews-Blakeslee model of critical thickness of relaxation. [21]–[24]

Experimental results also report the onset of non-basal plane MD formation subsequent to the formation of basal plane MDs. [23], [25], [26] Although non-basal plane slip is thermodynamically favored, basal plane slip has been reported to be the primary observed mechanism of relaxation on semipolar planes, which results due to kinetic considerations that favor the formation of basal plane MDs. However, non-basal plane slip eventually occurs because it acts to relieve strain in a direction that is not relaxed by the formation of basal plane MDs.

Work has examined limited area epitaxy (LAE) as a technique to enable growth of coherent semipolar layers beyond the critical thickness of relaxation observed for planar growth. [27], [28] LAE involves patterning the substrate surface prior to growth so that physical boundaries limit the run length of MDs that form on the LAE device regions. [29] MDs in semipolar III-nitride materials have been shown to form by bend and glide of preexisting threading dislocations, as opposed to being formed by the generation of new threading dislocations and half loops that terminate at the surface. [24] Because MD formation requires preexisting threading dislocations, LAE also limits the number of MDs that form on LAE device regions by using physical boundaries to determine the number of threading dislocations (TDs) that can participate in MD formation. [27]

MDs can also be used to reduce the number of threading dislocations in device regions. By generating MDs, threading dislocations can be swept to the edge of LAE device areas or the edge of the substrate in the case of planar growth. Additionally, MDs enable intentional partial relaxation of device structures on semipolar planes. Other work has

explored relaxed buffer layers where devices are not affected by MDs that produce relaxation if they are formed far away from the active region. [30], [31]

1.1.3 Long Visible Wavelength Emission from III-Nitrides

By changing the alloy composition, the bandgap of InGaN can correspond to emission of any visible wavelength of light. Thus, white light emission can be achieved by creating a device with QWs that emit different wavelengths of light. However, long wavelength emission from the InGaN requires high indium content layers, which are challenging to achieve for multiple reasons. First, high indium content InGaN layers have a large lattice mismatch with GaN (as discussed in Section 1.1.1.), and when high indium content InGaN layers grown on GaN reach critical thickness, stress is relieved by a transition to 3D growth [32] or by the formation of extended defects at which nonradiative recombination occurs. [21] Second, the crystal quality of high indium content InGaN layers is also negatively impacted by the low growth temperatures that are required to increase indium incorporation. Low growth temperatures are necessary to decrease desorption of indium from the growth surface, but low temperatures that result in decreased adatom diffusion and desorption can lead to growth errors, breakdown of surface morphology, and higher impurity incorporation. [33], [34] Thus, low growth temperatures may produce defects at which carriers can recombine nonradiatively. Lastly, high indium content InGaN layers have a low thermal budget, as high temperature steps have been shown to degrade high indium content InGaN. [35], [36] This is problematic because LED structures have *p*-type GaN above InGaN QWs, and elevated temperatures are usually required to ensure adequate *p*-type conduction. [35], [37]

Increasing QW thickness is a technique that can be used to red-shift the emission wavelength while holding InGaN indium content constant. Increasing QW thickness decreases the energies of the bound states. However, like high indium content InGaN layers, thick QWs encounter problems with relaxation and material quality. Wide QWs can allow the growth of facets. [38]

Even when InGaN layers with long wavelength are achieved, the higher indium content and/or wider QWs have decreased electron and hole wavefunction overlap leading to decreased radiative recombination rates and increased nonradiative recombination rates. [5] Higher indium content InGaN results in decreased wavefunction overlap for QWs on polar and semipolar planes because piezoelectric polarization-induced electric fields increase with increasing InGaN indium content. [2] As radiative recombination decreases, carrier lifetime increases resulting in increased carrier concentration at a given current density. [5] Thus, longer wavelength emitting devices have higher carrier concentrations at a given current density, which results in increased nonradiative Auger recombination because Auger recombination dominates at high carrier densities since it scales with the third power of the carrier concentration, as discussed in Section 1.1.1. [4]–[6] Overall, InGaN QWs with increasing emission wavelength are expected to have decreasing efficiency.

1.2 White Light

1.2.1 Creating White Light

An additive color model explains the mixing and production of different colors of light. Red, green, and blue are the primary colors. Mixing two primary colors produces

secondary colors, which are cyan, magenta, and yellow. Mixing complementary colors or all three primary colors produces white. Because III-nitride alloys have bandgaps that span the visible spectrum, it is possible to create white light by combining emission from different InGaN layers. However, producing phosphor-free III-nitride white light is a challenge because it is difficult to achieve high indium content InGaN layers for long wavelength emission.

Commercially available white LEDs today typically combine a blue or violet InGaN LED pumping phosphors with emission at longer visible wavelengths. Most commonly a simple white LED combines a blue InGaN LED and a Ce-doped yttrium aluminum garnet (YAG:Ce) phosphor with broad emission centered at yellow emission wavelengths. A phosphor with red emission may be added to improve the color quality of the light. Section 1.2.2 further discusses measuring and characterizing white light color quality.

Another way to produce white light is to use an LED with shorter wavelength emission to excite quantum dots (QDs) with longer wavelength emission. Changing the QD particle size can precisely control QD emission wavelength. This technology is applied commercially today in backlighting liquid crystal displays (LCDs). Overall, this concept is very similar to phosphor-converted LEDs. However, phosphors employed in white lighting produce broad emission peaks, while QDs have very narrow emission peaks. These different spectra lend themselves to different applications. Phosphors are typically favorable for general illumination, while QDs lend themselves to display technology. Again, Section 1.2.2 discusses measuring and characterizing white light and color quality.

One of the disadvantages of optically pumping phosphors or QDs is that the energy efficiency is decreased due to Stokes shift. Stokes shift is the difference between the energy

of the light absorbed and the energy of the light emitted. The phosphor or QD absorbs higher energy blue or violet light and emits lower energy green, yellow, orange, or red light. As an example, using 450 nm (2.76 eV) light to excite a phosphor with 560 nm (2.21 eV) emission produces a Stokes loss of 20 %.

Incorporating phosphors for white light emission also poses challenges from a manufacturing standpoint. A variety of variables are introduced in designing devices that combine LEDs and phosphors, including: type of phosphor, type of silicone, phosphor−silicone interactions, location of phosphor, and integration of optics. A variety of metrics need to be considered when designing such devices, including: temperature stability, environmental stability, photostability, cost, and manufacturing yield. While LEDs are fabricated on a wafer-level, after they are diced into individual chips, packaging steps must be performed on a chip-level. Steps to encapsulate LEDs and incorporate phosphors are typically performed at the chip-level, but performing steps on each individual chip is more time intensive and expensive than wafer-level processing.

An alternative to QD or phosphor-converted LEDs is to produce white light by combining emission from different LEDs. This option is available commercially in, for example, organic LED (OLED) displays, which combine red, green, and blue OLEDs. Comparable inorganic LED displays and white light sources are not yet available. This is largely due to high cost. However, inorganic LEDs offer improved efficiencies and device lifetimes compared to OLEDs. Creating white light by combining emission from LEDs is advantageous because it allows for easy color tunability and eliminates the disadvantages associated with phosphors, including Stokes losses, chip-level manufacturing steps, and silicone and phosphor material limitations.

In addition to decreasing costs, improving the efficiency of InGaN LEDs with emission at long wavelength will also contribute to making phosphor-free white light sources a viable commercial product. While blue InGaN LEDs with 76 % external quantum efficiency (EQE) have been demonstrated, the best green InGaN LEDs are only 32 % efficient. [39] Red, orange, and yellow LEDs continue to be made from AlGaInP alloys. The efficiency of AlGaInP LEDs is limited by extraction efficiency, which is difficult to increase because of the high refractive index of AlGaInP materials. AlGaInP LEDs also suffer from poor performance at increased temperature and carrier overflow, which are a result of relatively small conduction band offsets. Lastly, AlGaInP is relevant for a limited wavelength range because the alloys transition from direct bandgap to indirect bandgap semiconductors. If efficient yellow, orange, and red InGaN LEDs can be realized, they may replace AlGaInP LEDs in white lighting, especially because such advances would enable monolithic white light devices that combine multiple InGaN emitting layers. Different InGaN emitting layers should have more similar performance with increasing temperature and current density as compared to combining InGaN and AlGaInP LEDs.

1.2.2 Measuring and Characterizing White Light

The two main goals in creating white light are efficiency and color quality. There are several efficiency metrics, including: EQE and wall-plug efficiency. Luminous efficacy of a source also captures aspects of efficiency. There are several techniques used to quantify emission color, including: *Commission Internationale de l'Eclairage* (CIE) chromaticity coordinates, correlated color temperature (CCT), color rendering index (CRI), and area of the color gamut. In creating white light, the goal is maximize efficiency and color quality.

However, maximum color quality is usually correlated with decreasing efficiency and efficacy. In addition, optimizing white light must consider the application of the white light source. For example, the ideal white light spectrum for general illumination is different from that for displays. Even in general illumination, the preferred white light spectrum may be dependent on the setting or vary geographically.

EQE is a straightforward metric for quantifying the energy efficiency of an LED; it is simply the number of photons produced per number of electrons provided by electrical current. The wall-plug efficiency or power efficiency measures the efficiency of converting electrical power to optical power; it is the radiant flux per input electrical power. The wall-plug efficiency captures the effects of parasitic resistances. The luminous efficacy of a source has units of lumens/watt and so weighs the emission spectrum using the eye response in order to compare light output to input electrical power. The luminous efficacy is affected by the emission wavelength and the eye response to that wavelength of light. For example, green 555 nm light corresponds to a maximum in the eye response function, and therefore, green 555 nm light has a maximum possible luminous efficacy. Moving away from green towards blue or red wavelengths reduces the value of the eye response function and, thus, the maximum attainable luminous efficacy. Although high luminous efficacy of a source is desirable, white light combines emission at different wavelengths, and white light with high color quality often includes wavelengths with inherently low luminous efficacy due to low human eye sensitivity. White light must find a balance between the need for high luminous efficacy and color quality.

Results presented in Chapter 4 will use the CIE *x*, *y* chromaticity diagram to represent color of emission spectra. The CIE *x*, *y*, and *z* chromaticity coordinates are

calculated from the *X*, *Y*, and *Z* tristimulus values, which indicate the stimulation of the red, green, and blue cones in the human eye, respectively.

$$X = \int_{\lambda} \bar{x}(\lambda)\, P(\lambda)\, d\lambda \tag{1.3.a}$$

$$Y = \int_{\lambda} \bar{y}(\lambda)\, P(\lambda)\, d\lambda \tag{1.3.b}$$

$$Z = \int_{\lambda} \bar{z}(\lambda)\, P(\lambda)\, d\lambda \tag{1.3.c}$$

$$x = \frac{X}{X + Y + Z} \tag{1.4.a}$$

$$y = \frac{Y}{X + Y + Z} \tag{1.4.b}$$

$$z = \frac{Z}{X + Y + Z} \tag{1.4.c}$$

where $P(\lambda)$ is the power spectral density (i.e. power emitted as a function of wavelength) and $\bar{x}(\lambda)$, $\bar{y}(\lambda)$, and $\bar{z}(\lambda)$ are the red, green, and blue color matching functions, which correspond to the eye sensitivities of the red, green, and blue cones, respectively. Figure 1.1 is a CIE *x*, *y* chromaticity diagram, which is used to represent color of emission spectra by plotting an emission spectrum as a point using the *x* and *y* chromaticity coordinates. Monochromatic colors are found along the perimeter of the chromaticity diagram. White light is found in the center of the chromaticity diagram.

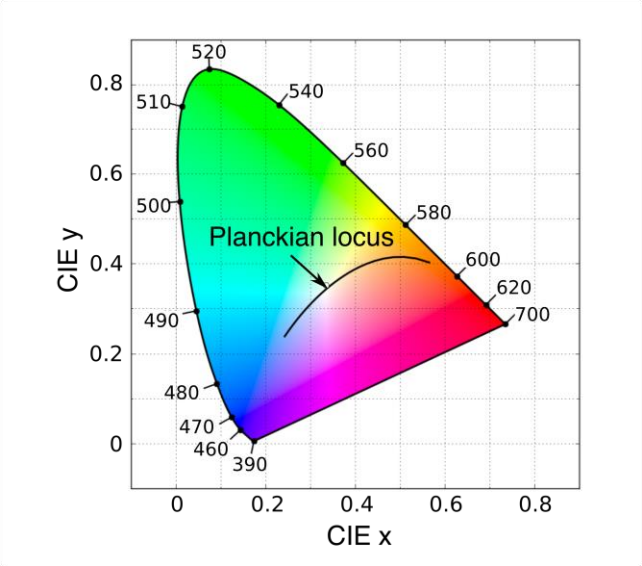

Figure 1.1. CIE *x, y* chromaticity diagram with Planckian locus.

The black line on the chromaticity diagram in Fig. 1.1 is the Planckian locus, which represents the colors of emission from black body emitters at different temperatures. In producing white light for general illumination, it is desirable to produce an emission spectrum similar to emission from a black body emitter. For example, the sun produces an emission spectrum that closely matches a black body emitter with a temperature of 5780 K. Colors that lie close to the Planckian locus on the chromaticity diagram also may be quantified using CCT, which is the temperature of the black body emitter with emission color that most closely matches the emission color of the point near the Planckian locus. Hotter color temperatures are more blue-white, which is called cool white, and colder color temperatures are more yellow-white, which is called warm white.

The CIE *x, y* chromaticity diagram is also useful for understanding and visualizing color mixing. Figure 1.2 shows a CIE *x, y* chromaticity diagram with points (x_1, y_1) and (x_2, y_2) representing blue light and yellow light, respectively. Combining different ratios of this blue light and yellow light produces colors located along the straight line connecting the chromaticity coordinates of the two sources. As expected, combining blue and yellow light

can create white light. In Fig. 1.2, white light indicated by point (x*, y*) lies half way between (x_1, y_1) and (x_2, y_2). Thus, in order to create white light at point (x*, y*), the total power of the yellow source must equal the total power of the blue source.

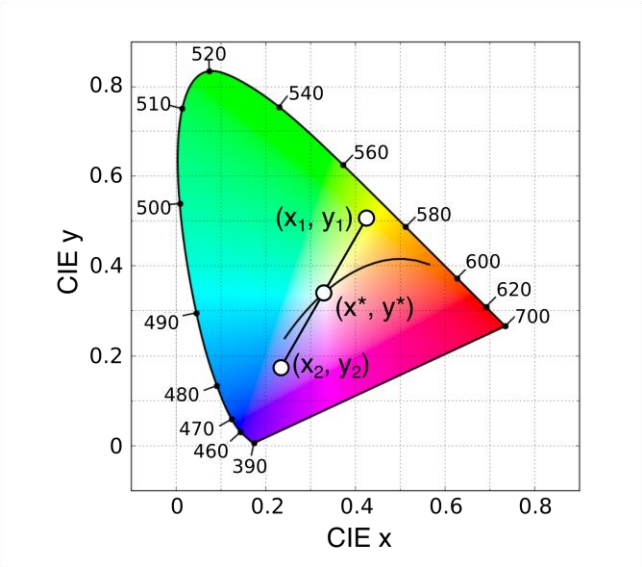

Figure 1.2. CIE *x, y* chromaticity diagram considering color mixing of blue and yellow sources.

Figure 1.3 shows CIE *x*, *y* chromaticity diagram with points indicating red, green, and blue sources. Combining different ratios of red, green, and blue light from these sources can produce any color within the triangular region created by connecting the chromaticity coordinates of the sources. This area is called the color gamut. As expected, combining red, green, and blue light can create white light. In fact, using these red, green, and blue sources, it is possible to create the same color white light as could be created by combining the blue and yellow sources shown in Fig. 1.2.

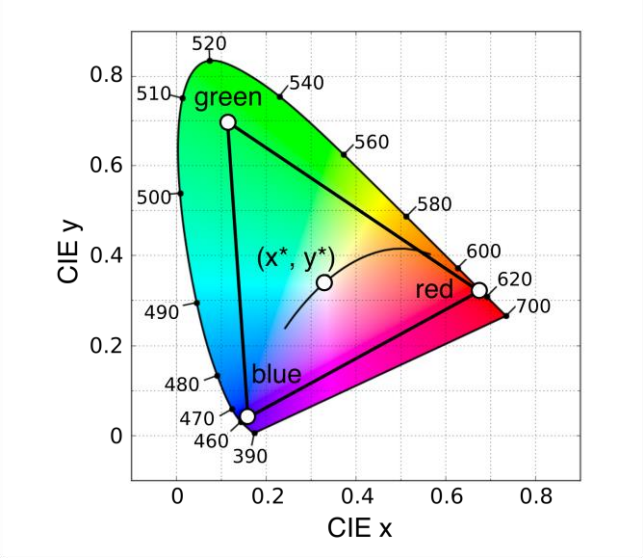

Figure 1.3. CIE *x, y* chromaticity diagram considering color mixing of red, green, and blue sources.

Either the red, green, and blue or the blue and yellow sources shown in Figs. 1.3 and 1.2, respectively, can be used to create the same color white light, represented as (x*, y*). Although the same color, the color quality of this light differs, which can be quantified using CRI. CRI attempts to quantify how well a light source reveals the colors of objects in comparison with the color objects appear when illuminated with an ideal or natural light source, which is defined to have CRI = 100. This is the concept of color fidelity, which is quantified by considering a collection of test samples of different colors and calculating the difference between the sample's natural color (as rendered by the ideal illuminant) and the color appears when illuminated with a test source. As specified by the CIE in 1995, our CRI calculations are based on fourteen test color samples, for which the CIE has defined reflectivity curves. The CRI is calculated by averaging the color rendering indices for the fourteen test color samples. If there is no difference between when the sample object is illuminated with the natural source or test source, then the test color sample rendering index is 100. A color shift between the sample object illuminated with the test source compared to

the natural source reduces the test color sample color rendering index. It is possible for large color shifts to produce negative values for the test color sample color rendering index.

There are many critiques of how CRI is determined. For example, there is debate about what and how many test color samples should be employed in calculating CRI. There are also different opinions about which color space should be used in quantifying color shifts and how the individual test color sample rendering indices should be combined to determine overall CRI. It is known that high CRI can be achieved by creating a source that faithfully reproduces the test color samples but performs poorly in rendering other colors. In particular, CRI can be inaccurate for emission spectra comprising narrow peaks. Other metrics have been developed, but at this time, CRI remains the current industry standard. Overall, CRI or another similar metric is very important for evaluating the color quality of light applied in general illumination. White light for general illumination should have color fidelity across the visible spectrum, which is best achieved by an emission spectrum that spans the visible wavelengths.

In addition to general illumination, white light is also required for display applications, but the ideal emission spectrum of white light for displays differs from the desired emission spectrum for general illumination. The color gamut is most important for evaluating white light sources used in display technology. Since the color gamut represents the colors that can be made by combining different intensities of sources of different colors, it is desirable for a display to have a large color gamut. The color of the light sources defining the color gamut of a display is determined by the color of the individual pixels. Displays most commonly combine red, green, and blue pixels, which would create a triangular color gamut similar to the one illustrated in Fig. 1.3.

As discussed in Section 1.2.1, individually driven LEDs can be used as pixels in a display. In this case, the colors of the pixels are determined by the emission spectra of the individual LEDs. Alternatively, LED white light sources are employed in backlighting LCDs. In this case, the colors of the pixels of a LCD depend on the transmission of LCD filters as well as the emission spectrum of the white backlight. Section 1.2.1 also discussed that LCDs may be backlit by LEDs pumping phosphors or QDs, which produce broader or narrower emission peaks at long wavelengths, respectively. Considering the color gamuts helps to explain the benefit of QDs in improving displays. Because QDs produce narrower emission peaks, the color of the pixels lie closer to the perimeter of the CIE chromaticity diagram, which increases the area of the color gamut. Aligning the QD emission spectra with the transmission spectra of the filters also decreases light loss to absorption in the filters. For example, wavelengths of light between green and red have low transmission through both the green and red filters. Overall, for a display with red, green, and blue pixels, it is most desirable to have a white light source with sharp red, green, and blue peaks because this maximizes the color gamut. However, such a white light emission would be less desirable for general illumination as it would have low CRI.

1.3 Polarized Light

1.3.1 Spontaneous Emission of Polarized Light

The optical polarization of spontaneous emission is determined by the valence band structure. In III-nitrides, the top three valence bands (VBs) are derived from the nitrogen p_x, p_y, and p_z orbitals, where the *x*-, *y*-, and *z*-directions are defined as the $\langle 11\bar{2}0 \rangle$ *a*-direction,

$\langle 1\bar{1}00\rangle$ *m*-direction, and the $\langle 0001\rangle$ *c*-direction, respectively. Light emitted normal to the surface of a *c*-plane InGaN device is not polarized because the biaxial stress in a coherent *c*-plane QW is isotropic in the *m*- and *a*-directions. This results in the top two VBs always being degenerate and equally mixed with $|X\rangle$ and $|Y\rangle$ states. The third VB is the $|Z\rangle$ state, and it is relatively far away from the top two VBs at the Γ point, leading to a low probability of the $|Z\rangle$ state being populated. This VB structure for coherently strained *c*-plane InGaN LEDs produces emission normal to the surface that is not optically polarized, though the sidewall emission is highly polarized. [40]

For semipolar and nonpolar InGaN LEDs, light emitted normal to the surface is partially polarized due to anisotropic biaxial stress in InGaN QWs that increases the energy separation of the top two VBs and changes the state character of the VBs. [13]–[17] For the case of InGaN growth on inclined *m*-planes, like $(20\bar{2}1)$ and $(20\bar{2}\bar{1})$, the anisotropic biaxial stress results in the top VB being mainly $|X\rangle$ state and the second and third VBs being mixed with $|Y\rangle$ and $|Z\rangle$ states. [13] Because radiative recombination results primarily from recombination of electrons in the conduction band with holes in the top VB, dipole emission from $|X\rangle$ is considered, and the emission from InGaN QWs grown on semipolar inclined *m*-planes is partially polarized with the electric field aligned parallel to the *a*-direction. Light polarized with the electric field aligned parallel to the projection of the *c*-direction onto the growth plane is contributed by recombination between electrons in the conduction band and holes in the second VB.

Polarization switching has been reported with increasing indium content for growth on certain semipolar III-nitrides planes. For example, for growth on $(11\bar{2}2)$, which is rotated by 58.4° from *c*-plane, the polarization of the dominant component of emission

switches when indium content of InGaN QWs reaches approximately 30 %. [41], [42] Polarization switching results because with increasing indium content, the second VB approaches the topmost VB, and when a certain indium content is exceeded, the order of the VBs switches. Schade *et al.* have investigated polarization switching from a theoretical perspective and have concluded that polarization switching will affect semipolar planes with inclination angles with respect to *c*-plane that are smaller 69.4°. [43] Because $(20\bar{2}1)$ and $(20\bar{2}\bar{1})$ are inclined by 75° compared to *c*-plane, they experience small shear strain contribution to the valence band energy shift and are not affected by polarization switching with increasing indium content.

Devices with optically polarized emission must also be designed to prevent scattering of emitted light. Typically LEDs employ roughened surfaces to intentionally scatter light and increase extraction efficiency. LEDs with roughened surfaces will produce unpolarized light. In addition, device designs that include powdered phosphors cannot produce optically polarized emission. Even if an LED with optically polarized emission was used in a phosphor-converted LED, the LED emission would be scattered by the powdered phosphor. Additionally, powdered phosphors do not emit optically polarized light.

1.3.2 Measuring and Characterizing Polarized Light

Polarized light is measured by inserting a polarizer between the sample and the detector. This polarizer can be rotated to allow only light with the desired polarization to be transmitted to the detector. The details of the measurement set-up used in this work are detailed in Section 4.1. The degree to which emission is optically polarized is quantified by the polarization ratio, which is defined below.

The $\{20\bar{2}1\}$ III-nitride growth planes are inclined by 15° from the nonpolar *m*-plane. For growth on $(20\bar{2}1)$, we define the x'-, y'-, and z'-directions. The z'-direction is normal to the $(20\bar{2}1)$ growth plane. The x'-direction is $[1\bar{2}10]$, which is the same as the previously defined *x*-direction, and the y'-direction is $[10\bar{1}\bar{4}]$, which is the projection of the –*c*-direction onto the $(20\bar{2}1)$ plane. Thus, for growth on $(20\bar{2}1)$, the polarized light emission intensity is at a maximum when the polarizer is aligned along the x'-direction, and the polarized light emission intensity is at a minimum when the polarizer is aligned along the y'-direction. The optical polarization ratio (ρ) is calculated according to

$$\rho = \left(I_{x'} - I_{y'}\right)/\left(I_{x'} + I_{y'}\right), \tag{1.5}$$

where $I_{x'}$ and $I_{y'}$ are the integrated electroluminescence (EL) intensities with the polarizer aligned along the $[1\bar{2}10]$ and $[10\bar{1}\bar{4}]$ directions of the sample, respectively.

Unpolarized light has a polarization ratio of zero. Perfectly polarized light has a polarization ratio of one. We can consider comparable light that only differs in its polarization ratio, and we can consider light that is either unpolarized with a polarization ratio of 0 or light that is partially polarized with a polarization ratio of, for example, 0.4. If we assume a polarizer with 100% transmission of light with the desired polarization, 50% of the intensity of the unpolarized light will pass through the polarizer, and 70% of the light with a polarization ratio of 0.4 will pass through the polarizer. Thus, 40% more light would pass through the polarizer for the case where the incident light had a polarization ratio of 0.4 compared to the case where the incident light was unpolarized, and this would be a 40% increase in the efficiency of the transmission of the partially polarized light.

References

[1] P. Waltereit, O. Brandt, A. Trampert, H. T. Grahn, J. Menniger, M. Ramsteiner, M. Reiche, and K. H. Ploog, "Nitride semiconductors free of electrostatic fields for efficient white light-emitting diodes," *Nature*, vol. 406, no. 6798, pp. 865–868, Aug. 2000.

[2] A. E. Romanov, T. J. Baker, S. Nakamura, and J. S. Speck, "Strain-induced polarization in wurtzite III-nitride semipolar layers," *J. Appl. Phys.*, vol. 100, no. 2, p. 023522, 2006.

[3] D. F. Feezell, J. S. Speck, S. P. DenBaars, and S. Nakamura, "Semipolar (20-2-1) InGaN/GaN Light-Emitting Diodes for High-Efficiency Solid-State Lighting," *J. Disp. Technol.*, vol. 9, no. 4, pp. 190–198, Apr. 2013.

[4] E. Kioupakis, P. Rinke, K. T. Delaney, and C. G. Van de Walle, "Indirect Auger recombination as a cause of efficiency droop in nitride light-emitting diodes," *Appl. Phys. Lett.*, vol. 98, no. 16, p. 161107, 2011.

[5] E. Kioupakis, Q. Yan, and C. G. Van de Walle, "Interplay of polarization fields and Auger recombination in the efficiency droop of nitride light-emitting diodes," *Appl. Phys. Lett.*, vol. 101, no. 23, p. 231107, 2012.

[6] A. David and M. J. Grundmann, "Droop in InGaN light-emitting diodes: A differential carrier lifetime analysis," *Appl. Phys. Lett.*, vol. 96, no. 10, p. 103504, 2010.

[7] J. Iveland, M. Piccardo, L. Martinelli, J. Peretti, J. W. Choi, N. Young, S. Nakamura, J. S. Speck, and C. Weisbuch, "Origin of electrons emitted into vacuum from InGaN light emitting diodes," *Appl. Phys. Lett.*, vol. 105, no. 5, p. 052103, Aug. 2014.

[8] W. Gotz, N. M. Johnson, J. Walker, D. P. Bour, and R. A. Street, "Activation of acceptors in Mg-doped GaN grown by metalorganic chemical vapor deposition," *Appl. Phys. Lett.*, vol. 68, no. 5, p. 667, 1996.

[9] D. L. Becerra, Y. Zhao, S. H. Oh, C. D. Pynn, K. Fujito, S. P. DenBaars, and S. Nakamura, "High-power low-droop violet semipolar (30-3-1) InGaN/GaN light-emitting diodes with thick active layer design," *Appl. Phys. Lett.*, vol. 105, no. 17, p. 171106, Oct. 2014.

[10] C.-C. Pan, S. Tanaka, F. Wu, Y. Zhao, J. S. Speck, S. Nakamura, S. P. DenBaars, and D. Feezell, "High-Power, Low-Efficiency-Droop Semipolar (20-2-1) Single-Quantum-Well Blue Light-Emitting Diodes," *Appl. Phys. Express*, vol. 5, no. 6, p. 062103, Jun. 2012.

[11] A. Pourhashemi, R. M. Farrell, D. a. Cohen, J. S. Speck, S. P. DenBaars, and S. Nakamura, "High-power blue laser diodes with indium tin oxide cladding on

semipolar (20-2-1) GaN substrates," *Appl. Phys. Lett.*, vol. 106, no. 11, p. 111105, Mar. 2015.

[12] K. M. Kelchner, R. M. Farrell, Y.-D. Lin, P. S. Hsu, M. T. Hardy, F. Wu, D. a. Cohen, H. Ohta, J. S. Speck, S. Nakamura, and S. P. DenBaars, "Continuous-Wave Operation of Pure Blue AlGaN-Cladding-Free Nonpolar InGaN/GaN Laser Diodes," *Appl. Phys. Express*, vol. 3, no. 9, p. 092103, Sep. 2010.

[13] Y. Zhao, R. M. Farrell, Y. Wu, and J. S. Speck, "Valence band states and polarized optical emission from nonpolar and semipolar III–nitride quantum well optoelectronic devices," *Jpn. J. Appl. Phys.*, vol. 53, no. 10, p. 100206, Oct. 2014.

[14] R. B. Chung, Y.-D. Lin, I. Koslow, N. Pfaff, H. Ohta, J. Ha, S. P. DenBaars, and S. Nakamura, "Electroluminescence Characterization of (20-21) InGaN/GaN Light Emitting Diodes with Various Wavelengths," *Jpn. J. Appl. Phys.*, vol. 49, no. 7, p. 070203, Jul. 2010.

[15] Y. Zhao, S. Tanaka, Q. Yan, C.-Y. Huang, R. B. Chung, C.-C. Pan, K. Fujito, D. Feezell, C. G. Van de Walle, J. S. Speck, S. P. DenBaars, and S. Nakamura, "High optical polarization ratio from semipolar (20-2-1) blue-green InGaN/GaN light-emitting diodes," *Appl. Phys. Lett.*, vol. 99, no. 5, p. 051109, 2011.

[16] S. Marcinkevičius, R. Ivanov, Y. Zhao, S. Nakamura, S. P. DenBaars, and J. S. Speck, "Highly polarized photoluminescence and its dynamics in semipolar (20-2-1) InGaN/GaN quantum well," *Appl. Phys. Lett.*, vol. 104, no. 11, p. 111113, Mar. 2014.

[17] T. Kyono, Y. Yoshizumi, Y. Enya, M. Adachi, S. Tokuyama, M. Ueno, K. Katayama, and T. Nakamura, "Optical Polarization Characteristics of InGaN Quantum Wells for Green Laser Diodes on Semi-Polar (20-21) GaN Substrates," *Appl. Phys. Express*, vol. 3, no. 1, p. 011003, Jan. 2010.

[18] S.-H. Park and D. Ahn, "High optical polarization ratio of semipolar (20-2-1)-oriented InGaN/GaN quantum wells and comparison with experiment," *J. Appl. Phys.*, vol. 112, no. 9, p. 093106, 2012.

[19] Y. Zhao, Q. Yan, D. Feezell, K. Fujito, C. G. Van de Walle, J. S. Speck, S. P. DenBaars, and S. Nakamura, "Optical polarization characteristics of semipolar (30-31) and (30-3-1) InGaN/GaN light-emitting diodes," *Opt. Express*, vol. 21, no. S1, p. A53, Jan. 2013.

[20] X. H. Wu, C. R. Elsass, A. Abare, M. Mack, S. Keller, P. M. Petroff, S. P. DenBaars, J. S. Speck, and S. J. Rosner, "Structural origin of V-defects and correlation with localized excitonic centers in InGaN/GaN multiple quantum wells," *Appl. Phys. Lett.*, vol. 72, no. 6, p. 692, 1998.

[21] A. E. Romanov, E. C. Young, F. Wu, A. Tyagi, C. S. Gallinat, S. Nakamura, S. P. DenBaars, and J. S. Speck, "Basal plane misfit dislocations and stress relaxation in III-nitride semipolar heteroepitaxy," *J. Appl. Phys.*, vol. 109, no. 10, p. 103522, 2011.

[22] J. W. Matthews and A. E. Blakeslee, “Defects in epitaxial multilayers,” *J. Cryst. Growth*, vol. 27, pp. 118–125, Dec. 1974.

[23] P. Shan Hsu, M. T. Hardy, E. C. Young, A. E. Romanov, S. P. DenBaars, S. Nakamura, and J. S. Speck, “Stress relaxation and critical thickness for misfit dislocation formation in (10-10) and (30-3-1) InGaN/GaN heteroepitaxy,” *Appl. Phys. Lett.*, vol. 100, no. 17, p. 171917, 2012.

[24] P. S. Hsu, E. C. Young, A. E. Romanov, K. Fujito, S. P. DenBaars, S. Nakamura, and J. S. Speck, “Misfit dislocation formation via pre-existing threading dislocation glide in (11-22) semipolar heteroepitaxy,” *Appl. Phys. Lett.*, vol. 99, no. 8, p. 081912, 2011.

[25] F. Wu, E. C. Young, I. Koslow, M. T. Hardy, P. S. Hsu, a. E. Romanov, S. Nakamura, S. P. DenBaars, and J. S. Speck, “Observation of non-basal slip in semipolar InxGa1-xN/GaN heterostructures,” *Appl. Phys. Lett.*, vol. 99, no. 25, p. 251909, 2011.

[26] M. T. Hardy, P. S. Hsu, F. Wu, I. L. Koslow, E. C. Young, S. Nakamura, A. E. Romanov, S. P. DenBaars, and J. S. Speck, “Trace analysis of non-basal plane misfit stress relaxation in (20-21) and (30-3-1) semipolar InGaN/GaN heterostructures,” *Appl. Phys. Lett.*, vol. 100, no. 20, p. 202103, 2012.

[27] M. T. Hardy, F. Wu, P. Shan Hsu, D. a. Haeger, S. Nakamura, J. S. Speck, and S. P. DenBaars, “True green semipolar InGaN-based laser diodes beyond critical thickness limits using limited area epitaxy,” *J. Appl. Phys.*, vol. 114, no. 18, p. 183101, 2013.

[28] M. T. Hardy, S. Nakamura, J. S. Speck, and S. P. DenBaars, “Suppression of relaxation in (20-21) InGaN/GaN laser diodes using limited area epitaxy,” *Appl. Phys. Lett.*, vol. 101, no. 24, p. 241112, 2012.

[29] E. A. Fitzgerald, G. P. Watson, R. E. Proano, D. G. Ast, P. D. Kirchner, G. D. Pettit, and J. M. Woodall, “Nucleation mechanisms and the elimination of misfit dislocations at mismatched interfaces by reduction in growth area,” *J. Appl. Phys.*, vol. 65, no. 6, p. 2220, 1989.

[30] P. S. Hsu, M. T. Hardy, F. Wu, I. Koslow, E. C. Young, A. E. Romanov, K. Fujito, D. F. Feezell, S. P. DenBaars, J. S. Speck, and S. Nakamura, “444.9 nm semipolar (11-22) laser diode grown on an intentionally stress relaxed InGaN waveguiding layer,” *Appl. Phys. Lett.*, vol. 100, no. 2, p. 021104, 2012.

[31] I. L. Koslow, M. T. Hardy, P. Shan Hsu, P.-Y. Dang, F. Wu, A. Romanov, Y.-R. Wu, E. C. Young, S. Nakamura, J. S. Speck, and S. P. DenBaars, “Performance and polarization effects in (11-22) long wavelength light emitting diodes grown on stress relaxed InGaN buffer layers,” *Appl. Phys. Lett.*, vol. 101, no. 12, p. 121106, 2012.

[32] R. a. Oliver, M. J. Kappers, C. J. Humphreys, and G. A. D. Briggs, “Growth modes in heteroepitaxy of InGaN on GaN,” *J. Appl. Phys.*, vol. 97, no. 1, p. 013707, 2005.

[33] S. Kim, K. Lee, K. Park, and C.-S. Kim, “Effects of barrier growth temperature on the properties of InGaN/GaN multi-quantum wells,” *J. Cryst. Growth*, vol. 247, no. 1–2, pp. 62–68, Jan. 2003.

[34] G. Parish, S. Keller, S. P. Denbaars, and U. K. Mishra, “SIMS investigations into the effect of growth conditions on residual impurity and silicon incorporation in GaN and AlxGa(1−x)N,” *J. Electron. Mater.*, vol. 29, no. 1, pp. 15–20, Jan. 2000.

[35] B. Van Daele, G. Van Tendeloo, K. Jacobs, I. Moerman, and M. R. Leys, “Formation of metallic in in InGaN/GaN multiquantum wells,” *Appl. Phys. Lett.*, vol. 85, no. 19, pp. 4379–4381, 2004.

[36] M. T. Hardy, F. Wu, C.-Y. Huang, Y. Zhao, D. F. Feezell, S. Nakamura, J. S. Speck, and S. P. DenBaars, “Impact of p-GaN Thermal Damage and Barrier Composition on Semipolar Green Laser Diodes,” *IEEE Photonics Technol. Lett.*, vol. 26, no. 1, pp. 43–46, Jan. 2014.

[37] W. Lee, J. Limb, J.-H. Ryou, D. Yoo, T. Chung, and R. D. Dupuis, “Influence of growth temperature and growth rate of p-GaN layers on the characteristics of green light emitting diodes,” *J. Electron. Mater.*, vol. 35, no. 4, pp. 587–591, Apr. 2006.

[38] F. Wu, Y. Zhao, A. Romanov, S. P. DenBaars, S. Nakamura, and J. S. Speck, “Stacking faults and interface roughening in semipolar (20-2-1) single InGaN quantum wells for long wavelength emission,” *Appl. Phys. Lett.*, vol. 104, no. 15, p. 151901, Apr. 2014.

[39] N. Bardsley, S. Bland, M. Hansen, L. Pattison, M. Pattison, K. Stober, and M. Yamada, “Solid-State Lighting R & D Plan,” 2015.

[40] M. F. Schubert, S. Chhajed, J. K. Kim, E. Fred Schubert, and J. Cho, “Polarization of light emission by 460 nm GaInN/GaN light-emitting diodes grown on (0001) oriented sapphire substrates,” *Appl. Phys. Lett.*, vol. 91, no. 5, p. 051117, 2007.

[41] M. Ueda, M. Funato, K. Kojima, Y. Kawakami, Y. Narukawa, and T. Mukai, “Polarization switching phenomena in semipolar InxGa(1-x)N/GaN quanum well active layers,” *Phys. Rev. B*, vol. 78, no. 23, p. 233303, Dec. 2008.

[42] L. Schade and U. T. Schwarz, “Energy offset between valence band anti-crossing and optical polarization switching in semipolar InGaN quantum wells,” *Appl. Phys. Lett.*, vol. 102, no. 23, p. 232101, 2013.

[43] L. Schade, U. T. Schwarz, T. Wernicke, J. Rass, S. Ploch, M. Weyers, and M. Kneissl, “On the optical polarization properties of semipolar InGaN quantum wells,” *Appl. Phys. Lett.*, vol. 99, no. 5, p. 051103, 2011.

Chapter 2

Novel Device Design for Polarized White Light Emission

2.1 Introduction and Motivation

Polarized white light has applications where polarized white light is required or advantageous. If an unpolarized light source is used in applications requiring polarized light, the light must be passed through a polarizer, which results in the loss of light that is not aligned with the polarizer. In the case of unpolarized light, only 50% of the light will be aligned with the polarizer. Most technology employing polarized light improves transmission through a polarizer by incorporating a reflective layer to repeatedly reflect light with the undesired polarization with the intention of scattering the light to change its polarization. Additional loss is introduced because most polarizers have some absorption of light with the desired optical polarization, though this absorption is minimal for the best polarizers. Overall, because light is lost when unpolarized light is passed through a polarizer, the opportunity exists to improve the energy efficiency of devices that utilize polarized light by using a device that emits polarized light. While perfectly polarized light would eliminate the need for a polarizer, partially polarized light would also be more efficient than unpolarized light because a greater percentage of light would pass through the polarizer (as discussed in Section 1.3.).

The largest current application of polarized white light is in liquid crystal displays (LCDs). LCDs today are typically backlit by phosphor-converted light-emitting diodes (LEDs), which produce unpolarized light that must be passed through a rear polarizer. The LCD requires polarized white light because the optical polarization determines whether light passed through each individual pixel is transmitted through a front polarizer to reach a viewer's eye. Each pixel in the LCD has a transistor, which applies an electric field across the liquid crystal when turned on. When the transistor is off, the liquid crystal acts to rotate the optical polarization of the light passing through it by 90°. When the transistor is on, the liquid crystal will align with the electric field, which allows light passing through it to maintain its optical polarization. The front polarizer, which is rotated by 90° compared to the rear polarizer, only transmits light that has had its optical polarization rotated. Thus, the optical polarization is used to control which pixels are illuminated in a LCD. Although LCDs are currently the largest application of polarized white light, incorporating polarized white light sources in LCDs will need to consider how to achieve uniform lighting. LED backlights today require diffusers to produce even lighting to backlight LCDs. In addition to LCDs, there are other applications of polarized light, for example, 3D display and holography applications. Polarized white light could also have potential applications in general illumination applications, where polarized light could be leverage to reduce glare.

This chapter will present novel device designs, which we have proposed for polarized white light emission. Our demonstrations of these device designs are subsequently presented in Chapter 4. Prior to demonstrating these devices, polarized white light emission from a single device had not been previously reported.

2.2 Novel Device Designs

2.2.1 Double-sided Devices

We have proposed a device design to enable polarized white light emission from a single III-nitride device. This device monolithically incorporates electrically injected and optically pumped InGaN quantum wells (QWs), where the emission from the electrically injected QWs is higher in energy and used to excite the optically pumped QWs. Utilizing optically pumped QWs rather than electrically injected QWs has several advantages for achieving long wavelength emission from InGaN QWs.

First, optical pumping allows for QWs to be exposed to a limited thermal budget, which is favorable because high temperatures have been shown to degrade high indium content InGaN. [1], [2] The thermal budget is limited by growing optically pumped, high indium content InGaN QWs after the higher temperature growth steps for the shorter wavelength, electrically injected QWs. Additionally, optical pumping eliminates the need for *p*-type GaN above the QWs, which is required for electrical injection and typically is performed at higher growth temperatures to achieve adequate *p*-type conduction. [1], [3]

A second advantage of optically pumping QWs for long wavelength emission is that wide or strain compensating barriers can be incorporated between InGaN QWs to help prevent relaxation. [4], [5] Wide or strain compensating barriers are challenging in electrically injected devices because QWs must be confined within a depletion width and carriers must be transported across all QWs. [6] Optically pumping QWs for long wavelength emission eliminates these constraints.

Another benefit of optically pumped devices, where carrier transport and confining QWs within the depletion width are not a concern, is the ability to create multiple QW

(MQW) devices. [7] As discussed in Section 1.1.3, the efficiency of III-nitride emitters is expected to decrease for longer emission wavelengths. InGaN QWs with long wavelength emission have increased nonradiative recombination and decreased radiative recombination because of lower crystal quality and decreased overlap of electron and hole wavefunctions. A device with optically pumped QWs can increase the amount of long wavelength emission in a straightforward way by increasing the number of optically pumped QWs. The ideal electrically injected and optically pumped device will have the correct number of optically pumped QWs with long wavelength emission to result in uniform white light emission. Determining the number of optically pumped QWs required will be a function of the absorbance and radiative efficiency of the optically pumped QWs as well as the colors of the electrically injected and optically pumped QWs.

Optically pumped devices are also advantageous because they typically have lower carrier densities than electrically injected devices, which is desirable because nonradiative Auger recombination dominates at high carrier densities since it scales with the third power of the carrier density, as discussed in Section 1.1.1. [7]–[10] The carrier concentration in optically pumped QWs is limited by generation of carriers, which depends on the excitation photon flux and QW absorption. The photon flux is limited by the illumination source. The QW absorption is limited because InGaN QWs are relatively thin in order to achieve electron and hole wavefunction overlap and prevent relaxation of pseudomorphic InGaN layers on GaN. Overall, optically pumped QWs typically have lower carrier densities compared to electrically injected devices, but as discussed above, optical pumping enables MQW stacks, and optically pumped MQW stacks can produce luminous flux comparable to

the best LEDs. [7] Ultimately, optically pumped devices with high luminous flux spread carriers across MQWs for lower carrier densities, which decrease Auger recombination.

Results from Osram published by Galler *et al.* demonstrated an optically pumped MQW structure with green emission that had luminous flux comparable to the best reported values for green LEDs. [7] This paper also reported an optically pumped MQW structure with green emission to have an efficiency maximum shifted by an order of magnitude towards higher equivalent current density as compared to the best reported green LEDs. The ability to reduce Auger recombination in optically pumped MQWs is especially of interest for achieving long wavelength emission because, as discussed in Section 1.1, QWs with long wavelength emission have higher carrier densities and increased Auger recombination. QWs with long wavelength emission are affected by decreased wavefunction overlap due to wide QWs or increased piezoelectric polarization-induced electric fields in QWs with higher indium content InGaN. [8]

By using a double side polished (DSP) bulk GaN substrate, the electrically injected device can be grown on one side, and the optically pumped layers can be grown on the opposite side. This enables the higher temperature growth of the electrically injected LED with shorter wavelength emission to be performed prior to the growth of the optically pumped, higher indium content InGaN QWs for long wavelength emission. Figure 2.1 shows a cross-sectional schematic of an example of a double-sided device with monolithic electrically injected and optically pumped QWs. The fabricated device is flipped so that the *p*-type GaN of the LED faces down and light is extracted from the top face on which the optically pumped QWs were grown. The *p*-type contact is a metal mirror, which serves to

reflect light towards the optically pumped QWs for possible absorption and towards the top surface for extraction.

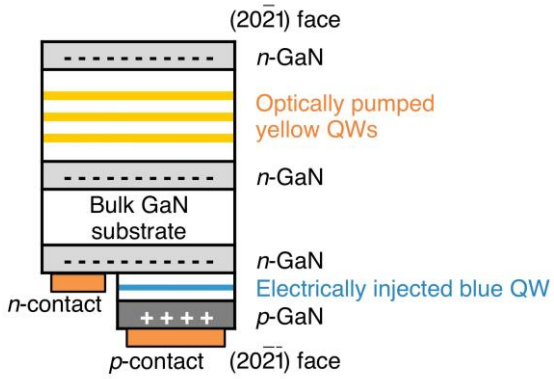

Figure 2.1. Cross-sectional schematic of a double-sided, electrically injected and optically pumped semipolar device for polarized white light emission.

In order to achieve white light emission, a blue LED could be used to pump higher indium content InGaN QWs with yellow emission, as shown in Fig. 2.1. This would produce white light with a spectrum similar to white light produced by a blue LED pumping a Ce-doped yttrium aluminum garnet (YAG:Ce) phosphor. However, one of the benefits of this design is that the emission spectrum produced by the optically pumped QWs can be tailored to produce white light in different ways. White light could also be produced by using a blue LED to optically pump green and red QWs, or multiple optically pumped QWs with slightly varying emission wavelengths could be used to create a broad peak spanning green to red. In order to achieve polarized emission, the surfaces of the final device are not roughened in order to prevent scattering of the light. Lastly, as will be discussed in Section 5.2.2, dichroic mirrors on the device sidewalls and/or top surface may help control the emission color and improve the polarization ratio.

In particular, our work has focused on electrically injected and optically pumped devices grown on $(20\bar{2}1)/(20\bar{2}\bar{1})$ DSP bulk GaN substrates. $(20\bar{2}\bar{1})$ is a favorable plane for growth of blue LEDs, as previous work has demonstrated $(20\bar{2}\bar{1})$ blue LEDs with high

power, low droop, and small wavelength shift. [11]–[13] $(20\bar{2}1)$ is a favorable plane for growth of long wavelength emitting layers because previous work has demonstrated high indium content InGaN QWs with long wavelength emission on $(20\bar{2}1)$, [14]–[16] while basal plane stacking faults (BPSFs) have been observed when increasing the indium content of InGaN layers on $(20\bar{2}\bar{1})$. [17] Additionally, the semipolar $(20\bar{2}1)$ and $(20\bar{2}\bar{1})$ planes are good candidates for optically polarized emission, as discussed in Section 1.3.

2.2.2 Devices with Band Engineering Emission Wavelength

A further benefit of optically pumping QWs for long wavelength emission is that the doping profile can be engineered to tailor the emission wavelength of optically pumped QWs. For example, when *p*-*n* junction is used to create a built-in electric field that acts in the same direction as the polarization-induced electric field (such as in certain semipolar orientations), [13], [18] the total electric field in the QW increases, decreasing the energy of the ground state transitions and red-shifting the emission wavelength. Because optically pumped QWs are not electrically injected and therefore are unbiased, the electric field in these QWs will remain largely unchanged during device operation.

Band engineering can enable emission at longer wavelengths than can otherwise be achieved by simple manipulation of the alloy composition. Additionally, band engineering can also be used to red-shift the emission wavelength of a QW so that a desired wavelength can be realized using a lower indium content InGaN QW or a thinner QW. The ability to utilize lower indium content InGaN is advantageous because it enables growth at higher temperatures for higher crystal quality material. For InGaN layers grown pseudomorphically on GaN, lower indium content InGaN films and thinner QWs also have less stress than

higher indium content InGaN films or thicker QWs. Reduced stress is favorable to ensuring that strained layers do not relax. [19]

A monolithic optically pumped and electrically injected device that utilizes band engineering to red-shift emission from optically pumped QWs ultimately is similar to the double-sided device described in Section 2.2.1, and Fig. 2.2 shows a cross-sectional schematic of an example of such a device. Again, the blue LED would be grown first, followed by the subsequent growth of optically pumped QWs for long wavelength emission. The double-sided device design enables band engineering to red-shift the emission from the optically pumped QWs. In MOCVD growth, *p*-type GaN must be exposed at the surface in order to activate the acceptors by removing the hydrogen from the Mg–H complex. The double-sided device design allows activation of both the *p*-type GaN of the LED as well as the *p*-type GaN that creates a *p*-*i*-*n* structure to red-shift emission from the optically pumped QWs.

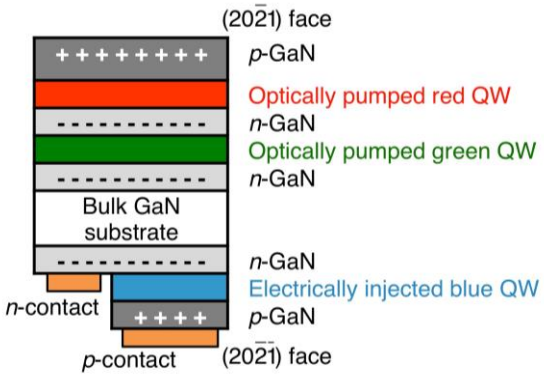

Figure 2.2. Cross-sectional schematic of a double-sided, electrically injected and optically pumped semipolar device utilizing band engineering to red-shift the optically pumped QW situated in a *p*-*n* junction.

Again, as in the case of the double-sided devices discussed in Section 2.2.1, our efforts have focused on the semipolar $(20\bar{2}1)$ and $(20\bar{2}\bar{1})$ growth planes and a device with a blue $(20\bar{2}\bar{1})$ LED and optically pumped $(20\bar{2}1)$QWs for long wavelength emission. In order to create a built-in electric field in the same direction as the polarization-induced

electric field in an InGaN QW grown by MOCVD, the total polarization discontinuity in the growth direction must be antiparallel to that of *c*-plane (i.e., negative). [13], [18] This requirement applies to MOCVD growth where *p*-type GaN must be exposed at the surface for activation of the acceptors. $(20\bar{2}1)$ is an appropriate plane for growing a structure in which the doping profile can be engineered to red-shift emission from optically pumped QWs. Our efforts to reach red emission by increasing the indium content of optically pumped $(20\bar{2}1)$ QWs in an *n-i-n* structure have not yet been successful because higher InGaN indium contents and/or lower growth temperatures negatively impact the InGaN crystal quality and radiative efficiency. However, red emission can be achieved by using a *p-i-n* structure, where the built-in electric field acts in the same direction as the polarization-induced electric field, to red-shift emission.

2.2.3 Tunnel Junction Devices

In a device where QWs with long wavelength emission are optically pumped by monolithic electrically injected QWs, the electrically injected device layers require higher growth temperatures and should be grown prior to the optically pumped layers in order to prevent thermal damage to high indium content InGaN QWs. However, this design requirement is complicated by the fact that device designs with buried *p*-type GaN are challenging. First, MOCVD *p*-type III-nitride layers must be exposed at the surface of the sample in order to be activated by a post-growth anneal that removes hydrogen from the Mg−H complex, which forms during growth and passivates the magnesium acceptors. [20] While molecular beam epitaxy (MBE) enables the growth of activated *p*-type GaN, this growth technique produces InGaN with poor radiative efficiency. [21], [22]

Even if activated buried *p*-type GaN can be achieved, it is challenging to fabricate devices. Transparent conducting oxide (TCO) or reflective metal *p*-contacts typically define the injection area of LEDs because the conductivity of *p*-type GaN is too low to enable current spreading across device areas. Therefore, current spreading is a challenge in devices with buried *p*-type GaN. Additionally, it is challenging to form *p*-contacts to buried *p*-type GaN because dry etching techniques where the sample is exposed to plasma results in damage to *p*-type GaN layers. Exposure to plasma forms nitrogen vacancies, which are *n*-type defects. [23]–[25]

As discussed in Sections 2.2.2 and 2.2.3, double-sided device designs allow for monolithically integrated QWs where a blue LED is grown first and optically pumped QWs for long wavelength emission are grown subsequently on the opposite side of the DSP substrate. Such a double-sided device design avoids the challenges associated with buried *p*-type GaN but requires growth on both sides of a substrate and fabrication of a flip-chip device. Additionally, in a double-sided device, the optically pumped QWs are far away from the electrically injected QWs, which produces devices where significant light escapes from the sidewalls of a device without passing through the optically pumped QWs.

Alternatively, a tunnel junction can be used to monolithically integrate an electrically injected blue LED and optically pumped InGaN QWs with yellow emission grown above the electrically injected QWs. Figure 2.3 shows cross-sectional schematic of an example of such a device. In such a device, a tunnel junction is required to achieve electrical injection of the buried blue LED because a tunnel junction provides a means of carrier conversion between *p*- and *n*-type material. The tunnel junction is formed at the interface of the p^+- and n^+-type layers. The goal is to create a *p*-*n* junction with a small enough distance between the

conduction band on the *n*-side and the valence band on the *p*-side that valence band electrons can tunnel from the *p*-side to the *n*-side resulting in holes in the *p*-type material. This requires highly doped layers and a sharp p^+/n^+ interface.

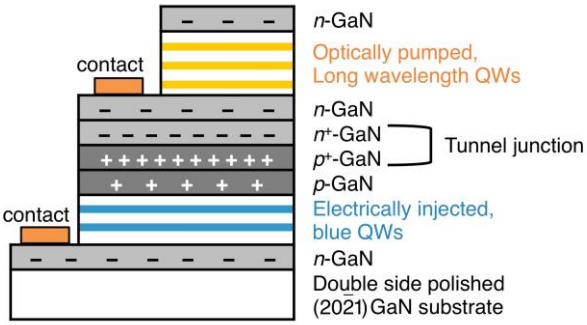

Figure 2.3. Cross-sectional schematic of a semipolar device utilizing a tunnel junction to stack electrically injected and optically pumped QWs for polarized white light emission.

While it would be possible to use any growth plane to create devices in which a tunnel junction is used to monolithically integrate optically pumped and electrically injected QWs, we propose a device grown on $(20\bar{2}1)$ because, as discussed in Section 2.2.1, $(20\bar{2}1)$ is an ideal plane for growing high indium content InGaN QWs [14]–[16] and $(20\bar{2}1)$, which is inclined by 15° from the nonpolar *m*-plane, is an appropriate growth plane for QWs with optically polarized emission, as discussed in Section 1.3. In addition to focusing on growth on $(20\bar{2}1)$, our experimental work has focused on a hybrid MOCVD/MBE growth procedure to enable growth of such optically pumped and electrically injected tunnel junction devices. [26], [27]

To create a tunnel junction device like the one in Fig. 2.3 by a hybrid MOCVD/MBE growth technique, a blue LED is grown first by MOCVD on the $(20\bar{2}1)$ face of a bulk GaN substrate. The *p*-type GaN is activated before a tunnel junction is created by NH_3 MBE growth of an n^+-type GaN layer above the LED p^+-type GaN layer. The n^+-type GaN layer is capped with an *n*-type GaN layer in the MBE prior to MOCVD growth of the optically

pumped QWs. During the growth of the optically pumped QWs, the QWs as well as the barriers and capping layer can be grown at the same temperature to prevent thermal damage to the high indium content InGaN QWs.

In this growth procedure, NH_3 MBE is used in the growth of the tunnel junction, which enables a device with activated buried *p*-type GaN. [26]–[29] Although the optically pumped QWs are subsequently grown by MOCVD, hydrogen has low diffusivity in *n*-type GaN, which prevents hydrogen from diffusing through the MBE *n*-type GaN layers to passivate magnesium acceptors in the *p*-type layers of the LED. [30] Use of MBE also is favorable for growth of the tunnel junction because MBE enables a sharp p^+/n^+ interface, high silicon doping, and GaN with high *n*-type mobility. [31], [32] Magnesium memory effect produces slow turn-off of magnesium doping in MOCVD, and high silicon doping by MOCVD can result in rough sample surfaces. [33]

In fabricating the final device, contact would be made to the *n*-side of the LED and the *n*-side of the tunnel junction, allowing for electrical injection of the blue QWs. There is no *p*-type contact, which is beneficial because no metal with an appropriate work function exists for making ohmic contact to *p*-type GaN. [34], [35] In this device structure, the *n*-type GaN above the tunnel junction is used for current spreading, which is advantageous because GaN has less absorbance than TCOs or metal contacts. [29] Because the *n*-type GaN layer is used for current spreading on the *p*-side of the LED, in a vertical LED design, small area contacts decrease absorption.

2.3 Relevant Device Designs from Literature

Monolithically integrated InGaN layers have been used in prior work to produce white light. However, because these InGaN layers were grown on *c*-plane GaN, the resulting white light was not polarized, as discussed in Section 1.3.1. White light has been demonstrated by electrical injection across vertically stacked InGaN layers [36]–[39] as well as laterally distributed InGaN layers with different emission wavelengths. [40] Other groups have also demonstrated *c*-plane device designs similar to the devices we report here, where blue light produced from electrically injected InGaN layers is used to optically pump longer wavelength emitting InGaN layers. [41], [42] However, in these devices, the optically pumped high indium content InGaN layers for long wavelength emission were grown on the same plane as and prior to the blue LED. This resulted in the high indium content InGaN layers being exposed to higher temperatures during the growth of the blue LED, which could degrade the performance of the high indium content layers. [1], [2]

Prior to our results, comparable monolithic devices had not been previously demonstrated on semipolar or nonpolar growth planes. Similar to phosphor-converted *c*-plane LEDs, blue semipolar and nonpolar LEDs have been combined with long wavelength emitting phosphors to produce white light. Although the light emitted by semipolar and nonpolar LEDs is polarized, the surfaces of a fabricated LED are roughened to increase light extraction, which results in scattering of the light and a loss of optical polarization. Light is also scattered by powdered phosphors, and the long wavelength emission from the powdered phosphors is not optically polarized. Fellows *et al*. report polarized white light by combining emission from a yellow semipolar LED and a blue *m*-plane LED. [43] In this case, the two LEDs were driven independently by two power supplies.

2.4 Comments on the Required Number of Optically Pumped Quantum Wells

An electrically injected and optically pumped device for polarized white light emission will require enough optically pumped QWs to absorb a significant portion of the blue light for conversion to long wavelength emission. As will be discussed in Chapter 3, we have been limited in how many QWs we can achieve in our MQW stacks because defects in the QWs increase in size with increasing number of QWs. However, researchers working on InGaN QW solar cells have achieved growth of samples with many QWs and have studied absorption of such MQW stacks. Although the majority of InGaN solar cell work was performed on *c*-plane and for QWs with emission from blue to green wavelengths, solar cell results provide absorbance data that is useful in considering how many optically pumped QWs will be required in our proposed electrically injected and optically pumped devices.

Work published by Young *et al*. has absorbance data for 10, 20, 30, and 50 InGaN MQW solar cells on *c*-plane. [44] The absorption edge was at 450 nm, and Table 2.1 summarizes the measured absorbance at 420 nm and 410 nm for the samples grown on sapphire and bulk GaN substrates. Work published by Farrell *et al.* also reports absorbance data for 10, 20, and 30 InGaN MQW solar cells grown on sapphire. [45] The absorption edge was at 500 nm, and Table 2.1 summarizes the measured absorbance at 450 nm, 420 nm, and 410 nm.

TABLE 2.1. Measured absorbance of InGaN MQWs from solar cell literature. Young *et al.* refers to Ref. [44]. Farrell *et al.* refers to Ref. [45].

Reference Absorption edge Substrate	Young *et al.* 450 nm Sapphire		Young *et al.* 450 nm Bulk GaN		Farrell *et al.* 500 nm Sapphire		
Number of QWs	Absorbance (%)		Absorbance (%)		Absorbance (%)		
	420 nm	410 nm	420 nm	410 nm	450 nm	420 nm	410 nm
10	17	20	19	22	11	20	23
20	24	29	28	32	16	33	35
30	33	39	36	43	20	41	45
50	43	50	53	60			

Again, solar cell literature results, like those reported in Table 2.1, differ from our work because we are focused on QWs on a semipolar plane and with longer emission wavelengths. Both growing on a semipolar plane as well as growing QWs with longer wavelength emission should increase absorbance. Because semipolar planes have decreased piezoelectric polarization-induced electric fields compared to *c*-plane, they have the advantage of improved wavefunction overlap. [18] Because of improved wavefunction overlap, QWs grown on semipolar planes are expected to have increased absorption compared to QWs grown on *c*-plane.

Additionally, our devices require QWs with long emission wavelength in order to achieve white light, and QWs with longer emission wavelength should correspondingly have red-shifted absorption spectra. As shown in Table 2.1, solar cell literature results report ~10 % absorbance at 450 nm for a 10 QW sample with an absorption edge at 500 nm. [45] Pushing the absorption edge to 560 nm might double the absorbance in blue. Additionally, as can be seen from the data in Table 2.1, absorbance is strongly dependent on wavelength. Thus, in our electrically injected and optically pumped devices, a significant increase in the absorbance of the optically pumped QWs can be produced by blue-shifting the LED emission wavelength.

Based on literature absorbance results and considering that the absorption spectrum will be red-shifted as the emission wavelength is increased, the number of optically pumped QWs to achieve acceptable absorbance is estimated to between 50 QWs and 100 QWs. As will be discussed in Chapter 3, we have not yet succeeded in optimizing growth conditions to demonstrate MQW stacks with tens of QWs, and this is an area for future work. In particular, it will be important to experimentally investigate whether initial QWs are damaged when held at growth temperature for a long time when growing tens of QWs.

In addition to the absorbance of the optically pumped QWs, there are several other factors that need to be considered in determining the number of optically pumped QWs required to achieve white light emission. First, in addition to knowing the absorption of the optically pumped QWs, we must know the radiative efficiency with which these QWs produce long wavelength light. Second, the required number of optically pumped QWs is very sensitive to the exact emission colors of the electrically injected and optically pumped QWs. Slight changes in the peak emission or width of the emission peak affect the color and, thus, the ratio of light from the optically pumped QWs compared to light from the electrically injected QWs that is required to produce white light. Third, in our proposed electrically injected and optically pumped devices, it is also possible for blue light to be re-absorbed by the electrically injected blue QWs. Fourth, extraction engineering must be considered, as this affects how much light escapes from the chip and the number of passes light will make through the QWs, with the probability of absorption increasing as a function of the number of passes. As will be discussed in Section 5.2.2, it is possible to intentionally control extraction by incorporating dichroic mirrors with high blue reflectance and high transmittance at longer wavelengths. Such dichroic mirrors provide a means to increase

absorption of the blue light by the optically pumped QWs. Thus, employing dichroic mirrors can allow for white light emission from devices with fewer optically pumped QWs.

References

[1] B. Van Daele, G. Van Tendeloo, K. Jacobs, I. Moerman, and M. R. Leys, "Formation of metallic in in InGaN/GaN multiquantum wells," *Appl. Phys. Lett.*, vol. 85, no. 19, pp. 4379–4381, 2004.

[2] M. T. Hardy, F. Wu, C.-Y. Huang, Y. Zhao, D. F. Feezell, S. Nakamura, J. S. Speck, and S. P. DenBaars, "Impact of p-GaN Thermal Damage and Barrier Composition on Semipolar Green Laser Diodes," *IEEE Photonics Technol. Lett.*, vol. 26, no. 1, pp. 43–46, Jan. 2014.

[3] W. Lee, J. Limb, J.-H. Ryou, D. Yoo, T. Chung, and R. D. Dupuis, "Influence of growth temperature and growth rate of p-GaN layers on the characteristics of green light emitting diodes," *J. Electron. Mater.*, vol. 35, no. 4, pp. 587–591, Apr. 2006.

[4] X. Chu and S. a. Barnett, "Model of superlattice yield stress and hardness enhancements," *J. Appl. Phys.*, vol. 77, no. 9, pp. 4403–4411, 1995.

[5] S. Keller, R. M. Farrell, M. Iza, Y. Terao, N. Young, U. K. Mishra, S. Nakamura, S. P. DenBaars, and J. S. Speck, "Influence of the Structure Parameters on the Relaxation of Semipolar InGaN/GaN Multi Quantum Wells," *Jpn. J. Appl. Phys.*, vol. 52, no. 8S, p. 08JC10, Aug. 2013.

[6] Y. Kawaguchi, C. Huang, Y. Wu, Q. Yan, C. Pan, Y. Zhao, S. Tanaka, K. Fujito, D. Feezell, C. G. Van de Walle, S. P. DenBaars, and S. Nakamura, "Influence of polarity on carrier transport in semipolar (20-2-1) and (20-21) multiple-quantum-well light-emitting diodes," *Appl. Phys. Lett.*, vol. 100, no. 23, p. 231110, 2012.

[7] B. Galler, M. Sabathil, A. Laubsch, T. Meyer, L. Hoeppel, G. Kraeuter, H. Lugauer, M. Strassburg, M. Peter, A. Biebersdorf, U. Steegmueller, and B. Hahn, "Green high-power light sources using InGaN multi-quantum-well structures for full conversion," *Phys. status solidi*, vol. 8, no. 7–8, pp. 2369–2371, Jul. 2011.

[8] E. Kioupakis, Q. Yan, and C. G. Van de Walle, "Interplay of polarization fields and Auger recombination in the efficiency droop of nitride light-emitting diodes," *Appl. Phys. Lett.*, vol. 101, no. 23, p. 231107, 2012.

[9] E. Kioupakis, P. Rinke, A. Schleife, F. Bechstedt, and C. G. Van de Walle, "Free-carrier absorption in nitrides from first principles," *Phys. Rev. B*, vol. 81, no. 24, p. 241201, Jun. 2010.

[10] A. David and M. J. Grundmann, "Droop in InGaN light-emitting diodes: A differential carrier lifetime analysis," *Appl. Phys. Lett.*, vol. 96, no. 10, p. 103504, 2010.

[11] C.-C. Pan, S. Tanaka, F. Wu, Y. Zhao, J. S. Speck, S. Nakamura, S. P. DenBaars, and D. Feezell, "High-Power, Low-Efficiency-Droop Semipolar (20-2-1) Single-

Quantum-Well Blue Light-Emitting Diodes," *Appl. Phys. Express*, vol. 5, no. 6, p. 062103, Jun. 2012.

[12] Y. Zhao, S. Tanaka, C.-C. Pan, K. Fujito, D. Feezell, J. S. Speck, S. P. DenBaars, and S. Nakamura, "High-Power Blue-Violet Semipolar (20-2-1) InGaN/GaN Light-Emitting Diodes with Low Efficiency Droop at 200 A/cm2," *Appl. Phys. Express*, vol. 4, no. 8, p. 082104, Jul. 2011.

[13] D. F. Feezell, J. S. Speck, S. P. DenBaars, and S. Nakamura, "Semipolar (20-2-1) InGaN/GaN Light-Emitting Diodes for High-Efficiency Solid-State Lighting," *J. Disp. Technol.*, vol. 9, no. 4, pp. 190–198, Apr. 2013.

[14] Y. Kawaguchi, C. Huang, Y. Wu, Y. Zhao, S. P. DenBaars, and S. Nakamura, "Semipolar (20-21) Single-Quantum-Well Red Light-Emitting Diodes with a Low Forward Voltage," *Jpn. J. Appl. Phys.*, vol. 52, no. 8S, p. 08JC08, Aug. 2013.

[15] S. Yamamoto, Y. Zhao, C.-C. Pan, R. B. Chung, K. Fujito, J. Sonoda, S. P. DenBaars, and S. Nakamura, "High-Efficiency Single-Quantum-Well Green and Yellow-Green Light-Emitting Diodes on Semipolar (20-21) GaN Substrates," *Appl. Phys. Express*, vol. 3, no. 12, p. 122102, Nov. 2010.

[16] Y. Enya, Y. Yoshizumi, T. Kyono, K. Akita, M. Ueno, M. Adachi, T. Sumitomo, S. Tokuyama, T. Ikegami, K. Katayama, and T. Nakamura, "531 nm Green Lasing of InGaN Based Laser Diodes on Semi-Polar {20-21} Free-Standing GaN Substrates," *Appl. Phys. Express*, vol. 2, no. 8, p. 082101, Jul. 2009.

[17] F. Wu, Y. Zhao, A. Romanov, S. P. DenBaars, S. Nakamura, and J. S. Speck, "Stacking faults and interface roughening in semipolar (20-2-1) single InGaN quantum wells for long wavelength emission," *Appl. Phys. Lett.*, vol. 104, no. 15, p. 151901, Apr. 2014.

[18] A. E. Romanov, T. J. Baker, S. Nakamura, and J. S. Speck, "Strain-induced polarization in wurtzite III-nitride semipolar layers," *J. Appl. Phys.*, vol. 100, no. 2, p. 023522, 2006.

[19] A. E. Romanov, E. C. Young, F. Wu, A. Tyagi, C. S. Gallinat, S. Nakamura, S. P. DenBaars, and J. S. Speck, "Basal plane misfit dislocations and stress relaxation in III-nitride semipolar heteroepitaxy," *J. Appl. Phys.*, vol. 109, no. 10, p. 103522, 2011.

[20] S. Nakamura, N. Iwasa, M. Senoh, and T. Mukai, "Hole Compensation Mechanism of P-Type GaN Films," *Jpn. J. Appl. Phys.*, vol. 31, no. Part 1, No. 5A, pp. 1258–1266, May 1992.

[21] A. Dussaigne, B. Damilano, J. Brault, J. Massies, E. Feltin, and N. Grandjean, "High doping level in Mg-doped GaN layers grown at low temperature," *J. Appl. Phys.*, vol. 103, no. 1, p. 013110, 2008.

[22] C. A. Hurni, J. R. Lang, P. G. Burke, and J. S. Speck, "Effects of growth temperature

on Mg-doped GaN grown by ammonia molecular beam epitaxy," *Appl. Phys. Lett.*, vol. 101, no. 10, p. 102106, 2012.

[23] X. A. Cao, S. J. Pearton, A. P. Zhang, G. T. Dang, F. Ren, R. J. Shul, L. Zhang, R. Hickman, and J. M. Van Hove, "Electrical effects of plasma damage in p-GaN," *Appl. Phys. Lett.*, vol. 75, no. 17, p. 2569, 1999.

[24] X. A. Cao, A. P. Zhang, G. T. Dang, F. Ren, S. J. Pearton, J. M. van Hove, R. A. Hickman, R. J. Shul, and L. Zhang, "Plasma damage in p-GaN," *J. Electron. Mater.*, vol. 29, no. 3, pp. 256–261, Mar. 2000.

[25] X. A. Cao, A. P. Zhang, G. T. Dang, F. Ren, S. J. Pearton, R. J. Shul, and L. Zhang, "Schottky diode measurements of dry etch damage in n- and p-type GaN," *J. Vac. Sci. Technol. A Vacuum, Surfaces, Film.*, vol. 18, no. 4, p. 1144, 2000.

[26] M. Malinverni, D. Martin, and N. Grandjean, "InGaN based micro light emitting diodes featuring a buried GaN tunnel junction," *Appl. Phys. Lett.*, vol. 107, no. 5, p. 051107, Aug. 2015.

[27] E. C. Young, B. P. Yonkee, F. Wu, S. H. Oh, S. P. DenBaars, S. Nakamura, and J. S. Speck, "Hybrid tunnel junction contacts to III–nitride light-emitting diodes," *Appl. Phys. Express*, vol. 9, no. 2, p. 022102, Feb. 2016.

[28] B. P. Yonkee, E. C. Young, C. Lee, J. T. Leonard, S. P. DenBaars, J. S. Speck, and S. Nakamura, "Demonstration of a III-nitride edge-emitting laser diode utilizing a GaN tunnel junction contact," *Opt. Express*, vol. 24, no. 7, p. 7816, Apr. 2016.

[29] J. T. Leonard, E. C. Young, B. P. Yonkee, D. a. Cohen, T. Margalith, S. P. DenBaars, J. S. Speck, and S. Nakamura, "Demonstration of a III-nitride vertical-cavity surface-emitting laser with a III-nitride tunnel junction intracavity contact," *Appl. Phys. Lett.*, vol. 107, no. 9, p. 091105, Aug. 2015.

[30] J. Neugebauer and C. G. Van de Walle, "Role of hydrogen in doping of GaN," *Appl. Phys. Lett.*, vol. 68, no. 13, p. 1829, 1996.

[31] L. Lugani, M. Malinverni, S. Tirelli, D. Marti, E. Giraud, J.-F. Carlin, C. R. Bolognesi, and N. Grandjean, "n+-GaN grown by ammonia molecular beam epitaxy: Application to regrown contacts," *Appl. Phys. Lett.*, vol. 105, no. 20, p. 202113, Nov. 2014.

[32] E. C. H. Kyle, S. W. Kaun, P. G. Burke, F. Wu, Y.-R. Wu, and J. S. Speck, "High-electron-mobility GaN grown on free-standing GaN templates by ammonia-based molecular beam epitaxy," *J. Appl. Phys.*, vol. 115, no. 19, p. 193702, May 2014.

[33] S. Fritze, A. Dadgar, H. Witte, M. Bügler, A. Rohrbeck, J. Bläsing, A. Hoffmann, and A. Krost, "High Si and Ge n-type doping of GaN doping - Limits and impact on stress," *Appl. Phys. Lett.*, vol. 100, no. 12, p. 122104, 2012.

[34] Y. Koide, H. Ishikawa, S. Kobayashi, S. Yamasaki, S. Nagai, J. Umezaki, M. Koike, and M. Murakami, "Dependence of electrical properties on work functions of metals contacting to p-type GaN," *Appl. Surf. Sci.*, vol. 117–118, no. 3, pp. 373–379, Jun. 1997.

[35] Q. Z. Liu and S. S. Lau, "A review of the metal–GaN contact technology," *Solid. State. Electron.*, vol. 42, no. 5, pp. 677–691, May 1998.

[36] M. Yamada, Y. Narukawa, and T. Mukai, "Phosphor Free High-Luminous-Efficiency White Light-Emitting Diodes Composed of InGaN Multi-Quantum Well," *Jpn. J. Appl. Phys.*, vol. 41, no. Part 2, No. 3A, pp. L246–L248, Mar. 2002.

[37] S.-N. Lee, H. S. Paek, H. Kim, T. Jang, and Y. Park, "Monolithic InGaN-based white light-emitting diodes with blue, green, and amber emissions," *Appl. Phys. Lett.*, vol. 92, no. 8, p. 081107, 2008.

[38] Chih-Feng Lu, Chi-Feng Huang, Yung-Sheng Chen, Wen-Yu Shiao, Cheng-Yen Chen, Yen-Cheng Lu, and Chih-Chung Yang, "Phosphor-Free Monolithic White-Light LED," *IEEE J. Sel. Top. Quantum Electron.*, vol. 15, no. 4, pp. 1210–1217, Jul. 2009.

[39] X. H. Wang, H. Q. Jia, L. W. Guo, Z. G. Xing, Y. Wang, X. J. Pei, J. M. Zhou, and H. Chen, "White light-emitting diodes based on a single InGaN emission layer," *Appl. Phys. Lett.*, vol. 91, no. 16, p. 161912, 2007.

[40] I.-K. Park, J.-Y. Kim, M.-K. Kwon, C.-Y. Cho, J.-H. Lim, and S.-J. Park, "Phosphor-free white light-emitting diode with laterally distributed multiple quantum wells," *Appl. Phys. Lett.*, vol. 92, no. 9, p. 091110, 2008.

[41] B. Damilano, P. Demolon, J. Brault, T. Huault, F. Natali, and J. Massies, "Blue-green and white color tuning of monolithic light emitting diodes," *J. Appl. Phys.*, vol. 108, no. 7, p. 073115, 2010.

[42] S. Jahangir, I. Pietzonka, M. Strassburg, and P. Bhattacharya, "Monolithic phosphor-free InGaN/GaN quantum dot wavelength converter white light emitting diodes," *Appl. Phys. Lett.*, vol. 105, no. 11, p. 111117, Sep. 2014.

[43] N. N. Fellows, H. Sato, Y. Lin, R. B. Chung, S. P. DenBaars, and S. Nakamura, "Dichromatic color tuning with InGaN-based light-emitting diodes," *Appl. Phys. Lett.*, vol. 93, no. 12, p. 121112, 2008.

[44] N. G. Young, R. M. Farrell, Y. L. Hu, Y. Terao, M. Iza, S. Keller, S. P. DenBaars, S. Nakamura, and J. S. Speck, "High performance thin quantum barrier InGaN/GaN solar cells on sapphire and bulk (0001) GaN substrates," *Appl. Phys. Lett.*, vol. 103, no. 17, p. 173903, 2013.

[45] R. M. Farrell, C. J. Neufeld, S. C. Cruz, J. R. Lang, M. Iza, S. Keller, S. Nakamura, S. P. DenBaars, U. K. Mishra, and J. S. Speck, "High quantum efficiency InGaN/GaN

multiple quantum well solar cells with spectral response extending out to 520 nm," *Appl. Phys. Lett.*, vol. 98, no. 20, p. 201107, 2011.

Chapter 3

Growth of Quantum Wells with Long Wavelength Photoluminescence

3.1 Introduction

The greatest challenge in realizing the novel device designs discussed in Section 2.2 is developing epitaxial design and growth conditions for the optically pumped quantum wells (QWs) for long wavelength emission. Although optically pumping QWs offers several benefits for achieving long wavelength emission, achieving long wavelength emission is still challenging for multiple reasons, which were introduced in Section 1.1.3. This chapter presents a discussion of the trends observed in developing the growth conditions and epitaxial design of the optically pumped $(20\bar{2}1)$ InGaN QWs for long wavelength emission. We examine the effects of changing epitaxial design variables, including: QW width, number of QWs, barrier thickness, limited area epitaxy (LAE), and doping profile. We also consider the effects of metalorganic chemical vapor deposition (MOCVD) growth conditions, including: growth temperature, trimethylindium (TMI) flow rate, InGaN growth rate, and barrier growth conditions.

Our initial experiments to develop optically pumped $(20\bar{2}1)$ InGaN QWs for long wavelength emission used previous literature results as a starting point. However, these published studies were not specifically about optically pumped $(20\bar{2}1)$ InGaN QWs for long wavelength emission. They included work published about trends for electrically injected

QWs and QWs with blue or green emission and QWs with longer wavelength emission grown on *c*-plane or different semipolar planes. Ultimately, we found that many of these techniques did not translate to benefiting the growth of optically pumped $(20\bar{2}1)$ InGaN QWs for long wavelength emission.

For example, in work from Toshiba published by Shioda *et al*., Saito *et al*., and Hwang *et al*. as well as from Sandia published by Koleske *et al*., AlGaN interlayers have been shown to enable *c*-plane InGaN light-emitting diodes (LEDs) with long wavelength emission. [1]–[4] We investigated AlGaN capping layers above InGaN QWs on $(20\bar{2}1)$ but did not find this epitaxial structure to enable optically pumped QWs with long wavelength emission on $(20\bar{2}1)$. The defects observed in these AlGaN interlayer InGaN/GaN multiple quantum well (MQW) samples were similar to those that were observed in samples without AlGaN interlayers. These defects will be discussed in detail below.

Similar defects also were not eliminated using growth pauses after the growth of the QW and before the growth of the barrier. This was a growth technique used by Sato *et al*., who published $(11\bar{2}2)$ LEDs with 562 nm emission and 13.4% external quantum efficiency at 7.4 A/cm^2. [5] Our experiments on $(20\bar{2}1)$ considered post-QW growth pauses ranging from 1 minute to 10 minutes. We found that post-QW growth pauses did not eliminate problematic defects in the QWs and typically resulted in a loss of indium from the QW. It was challenging to produce InGaN QWs with high indium incorporation when using a growth pause, making it difficult to achieve emission longer than approximately 540 nm from optically pumped $(20\bar{2}1)$ QWs. The biggest difference between our work and the results from Sato *et al*. is that we used the $(20\bar{2}1)$ growth plane while they used the $(11\bar{2}2)$ growth plane, which is known to have high indium uptake. [6]

Work by Zhao *et al.* considered growth of $(20\bar{2}\bar{1})$ green LEDs and reported a reduction in defects in the QWs by using very slow InGaN growth rates. [7] However, as will be discussed in Section 3.4.3, we found that very slow InGaN growth rates (with TEG flow rate corresponding to a GaN growth rate of 0.16 Å/s) produced poor results for growing optically pumped $(20\bar{2}1)$ InGaN QWs with long wavelength emission. Slower InGaN growth rates require lower growth temperature in order to produce the same indium incorporation, and the reduction in temperature required to produce long wavelength emission was problematic for material quality and radiative efficiency.

The three examples discussed here illustrate that the challenges we faced in optimizing epitaxial design and growth conditions for optically pumped $(20\bar{2}1)$ InGaN QWs with long wavelength emission. Because the results from literature did not reproduce successful results for optically pumped QWs, longer wavelength emission, or a different growth plane, we pivoted our approach towards mapping out the growth space. The first goal was to identify the variables that enabled long wavelength PL emission. As will be discussed below, we identified QW width, doping profile, and growth temperature as variables with the most significant effects on emission wavelength. Next, the goal shifted to maximizing photoluminescence (PL) emission intensity at a given long wavelength by systematically considering effect of changing each variable. In general, we found that changing growth conditions to enable slightly higher growth temperatures was usually beneficial. For example, increasing TMI flow rate or InGaN growth rate enable a higher growth temperature to be used to achieve a desired emission wavelength. Of course, increasing these variables indefinitely is not expected to be beneficial, so empirical studies

were required determine optimum conditions. Such growth studies are discussed in this chapter.

3.2 MOCVD Growth Conditions

MOCVD growths were performed at atmospheric pressure using bulk GaN substrates provided by Mitsubishi Chemical Corporation. Ammonia was used as the nitrogen source. Trimethylgallium (TMG) was the gallium source used for the high temperature growth of GaN layers grown initially on the substrates. Triethylgallium (TEG) was the gallium source used for growth of subsequent GaN layers; the TEG bubbler bath was held at 20 °C. Many layers in the device were grown at low temperature, and compared to TMG, TEG offers reduced carbon incorporation at low temperature. TMI was the indium source; the TMI bubbler bath was held at 20 °C. Silane was the source of silicon for *n*-type doping, and bis(cyclopentadienyl)magnesium (Cp_2Mg) was the source of magnesium for *p*-type doing. The temperature at the growth surface is estimated to be approximately 100 °C less than the reported thermocouple reading.

3.3 Epitaxial Device Design Variables

3.3.1 QW Width and InGaN Indium Content

Thinner QWs are appealing because thinner QWs have higher wavefunction overlap between electron and hole wavefunctions. This benefits both the radiative recombination rate as well as absorbance, although absorbance is also impacted by the number of InGaN QWs. Thinner QWs at a given indium content also have improved crystal quality because

there is less stress in the film making it less likely that the InGaN layer relaxes, [8] and both decreased stress and thinner InGaN decrease the likelihood and growth of faceting in the QW. [9]

The challenge in using thin QWs for long wavelength emission is that the emission wavelength blue-shifts for thinner QWs as the bound states for electrons and holes increase in energy. It was found experimentally that wider $(20\bar{2}1)$ QWs enable emission at longer wavelengths than can be achieved using thinner QWs grown at lower temperature for high indium content InGaN. However, it is difficult to state conclusively whether the higher indium content InGaN or lower growth temperatures are the problem in producing long wavelength emission from thinner QWs. While higher indium content InGaN leads to increased stress in the InGaN layer, lower growth temperature leads to decreased adatom diffusion and desorption, which can result in a breakdown of surface morphology, growth errors, and increased impurity incorporation. [10], [11] Lower growth temperatures also reduce the thermal energy available for overcoming kinetic barriers to defect formation. The effect of growth temperature and InGaN indium content is discussed further in Section 3.4.1.

Figure 3.1 illustrates the benefit of using wider QWs to achieve long wavelength emission. The PL emission spectra shown in Fig. 3.1 were obtained by exciting samples with a 405 nm laser. The growth sequence for the different samples was identical except for changing the growth time of the InGaN SQW—15 seconds, 25 seconds, 35 seconds, or 45 seconds. Samples were grown on $(20\bar{2}1)$ bulk GaN substrates. The sample structures consisted of an *n*-type GaN layer, a 6 nm undoped GaN layer, an InGaN SQW, a 36 nm undoped GaN layer, and a *p*-type GaN layer. The TEG flow rate for the InGaN QW

corresponded to a GaN growth rate of approximately 1.0 Å/s. All samples were grown at 805 °C.

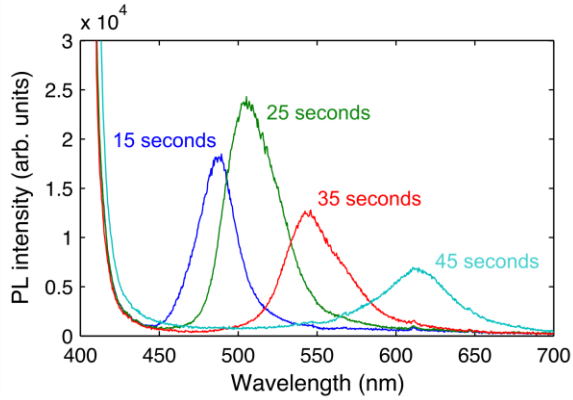

Figure 3.1. PL emission spectra for a SQW in a *p-n* junction with varying QW widths show red-shifted emission for wider QWs. Growth conditions for the samples were identical except for QW growth times of either 15 seconds, 25 seconds, 35 seconds, or 45 seconds. TEG flow rate for the InGaN QW corresponded to a GaN growth rate of 1.0 Å/s.

Figure 3.2 shows PL emission as function of decreasing growth temperature of InGaN single QWs (SQWs) in order to red-shift emission by increasing the indium content of the InGaN alloy. The colored lines replicate the data from Fig. 1, while the black lines report the result for samples that have identical growth conditions except for the growth temperature of the InGaN SQW. This figure illustrates that wider QWs achieve higher intensity PL emission at longer wavelengths than can be achieved using a thinner QW grown at a lower temperature for increased indium content InGaN.

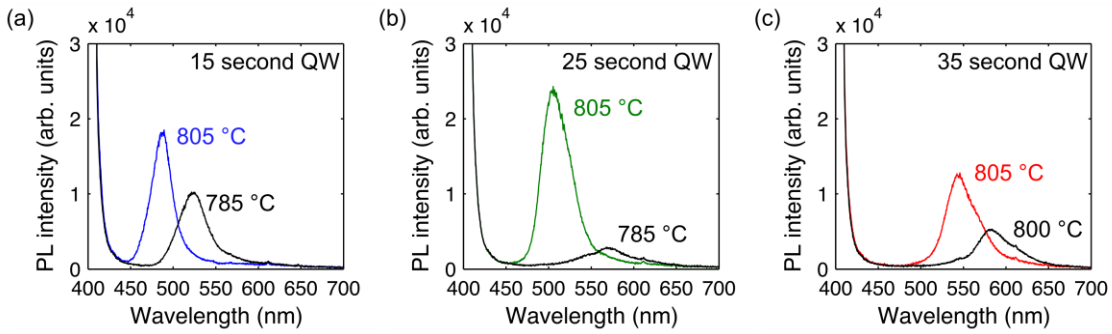

Figure 3.2. (a), (b), and (c) show PL emission spectra and the effect of decreasing growth temperature to red-shift emission from 15 seconds, 25 second, and 35 second QWs, respectively. Colored lines replicate data from Fig. 1 and black lines show comparable SQW in a *p-n* junction samples grown at lower temperature.

It is worthwhile to emphasize that the results presented here in favor of wide $(20\bar{2}1)$ QWs for long wavelength emission are based on optically pumped QWs, which may not be favorable for long wavelength emission from electrically injected QWs. For electrically injected QWs, the electric fields in an operating device are a function of the applied voltage, resulting in emission wavelength and radiative efficiency varying as a function of operating current. The emission wavelength and efficiency of electrically injected QWs differs from the performance of identical QWs under optical excitation. Typically carrier concentrations are much higher for electrical injection compared to optical excitation. Overall, optimizing for long wavelength electroluminescence (EL) is not the same as optimizing for long wavelength PL.

It is also important to mention that the majority of the following results focus on $(20\bar{2}1)$ QWs in an *n-i-n* structure. The potential benefits and challenges of using $(20\bar{2}1)$ QWs in a *p-i-n* structure are discussed in Section 3.3.5. The biggest benefit of using a *p-i-n* structure for long wavelength PL is that, for $(20\bar{2}1)$ QWs, the emission wavelength is red-shifted as compared to QWs in an *n-i-n* structure. Figure 3.1 shows the PL emission as a function of QW thickness for QWs in a *p-i-n* structure. In order to achieve comparable PL emission wavelengths using QWs in an n-*i-n* structure, wider QWs must be used. The

majority of the following results focus on $(20\bar{2}1)$ QWs in an *n-i-n* structure where the thickness of the QWs is 6 nm to 8 nm.

Lastly, faceting in the QW is suspected to be affecting the quality of MQW stacks with relatively wide QWs. It is not clear at this time whether the QW width is to blame for the defects that negatively affect the radiative efficiency of these MQWs. However, because thicker InGaN layers allow facets to grow, [9] reducing the QW width may be beneficial in preventing defects. At this time, reducing QW thickness to potentially suppress defect formation has not been extensively studied because long wavelength PL emission from $(20\bar{2}1)$ QWs in an *n-i-n* structure has only been successfully demonstrated with relatively wide QWs.

3.3.2 Number of QWs

The efficiency of III-nitride emitters decreases with increasing wavelength. This is the result of several factors, which were introduced in Section 1.1.3. First, increasing InGaN indium content, decreasing growth temperatures, and/or growing wider QWs to achieve longer wavelength emission can result in lower crystal quality leading to increased nonradiative recombination rates. Second, higher indium content InGaN and/or wider QWs have decreased electron and hole wavefunction overlap leading to decreased radiative recombination rates and increased nonradiative recombination rates, as discussed in Section 1.1.3. [12], [13]

A device with monolithically integrated electrically injected and optically pumped QWs can increase the amount of long wavelength emission by increasing the number of optically pumped QWs. The ideal device will have the correct number of optically pumped

QWs to result in uniform white light emission. Determining the number of optically pumped QWs required will be a function of the absorbance and radiative efficiency of the optically pumped QWs as well as the colors of the electrically injected and optically pumped QWs. Although the radiative efficiencies of our optically pumped QWs have not been measured, devices using a blue LED to optically pump longer wavelength QWs for white light would likely benefit from tens of QWs. Figure 3.3 shows the absorbance measured for five QWs. Samples were grown on $(20\bar{2}1)$ bulk GaN substrates. The sample structure consisted of an *n*-type GaN layer, an undoped 5× 35 nm/7 nm GaN/InGaN MQW stack, and an *n*-type GaN capping layer. Although the reflectance data is not shown, reflection accounts for the 20 % of the above the GaN bandgap intensity that was not absorbed. Reflectance was between 28 % and 30 % of light with energy below the GaN bandgap.

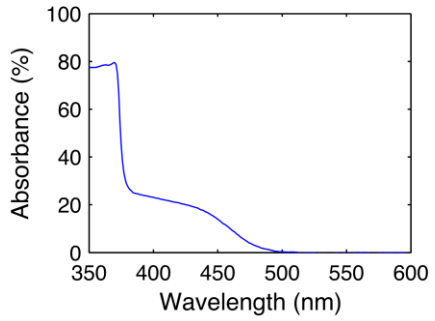

Figure 3.3. Absorbance for a five QW sample with emission peak at 455 nm was measured using spectrophotometer. Reflection accounts for the 20 % of the above GaN bandgap intensity that was not absorbed. Reflectance was between 28 % and 30 % of light with energy below the GaN bandgap.

Unfortunately, it has been difficult to achieve the growth of MQWs for long wavelength emission on $(20\bar{2}1)$. Defects are formed when growing MQWs. These defects are associated with nonradiative areas in the QWs as seen by fluorescence microscopy (FLM) and/or cathodoluminescence (CL) and features on the surface that are visible by optical microscopy, scanning electron microscopy (SEM), and/or atomic force microscopy (AFM.) The density and size of these defects increase with increasing number of QWs and

decreasing growth temperature. It is expected that the integrated PL intensity should increase with increasing number of QWs, and increasing PL intensity has been observed for increasing number of QWs with blue or green emission. For our work focused primarily on relatively wide QWs in an *n*-*i*-*n* structure, samples with peak PL emission wavelengths of 560 nm or longer did not produce increased PL intensity with increasing number of QWs. We believe that an increased density and size of defects in the QWs negatively impacted MQW samples, and sometimes the PL intensity of MQWs samples was less than the PL intensity of samples with fewer QWs.

Figures 3.4(a), 3.4(b), 3.4(c), and 3.4(d) show FLM images of samples with one, two, three, and four QWs, respectively. Defects appear as dark nonradiative spots, and the number of defects and the size of the defects can be seen to increase with increasing number of QWs. Samples were grown on $(20\bar{2}1)$ bulk GaN substrates. The sample structures consisted of an *n*-type GaN layer, either one, two, three, or four periods of undoped 35 nm/7 nm GaN/InGaN, and a thin *n*-type GaN capping layer.

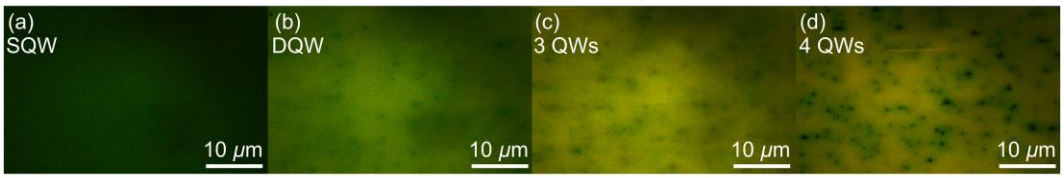

Figure 3.4. (a), (b), (c), and (d) show FLM images of SQW, DQW, triple QW, and four QW samples, respectively. Nonradiative defects in the QWs increase in size and density with increasing number of QWs.

We also investigated these defects by cross-sectional transmission electron spectroscopy (TEM). Figure 3.5 shows TEM images of a five QW stack. Samples were grown on $(20\bar{2}1)$ bulk GaN substrates. The sample structure consisted of an *n*-type GaN layer, an undoped 5× GaN/InGaN MQW stack, and an *n*-type GaN capping layer. In the MQW stack, the GaN barriers were grown for 5.5 minutes with a TEG flow of 45 sccm, and

the InGaN QWs were grown for 80 seconds with a TEG flow of 25 sccm and a TMI flow of 165 sccm. The GaN barriers and final capping layer were grown at the QW growth temperature. Figure 3.5(a) shows a lower magnification high-angle annular dark-field (HAADF) cross-sectional TEM image. This image shows defects in the QW associated with roughness on the surface. (The vertical stripes associated with these defects in the TEM images are a result of the focused ion beam (FIB) cross-section technique.) However, between these defects the five MQW stack appears free of extended defects, as shown at higher magnification in Fig. 3.5(b). Figures 3.5(c) and 3.5(d) shows both bright field and dark field TEM images for the diffraction conditions $\mathbf{g} = 000\bar{2}$ and $\mathbf{g} = 10\bar{1}0$, respectively. In these images, these defects, which create rough features on the sample surface, appear to result from faceting, basal plane stacking faults (BPSFs), and voids in the QWs. Interestingly, these defects first appear in the second QW. Lastly, Fig. 3.5(e) shows a plan view SEM image of the defects on the surface of the sample.

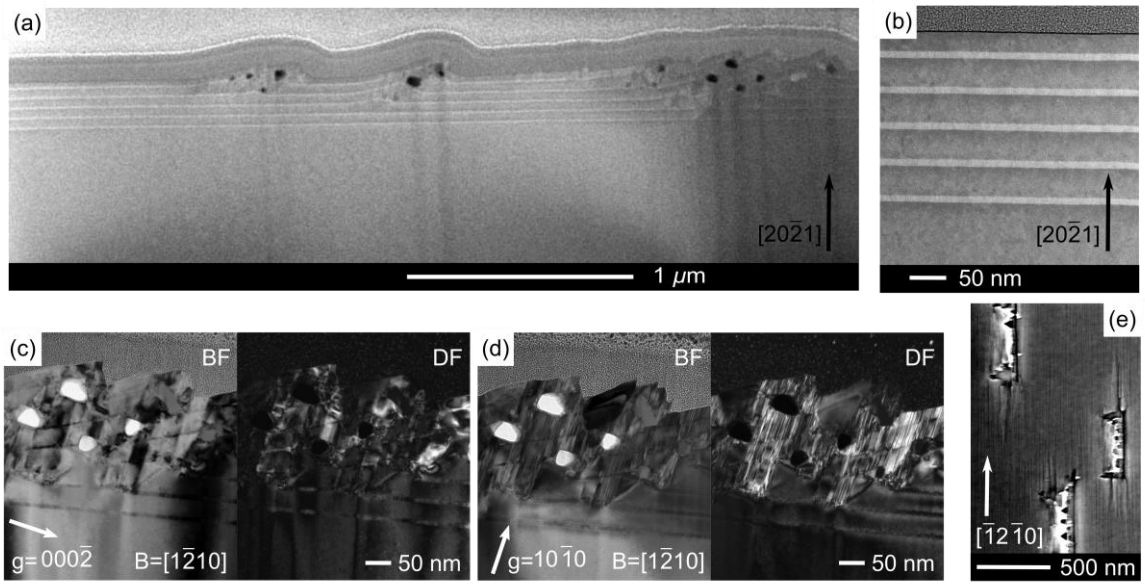

Figure 3.5. (a) and (b) are HAADF cross-sectional TEM images. (a) is taken in low magnification, some protruding surfaces are shown in the image. Under the rough surfaces, QW bending, BPSFs and voids happen. (b) is taken in higher magnification in an area without defects, the MQW are smooth and uniform. (c) and (d) are two beam BF and DF electron scattering contrast images taken under g = $000\bar{2}$ and g = $10\bar{1}0$ diffraction conditions, respectively. BPSFs are generated at the positions of bending QW. They introduce more strain and enhance the following QW bending. Voids are generated in highly defected area. (e) is a plan view SEM images of the $(20\bar{2}1)$ surface showing three protruding defects. (Images by Feng Wu.)

AFM was also used to look at the surface of samples. Figure 3.6 shows AFM images of MQW samples, where defects like those examined in Fig. 3.5 are apparent as crystallographic features on the surface. Figures 3.6(a) and 3.6(b) are height retraces, while Fig. 3.6(c) is an amplitude retrace.

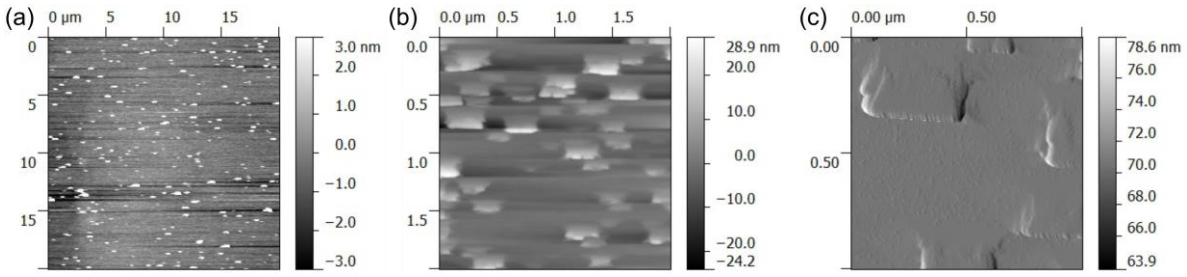

Figure 3.6. (a) and (b) are AFM height retraces of the surface of MQW samples. (c) is an AFM amplitude retrace examining the crystallographic features on the surface associated with defects in the QWs.

Section 3.4 will discuss some of the growth conditions that have been varied in an attempt to suppress the formation of these defects in MQW stacks. However, at this time, we have not succeeded in preventing these defects in MQWs with long wavelength PL emission, and the cause of these defects has not been determined. The wide QW widths, high stress in the QWs, and/or low QW growth temperatures may contribute to the formation of these defects. As will be discussed in Section 3.4.1, these defects appear to overwhelm the surface with decreasing growth temperature, though optimized growth conditions can be used to achieve longer wavelength emission before these defects dominate the surface.

3.3.3 Barrier Thickness

One of the benefits of optically pumping high indium content InGaN QWs for long wavelength emission is that thick quantum barriers (QBs) can be incorporated between QWs because the electrical resistance of the QBs and carrier transport between QWs are not a concern. Thick QBs are advantageous because they help to prevent relaxation of the InGaN QWs. [14] The MQW stack can be treated as a bulk layer with the average indium content determined by a weighted average composition of the superlattice (SL). Thus, increasing the thickness of the QB decreases the average indium content of the MQW stack, and lower indium content layers have larger critical thickness of relaxation.

The critical thickness of relaxation is the thickness to which a coherent InGaN layer can be grown before defects form that allow the InGaN layer to partially relax. The critical thickness of relaxation decreases as a function of increasing InGaN indium content and is plane dependent, with growth on semipolar planes having decreased critical thickness

compared to *c*-plane. [8] Because this work is concerned with high indium content InGaN semipolar QWs, the critical thickness of relaxation is expected to be small, i.e. on the order of nanometers. Thick QBs and the SL structure of MQW stacks can enable growth of coherent InGaN MQWs. However, growing QBs thicker than is needed to prevent relaxation requires more growth time and does not offer additional benefits.

As expected, thicker GaN QBs did help to prevent defects and increase PL intensity as shown in Fig. 3.7. Figures 3.7(a) and 3.7(b) show FLM images of samples with 30 nm and 15 nm QBs between MQWs, respectively. The dark horizontal lines in the FLM images are parallel to the *a*-direction and are basal plane misfit dislocations (MDs), which act to relieve strain in semipolar InGaN films, as discussed in Section 1.1.2. [8], [15] The thicker QBs reduced the formation of MDs. However, as seen in the FLM images, both samples have nonradiative defects in the QWs like those examined in Fig. 3.5. Although the thicker QBs did not prevent the formation of these defects in the QWs, they did enable increased PL emission intensity, as shown in Fig. 3.7(c), which compares the PL emission spectra from these samples. The PL emission spectra were obtained using a 405 nm laser as an excitation source, and the emission peak at 500 nm resulted from emission from the top QW, which was blue-shifted due to the *n*-type GaN layer grown directly above it (as will be discussed in Section 3.3.5). The samples were grown on $(20\bar{2}1)$ bulk GaN substrates. The sample structure consisted of an *n*-type GaN layer, an undoped 5× GaN/InGaN MQW stack, and an *n*-type GaN capping layer. The samples had identical QW growth conditions. The only difference between the samples was the time of the QB growth step.

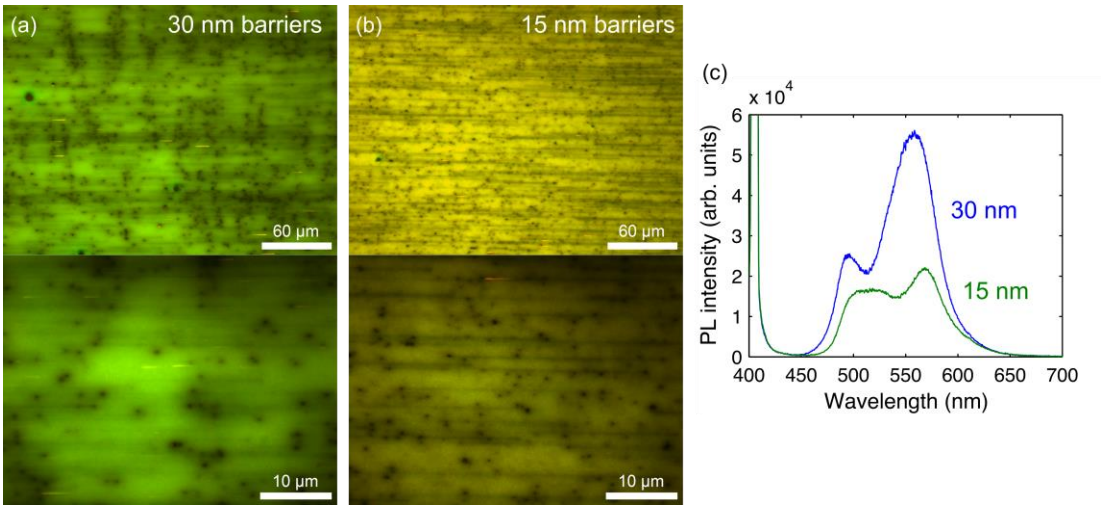

Figure 3.7. (a) and (b) show FLM images of samples with 30 nm and 15 nm QBs between MQWs, respectively. (c) shows the corresponding PL emission spectra.

3.3.4 Limited Area Epitaxy

In addition to incorporating thicker QBs, LAE is another technique that has been explored to help prevent relaxation of stressed semipolar III-nitride films, which have been shown to relax by MD formation, as discussed in Section 1.1.2. [8], [16] LAE involves patterning the substrate surface prior to growth so that physical boundaries limit the run length and number of MDs that form on the LAE device regions. [17] Previous work has shown that observed MDs in III-nitrides are formed by bend and glide of preexisting threading dislocations. [18] Thus, LAE limits the number of MDs that form on LAE device regions by using physical boundaries to determine the number of threading dislocations that can participate in MD formation. LAE has been demonstrated to enable growth of coherent III-nitride layers beyond the critical thickness of relaxation observed for comparable planar layers. [19], [20]

Because LAE is beneficial for preventing relaxation by the formation of MDs, it is not surprising that LAE did not offer improvements beyond those that could be achieved by

incorporating thick QBs in MQW stacks. Figure 3.8 shows a FLM image of a MQW sample grown on a substrate patterned prior to growth with LAE mesas. The sample was grown on $(20\bar{2}1)$ bulk GaN substrates. The sample structure consisted of an *n*-type GaN layer, an undoped 10× GaN/InGaN MQW stack, and an *n*-type GaN capping layer. The 20 μm wide mesas are seen in the upper left of the image, and the right and bottom sides of the image show areas between the LAE regions, where final devices would not be situated. The dark horizontal lines are parallel to the *a*-direction and are basal plane MDs. The growth in the non-device regions is affected by MDs with long run lengths, while the LAE device regions are affected by fewer MDs. However, as seen in the FLM image, both the non-device regions and LAE device regions have nonradiative defects in the QWs like those examined in Fig. 3.5.

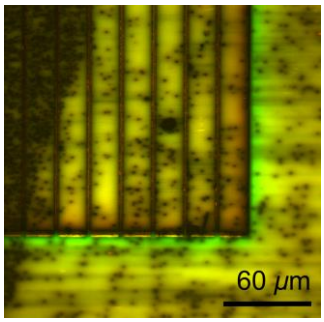

Figure 3.8. FLM of a sample patterned prior to growth for LAE shows nonradiative defects in the QWs still form on LAE mesas.

Because increasing barrier thickness is easier than LAE steps, moving forward our work focused on planar growths with thick GaN barriers to help prevent relaxation by MD formation. However, LAE could be beneficial if future work encounters a scenario where a SQW for long wavelength emission exceeds the critical thickness of relaxation and relaxes by the formation of MDs. Alternatively, LAE may be employed if optically pumped MQWs suffer from thermal damage due to QWs being held at growth temperature for too long of a

time. [21], [22] High indium content InGaN QWs grown first may suffer from decreased radiative efficiency compared to QWs grown later in a MQW stack because the first QWs have been held at elevated temperature. LAE can enable decreased growth time by preventing relaxation of MQW stacks with thinner barriers.

3.3.5 Doping

By eliminating electrical injection, built-in electric fields can instead be engineered to affect the emission wavelength of the optically pumped QWs. Specifically, by using a *p-n* junction to create a built-in electric field in the same direction as the polarization-induced electric field in the InGaN QWs, the energy of the ground state transition is decreased resulting in red-shifted emission. This enables longer wavelength emission than has been achieved from QWs in an *n-i-n* structure. Alternatively, this enables thinner or lower indium content InGaN QWs to be used in emitting a desired wavelength. Thinner QWs or lower indium content InGaN are favorable to prevent relaxation, and lower indium content InGaN can be grown at higher temperatures that are advantageous for crystal quality. A device utilizing band engineering to red-shift emission from optically pumped QWs is discussed in detail in Section 2.2.2.

However, there are also a few downsides associated with situating optically pumped QWs for long wavelength emission in a *p-i-n* structure. First, using built-in electrical fields to increase the total electric field in a QW results in increased quantum-confined Stark effect (QCSE) and so decreased electron and hole wavefunction overlap, which decreases radiative recombination and increases nonradiative recombination and is already a challenge in QWs with high InGaN indium contents required for long wavelength emission. [13] Section 1.1

introduces QCSE and decreasing electron and hole wavefunction overlap as a function of increasing InGaN indium content.

Second, when optically pumped QWs are situated in a *p*-*i*-*n* structure, they will be depleted of carriers. Increased majority carrier concentrations result in decreased minority carrier lifetimes, so doping QWs may be advantageous for radiative recombination. Work on *c*-plane has reported increased PL emission by silicon-doping GaN barriers. [23]

A third disadvantage of using a built-in electric field to red-shift emission from optically pumped QWs is that a *p*-*i*-*n* structure limits the number of QWs and/or the width of the QBs that fit within the depletion width. [24] Thicker QBs are required to prevent relaxation, [14] and MQWs are required to increase the absorbance and total emission from the optically pumped QWs. [24]–[26] Additionally, increasing the total thickness of the MQW stack in a *p*-*i*-*n* structure will result in a decreased built-in electric field. Although the depletion width constraints could be resolved by growing multiple a *p*-*i*-*n* structures, MOCVD growth constraints prevent the growth of buried *p*-type GaN layers. In MOCVD III-nitrides growth, only the final layer can be *p*-type because in order to activate the Mg acceptor, the layer must be exposed at the surface to liberate hydrogen from Mg−H complexes during an activation anneal. Buried Mg-doped layers remain passivated by hydrogen.

It is difficult to predict whether QWs situated in an *n*-*i*-*n* or *p*-*i*-*n* structure will result in higher emission intensity at a desired wavelength. There are many factors impacting PL emission intensity and many epitaxial design and growth condition variables to optimize. At this time, our work has primarily focused on optically pumped QWs situated in an *n*-*i*-*n*

structure, and correspondingly, the focus of this chapter is on optimizing conditions for long wavelength emission from optically pumped QWs in an *n*-*i*-*n* structure.

The doping profile also can impact the PL emission from QWs in an *n*-*i*-*n* structure. Specifically, many of the samples discussed in this chapter were grown on $(20\bar{2}1)$ and consisted of an *n*-type GaN layer, an undoped GaN/InGaN MQW stack, and an *n*-type GaN capping layer. As will be seen in many of the PL emission spectra, the emission from the top QW in such structures was blue-shifted due to the *n*-type GaN layer grown directly above it. Figures 3.9(a) and 3.9(b) show a simulated conduction band and the corresponding electric field, respectively, for a structure on $(20\bar{2}1)$ consisting of a 50 nm *n*-type GaN layer, an undoped 5× 35 nm/7 nm GaN/InGaN MQW stack, and a 20 nm *n*-type GaN capping layer. The unintentionally doped layers were assumed to be *n*-type with a carrier concentration of 1×10^{16} cm^{-3}. The *n*-type layers were doped with 1×10^{18} cm^{-3} silicon donors. Position x = 0 is defined to be the bottom of the epitaxial stack. The simulation was performed using the commercial package SiLENSe. Figure 3.9 shows that the electric field in the top QW is less than the electric fields in the other four QWs, which would result in shorter wavelength emission from the top QW. This is due to the *n*-type layer directly above the final QW, which creates a built-in electric field opposing the direction of the polarization-induced electric field in the QW, thus reducing the total electric field in the QW.

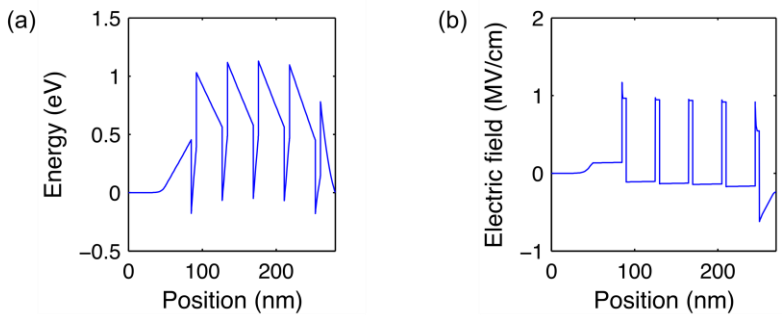

Figure 3.9. (a) and (b) are simulations of the conduction band and electric field, respectively, performed with the commercial package SiLENSe. The $(20\bar{2}1)$ structure was an *n*-type GaN layer, an undoped GaN/InGaN MQW stack, and a 20 nm *n*-type GaN capping layer. Position x = 0 corresponds to the bottom of the epitaxial stack. The top QW is seen to have a lesser electric field compared to other four QWs, which would result in a shorter emission wavelength from the top QW.

3.4 MOCVD Growth Condition Variables

3.4.1 Growth Temperature

Higher indium content InGaN requires lower growth temperatures to reduce desorption of indium from the growth surface. However, lower growth temperatures lead to decreased adatom diffusion and desorption that can result in a breakdown of surface morphology, growth errors, and increased impurity incorporation. [10], [11] Lower growth temperatures also reduce the thermal energy available for overcoming kinetic barriers to defect formation. Our experimental work has shown that growth temperature is an important variable. But because temperature is typically used to control the indium content of the InGaN alloy, it is difficult to separate whether challenges in achieving high indium content InGaN films are due lower growth temperatures or increased stress due to increased lattice mismatch between GaN and higher indium content InGaN layers. The topic of growth temperature is revisited in Section 3.4.3 where we specifically discuss low growth temperatures required for very slow InGaN growth rates (e.g., 0.16 Å/s).

As discussed in Section 3.3, the majority of our work has focused on growing relatively wide MQWs in an *n*-*i*-*n* structure for long wavelength PL emission. Growth of these MQW stacks has been found to be plagued by the formation of defects involving faceting, BPSFs, and voids. The increase in the density and size of these defects with decreasing growth temperature contributes to decreasing emission intensity for longer wavelength emitting samples grown at lower temperature. Figure 3.10 shows FLM images and corresponding PL emission spectra for samples with increasing emission wavelength. As discussed in Section 1.1.3, emission intensity is expected to decrease as a function of increasing emission wavelength. The FLM images in Fig. 3.10 show that the samples with longer wavelength emission have increasing nonradiative area due to the formation of defects, which further decreases the emission intensity of the samples with long wavelength emission. The samples in Fig. 3.10 were identical except for growth temperature. Samples were grown on $(20\bar{2}1)$ bulk GaN substrates. The sample structure consisted of an *n*-type GaN layer, an undoped 5× 35 nm/7 nm GaN/InGaN MQW stack, and an *n*-type GaN capping layer. The PL emission spectra were obtained by exciting samples with a 405 nm laser, and the emission peak at 500 nm resulted from emission from the top QW, which was blue-shifted due to the *n*-type GaN layer grown directly above it (as discussed in Section 3.3.5).

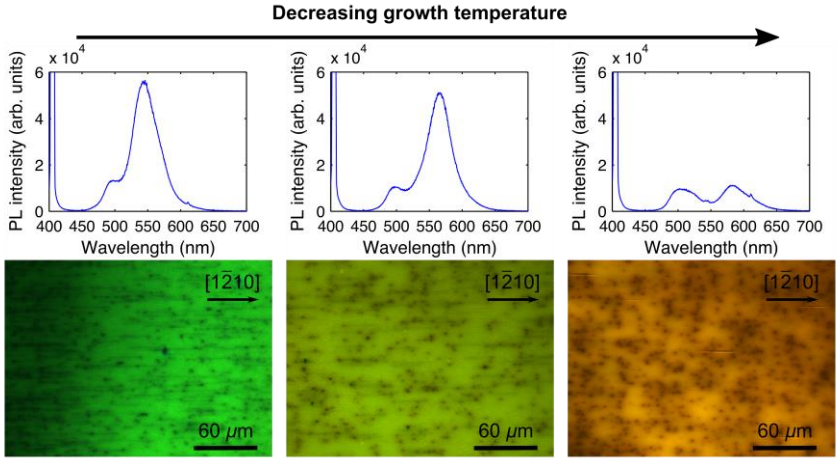

Figure 3.10. PL emission spectra and FLM images show the effect of decreasing growth temperature. Lower growth temperatures result in decreased PL intensity and more nonradiative defects in the QWs apparent in FLM images. The peak at 500 nm resulted from emission from the top QW, which was blue-shifted due to the *n*-type GaN layer grown directly above it.

For given growth conditions and epitaxial design, decreasing the growth temperature by 10 °C from a certain temperature has been found to result in catastrophic failure. In such a case, the sample grown at a hotter temperature has defects in the MQWs but areas between these defects emit long wavelength PL. However, the sample grown 10 °C colder has rough surface morphology, and the QWs do not produce significant PL emission. Sometimes the surface may appear orange, brown, or metallic. AFM and SEM of the surface of metallic samples show similarities to the features observed on the surface associated with the previously described defects in the QWs. Again, it cannot be stated conclusively whether this breakdown in surface morphology is due to low growth temperature or high stress in the InGaN films. Growth conditions affect when these defects overwhelm the surface, but we have not succeeded in preventing defects in MQW samples with long wavelength PL emission. Peak PL emission wavelengths beyond approximately 580 nm have not been achieved from MQWs in *n*-*i*-*n* structures.

Figure 3.11 shows plan view SEM images of samples grown on $(20\bar{2}1)$ bulk GaN substrates for long wavelength PL emission. The sample pictured in Fig. 3.11(a) appeared

orange to the eye. The sample pictured in Fig. 3.11(b) appeared metallic to the eye. Both of these samples did not produce PL emission. The sample pictured in Figs. 3.11(c) and 3.11(d) produced yellow PL emission but had defects in the QW. Figures 3.11(c) and 3.11(d) show defects on the surface that are similar to the image in Figs. 3.5(e) and 3.6. The defects in Figs. 3.11(c) and 3.11(d) are larger in size because this sample was a 10 QW stack. Additionally, in Fig. 3.11(c), the edge of a LAE mesa is visible, which was patterned prior to growth. Figure 3.11(d) shows one of the defects seen in Fig. 3.11(c) at a higher magnification. The metallic surface in Fig. 3.11(b) looks similar to the defects seen in Figs. 3.11(c) and 3.11(d), while the surface in Fig. 3.11(a) could be a step between a planar surface and the metallic surface. It is possible that samples that appear metallic and do not emit light may be affected by defects in the QWs that are similar to the defects imaged in Figs. 3.5 and 3.6.

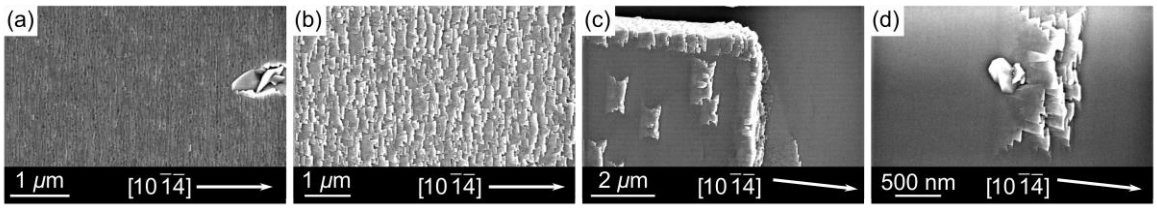

Figure 3.11. (a) and (b) show plan view SEM images of growth on $(20\bar{2}1)$ substrates show rough surfaces for samples appearing orange and metallic, respectively. (c) and (d) show SEM images of defects on the surface of a sample with yellow PL emission. The edge of a mesa patterned prior to growth is visible in (c).

Holding growth conditions other than temperature constant, we also have compared our MQWs in an *n*-*i*-*n* structure with yellow versus green PL emission. Typically yellow versus green PL emission results from a 5 °C to 10 °C decrease in growth temperature. As expected, the PL intensity of yellow QWs was less than that of green QWs. Figure 3.12 examines two samples, which were identical except for a 5 °C change in temperature resulting in the sample grown at 805 °C having green emission and the sample grown at 800

°C having yellow emission. These samples were optically pumped and electrically injected devices, as described in Section 2.2.1. A blue LED was grown on the $(20\bar{2}\bar{1})$ face of a DSP $(20\bar{2}\bar{1})/(20\bar{2}1)$ bulk GaN substrate. Subsequently, growth was performed on the $(20\bar{2}1)$ face. The structure consisted of an *n*-type GaN layer, an undoped 10× 75 nm/7 nm GaN/InGaN MQW stack, and an *n*-type GaN capping layer. Figures 3.12(a) and 3.12(e) show the PL emission spectra. The PL emission spectra were obtained by exciting samples with a 405 nm laser. The emission peak at 460 nm resulted from the $(20\bar{2}\bar{1})$ blue LED, and the emission peak at 500 nm resulted from emission from the top $(20\bar{2}1)$ QW, which was blue-shifted due to the *n*-type GaN layer grown directly above it (as discussed in Section 3.3.5).

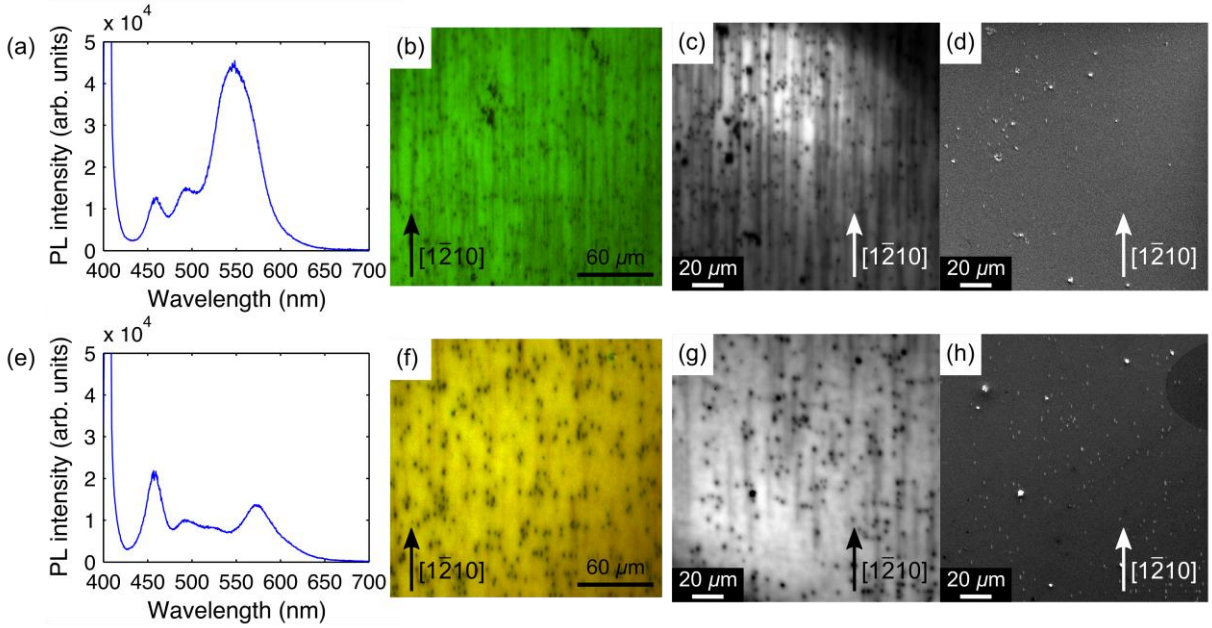

Figure 3.12. (a), (b), (c), and (d) show the PL emission spectrum and plan view FLM, CL, and SEM images, respectively, for a electrically injected and optically pumped device with optically pumped layers for long wavelength emission grown at 805 °C. (e), (f), (g), and (h) show the PL emission spectrum and plan view FLM, CL, and SEM images, respectively for an electrically injected and optically pumped device with optically pumped layers for long wavelength emission grown at 800 °C. The PL emission at 460 nm was from the blue LED, and PL emission at 500 nm was from the top optically pumped QW, which was blue-shifted due the *n*-type GaN layer grown directly above it. The lower growth temperature resulted in longer wavelength emission, larger nonradiative defects in the QWs, and fewer MDs.

Figures 3.12(b) and 3.12(f) show FLM images for the green and yellow samples, respectively. Figures 3.12(c) and 3.12(g) show CL images for the green and yellow samples, respectively, and Figs. 3.12(d) and 3.12(h) show SEM images of the surfaces matching the areas depicted in the CL images. High electron energies (30 kV) were required to penetrate to the bottom of the QW stack for CL imaging. As seen in the FLM, CL, and SEM images, both the green and yellow QWs have nonradiative defects in the QWs like those examined in Fig. 3.5, though these defects do not exist for comparable structures with shorter PL emission wavelengths of less than approximately 520 nm. In Fig. 3.12, the nonradiative areas associated with these defects appear larger for yellow QWs as compared the green QWs, and the green QWs appear to have more MDs than the yellow QWs. Because the yellow QWs were grown at a lower temperature, they have higher indium content InGaN and greater stress in the QW; these factors support the hypothesis that yellow QWs should have a greater number of MDs.[2]

At this time, it is not understood why the yellow QWs have fewer MDs compared to the green QWs, as seen, for example, in Fig. 3.12. It could be related to decreased temperature providing less thermal energy to overcome kinetic barriers (i.e. Peierls stress). Alternatively, it is possible that the defects visible on the surface are associated with relaxation. However, Fig. 3.13 shows x-ray diffraction (XRD) reciprocal space maps (RSMs) that indicate that the films are coherent as far as XRD analysis can discern. In fact, the sample used for this XRD analysis had thinner GaN barriers than most other samples and, thus, had a higher average indium content of the InGaN/GaN SL, which increased likelihood that the sample would be relaxed. The sample was grown on a $(20\bar{2}1)$ bulk GaN substrate. The sample structure consisted of an *n*-type GaN layer, an undoped 5× 18 nm/7

nm GaN/InGaN MQW stack, and an *n*-type GaN capping layer. Figure 3.13 shows RSMs about the $(20\bar{2}3)$ and $(3\bar{2}\bar{1}1)$ reflections, respectively. The $(20\bar{2}3)$ RSM is sensitive to relaxation that relieves stress in the $[1\bar{2}10]$ direction, while the $(3\bar{2}\bar{1}1)$ RSM is sensitive to relaxation that relieves stress in the $[\bar{1}014]$ direction. [15] Both RSMs in Fig. 3.13 indicate that the InGaN has remained coherently strained to the GaN.

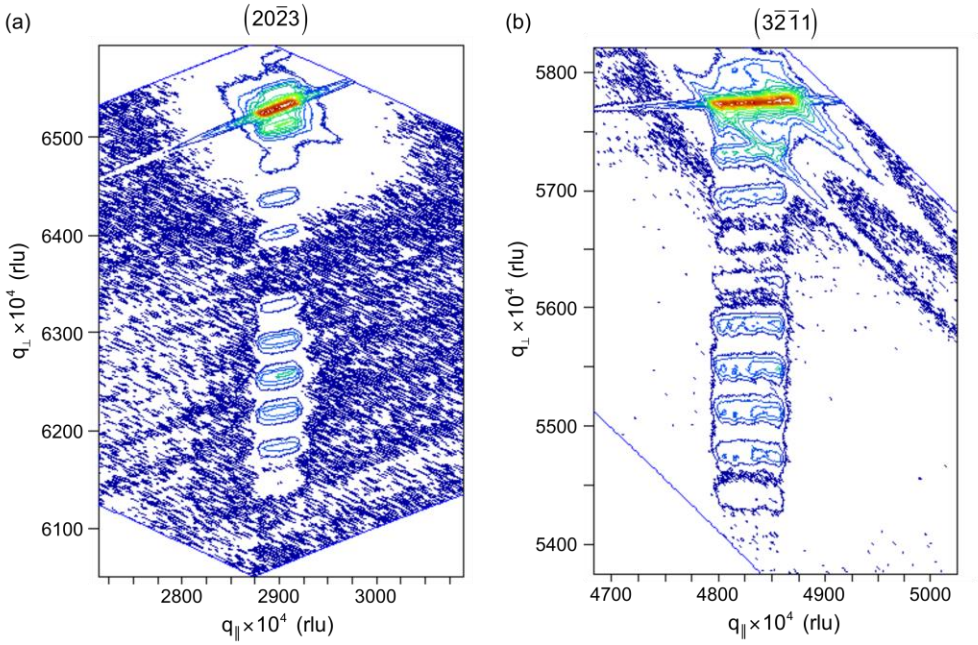

Figure 3.13. (a) and (b) are asymmetric RSMs of a $(20\bar{2}1)$ sample with five InGaN QWs about the $(20\bar{2}3)$ and $(3\bar{2}\bar{1}1)$ reflections, respectively, which show that the InGaN QWs have remained largely coherently strained to the GaN substrate.

Even if defects in QWs with long wavelength emission that are observed as nonradiative spots apparent in FLM and CL are not involved in macroscale relaxation, the formation of these defects may interfere with the formation of MDs. As shown in Fig. 3.5, these nonradiative defects in the QWs are associated with faceting, voids, and BPSFs. As discussed in Section 1.1.2, MDs relieve stress in strained InGaN QWs and form by glide of preexisting threading dislocations. If these defects associated with faceting, voids, and BPSFs are associated with preexisting threading dislocations, they could interfere with the

formation of MDs. Even if these defects apparent in QWs with long wavelength emission are not associated with preexisting threading dislocations, the faceting, voids, and BPSFs may interfere with the run length of MDs.

As mentioned in Section 3.3.1, a final consideration is that growing relatively wide InGaN QWs for long wavelength PL emission may be causing defects in MQW stacks. Thicker InGaN layers may be more likely to facet, and as discussed in Section 3.3.2, it appears that voids and BPSFs are associated with faceting.

3.4.2 TMI Flow Rate

While growth temperature is commonly used to affect indium incorporation, another way to control InGaN indium content is to adjust the TMI flow rate. Increasing the TMI flow rate while holding the TEG flow rate constant increases the indium as a percent of total Group III being introduced to the reactor. While work on *c*-plane InGaN growth has shown that indium content in the InGaN alloy saturates for increasing indium as a percent of total Group III being introduced to the reactor, [27] the indium content in the InGaN alloy as a function of indium as a percent of total Group III being introduced to the reactor is more complicated on semipolar planes because InGaN films more readily relax. If an InGaN film is grown to exceed a critical thickness, it becomes energetically favorable for the film to relax, [8] and the critical thickness for relaxation decreases for increasing InGaN indium content. When films relax, indium uptake has been found to increase dramatically. [28] Thus, for an InGaN film of a given thickness, increasing the TMI flow rate may result in a continual or even superlinear increase in the indium content of the InGaN alloy. This trend differs from observations of growth on *c*-plane, but the critical thicknesses for relaxation of InGaN films on *c*-plane are much greater than critical thicknesses on semipolar planes. The

more complicated relationship between InGaN indium content and TMI flow rate on semipolar planes may be due to relaxation of semipolar InGaN films.

Because the goal is to grow coherent InGaN films for light emission, this work focused on varying TMI flow rate to explore the effect on InGaN QWs with green and yellow PL emission. These samples were typically grown with InGaN thickness close to the critical thickness for relaxation, and thick layers were not explored. Because InGaN layers were too thin to perform XRD analysis, emission wavelength was used as a proxy for InGaN indium content. Additionally, growth of samples focused on conditions where indium as a percent of total Group III introduced to the reactor was typically greater than 50%. Lower TMI flow rates were not of interest because of the required significant decrease in growth temperature in order to achieve green and yellow emission. An advantage of higher TMI flow rates is the ability to grow at higher growth temperatures.

Although higher TMI flow rates can enable higher indium content InGaN, simply increasing the TMI flow rate may not optimize the PL emission intensity. One way in which increased TMI flow rate may negatively impact emission intensity is by increasing carbon incorporation. Additionally, point defects may more negatively impact PL than EL intensity because PL typically involves lower carrier densities. Although carbon incorporation may be affected by TMI flow rate, it is also a function of growth temperature and growth rate. Therefore, experimental work is required to optimize the combination of TMI flow rate, growth rate, and growth temperature to maximize PL emission.

Figure 3.14 shows examples of our work to understand the optimization of TMI flow rate. This figure shows PL emission spectra and FLM images for samples where temperature was used to adjust the emission wavelength to achieve comparable spectra for samples with

different TMI flow rates. A sample grown with a smaller TMI flow rate required a lower growth temperature to match the emission spectra. Other than growth temperature and TMI flow rate, the growth conditions and structure of samples being compared were identical. All samples were grown on $(20\bar{2}1)$ bulk GaN substrates with a structure consisting of an *n*-type GaN layer, an undoped 5× GaN/InGaN MQW stack, and an *n*-type GaN capping layer. The PL emission spectra were obtained by exciting samples with a 405 nm laser. An emission peak at approximately 500 nm is in all the spectra and resulted from emission from the top $(20\bar{2}1)$ QW, which was blue-shifted due to the *n*-type GaN layer grown directly above it (as discussed in Section 3.3.5).

The samples compared in Fig. 3.14(a) had TMI flow rates of 75 sccm and 100 sccm requiring growth temperatures of 765 °C and 775 °C, respectively. The 80 s QWs were grown with a TEG flow rate of 15 sccm, corresponding to a GaN growth rate of 0.50 Å/s. For these samples, the indium as a percent of total Group III being introduced to the reactor was 52 % and 59 %. The samples compared in Fig. 3.14(b) had TMI flow rates of 200 sccm and 300 sccm requiring growth temperatures of 800 °C and 810 °C, respectively. The 45 s QWs were grown with a TEG flow rate of 45 sccm, corresponding to a GaN growth rate of 1.0 Å/s. For these samples, the indium as a percent of total Group III being introduced to the reactor was 50 % and 60 %. The samples compared in Fig. 3.14(c) had TMI flow rates of 30 sccm and 45 sccm requiring growth temperatures of 775 °C and 785 °C, respectively. The 240 s QWs were grown with a TEG flow rate of 5 sccm, corresponding to a GaN growth rate of 0.16 Å/s. For these samples, the indium as a percent of total Group III being introduced to the reactor was 57 % and 66 %. The samples compared in Fig. 3.14(d) had TMI flow rates of 100 sccm and 200 sccm requiring growth temperatures of 780 °C and 800

°C, respectively. The 80 s QWs were grown with a TEG flow rate of 15 sccm, corresponding to a GaN growth rate of 0.50 Å/s. For these samples, the indium as a percent of total Group III being introduced to the reactor was 59 % and 75 %.

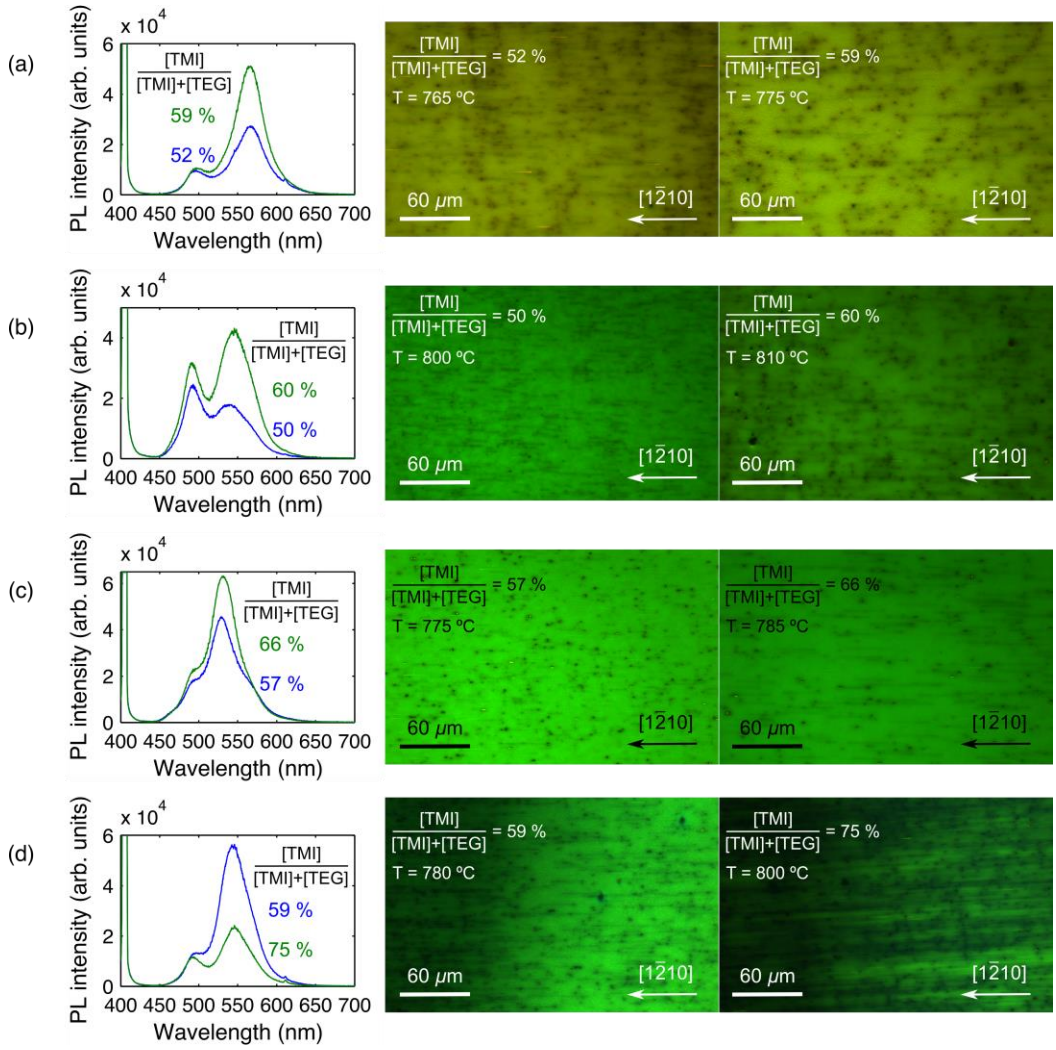

Figure 3.14. (a), (b), (c), and (d) consider different growth conditions, and for each of the growth conditions, one sample was grown with lower TMI flow rate and lower growth temperature, and a second sample grown with higher TMI flow rate and higher growth temperature, so as to result in comparable PL emission wavelengths. (a), (b), (c), and (d) are in order of increasing maximum indium as a percent of total group III introduced to the reactor, respectively. (a), (b), and (c) show increased PL intensity for the increased TMI flow rate sample. (d) shows decreased PL intensity and more MD generation for the increased TMI flow rate sample.

Figures 3.14(a), 3.14(b), and 3.14(c) show a trend that increasing TMI flow rate resulted in a higher PL emission intensity for samples at comparable emission wavelength. It is not fully understood why higher TMI flow rates produce this result, though higher growth

temperatures enabled by higher TMI flow rates are likely advantageous. However, Fig. 3.14(d) illustrates an additional complication in optimizing TMI flow rate. In this case, the higher TMI flow rate resulted in longer MDs apparent in the FLM image and decreased PL intensity compared to the sample grown with lower TMI flow rate. The high TMI flow rate for the sample in Fig. 3.14(d) represents a case where indium was 75 % of the total Group III being introduced to the reactor; this was the highest TMI to TEG ratio that we considered. The Fig. 3.14 result suggests that there is a point where increasing TMI flow is detrimental to PL emission intensity. At this time, it is unclear how high TMI flow rate affected the relaxation by MD formation. It is possible that the high TMI flow sample in Fig. 3.14(d) had higher indium content InGaN or thicker InGaN QWs or that the indium affected the kinetics of MD formation.

3.4.3 InGaN Growth Rate

Literature results illustrate that slower growth rates are advantageous for improving material quality. Although GaN layers in an LED may be grown at upwards of 4 μm/hr, the InGaN layers are grown closer to 1 Å/s. Specifically, Zhao *et al.* considered growth of green electrically injected $(20\bar{2}\bar{1})$ LEDs and reported that slower growth rates of 0.15 Å/s reduced dark triangle defects, [7] which have been shown to be stacking faults associated with voids. [7], [22] However, slower InGaN growth rates require lower growth temperatures, and as discussed in Section 3.4.1, low growth temperatures become problematic when pushing towards longer wavelength emission.

Faster growth rates enable higher indium content InGaN. [29] While it is well known that the growth rate of GaN is linear as function of the flow of the gallium precursor, it is

also well established that increasing the metalorganic (MO) precursor flows by, for example, a factor of two does not lead to the same indium content InGaN grown at twice the growth rate. Increasing the MO precursor flows and maintaining the same indium as a percent of total Group III being introduced into the reactor will increase the InGaN growth rate and also increase the InGaN indium content by incorporating indium adatoms before they have time to desorb from the surface. Because faster growth rates result in higher indium content InGaN layers, they may be favorable for achieving long wavelength emission. However, fast growth rates decrease adatom diffusion lengths, which can lead to growth errors or breakdown of surface morphology. The effects of changing InGaN growth rate need to be experimentally studied. Ultimately, growth conditions need to optimize InGaN growth rate, TMI flow, and growth temperature, all of which impact InGaN indium content and InGaN crystal quality.

Figure 3.15(a) shows the normalized PL spectra for two samples with different InGaN growth rates. The samples were grown on $(20\bar{2}1)$ bulk GaN substrates. The sample structure consisted of an *n*-type GaN layer, an undoped 5× GaN/InGaN MQW stack, and an *n*-type GaN capping layer. The layers after the initial *n*-type layer were grown at 775 °C. The GaN barriers were grown for 10 minutes with TEG = 15 sccm. For the sample with emission corresponding to the blue curve in Fig. 15(a), the InGaN QWs were grown for 240 s with TEG = 5 sccm and TMI = 30 sccm. For the sample with emission corresponding to the green curve in Fig. 12(a), the InGaN QWs were grown for 80 s with TEG = 15 sccm and TMI = 100 sccm. The GaN growth rate for a TEG flow rate of 15 sccm was 0.50 Å/s and for a TEG flow rate of 5 sccm was 0.16 Å/s. The PL emission spectra were obtained by exciting samples with a 405 nm laser. The emission peaks at 500 nm resulted from emission from the

top $(20\bar{2}1)$ QW, which was blue-shifted due to the *n*-type GaN layer grown directly above it (as discussed in Section 3.3.5).

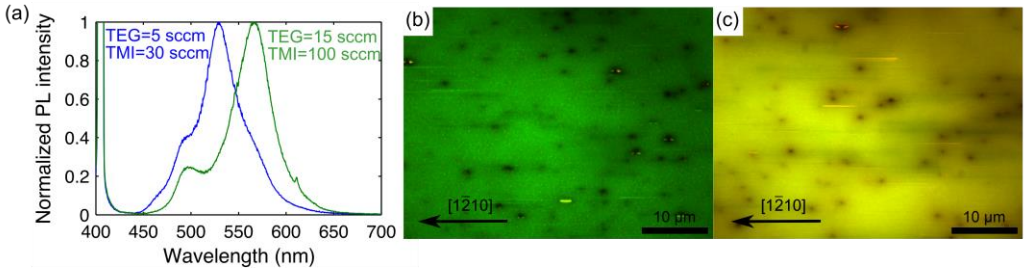

Figure 3.15. (a) shows the normalized PL spectra for a sample with very slow InGaN growth rate of approximately 0.16 Å/s (blue line) and a sample with faster InGaN growth rate of 0.50 Å/s (green line). Higher InGaN growth rate resulted in red-shifted emission. (b) and (c) show FLM images of the slow and faster InGaN growth rate samples, respectively. Both FLM show similar nonradiative defects in the QWs.

As expected, Fig. 3.15 shows that the faster InGaN growth rate resulted in red-shifted emission with a peak at 560 nm compared to the peak at 535 nm for the slower InGaN growth rate. It is expected that the faster InGaN growth rate resulted in higher indium content InGaN. In order to achieve 560 nm emission from a sample with the slower growth rate, the temperature would need to be decreased. Typically, to shift the emission from 535 nm to 560 nm would require approximately a 20 °C decrease in growth temperature. However, using the slower InGaN growth rate and decreasing the growth temperature resulted in rough samples with no emission. The slow InGaN growth rate has not achieved long wavelength emission comparable to that achieved for faster InGaN growth rate.

Figures 3.15(b) and 3.15(c) show FLM images of the previous described slower and faster InGaN growth rate samples, respectively. It is interesting to observe that both samples have similar defects apparent as nonradiative areas in the QWs like those examined in Fig. 3.5. The slower growth rate did not prevent these defects from forming.

A similar study compared InGaN grown with TEG flow rate corresponding to a GaN growth rates of 0.50 Å/s and 1.0 Å/s. The TMI was linearly increased based on the increase in TEG flow rate. The faster growth resulted in red-shifted emission, so the growth temperature was adjusted to result in comparable PL emission wavelengths. In this case, the difference in InGaN growth rate did not result in a significant decrease in the PL emission intensities for the two samples with matching PL emission wavelength. InGaN growth rates faster than 1.0 Å/s were not investigated, but we expect that continuing to increase the InGaN growth rate would become detrimental.

Unfortunately, it is difficult to experimentally measure InGaN growth rates and InGaN indium content for high indium content InGaN films on semipolar planes because the layers must be thin in order to prevent relaxation, which would affect the indium uptake of the layer. [28] Therefore, it cannot be conclusively stated how increasing the TMI and TEG flow rates affect the InGaN growth rate. It is possible that doubling the TMI and TEG flow rates may more than double or less than double the InGaN growth rate.

Additionally, as discussed in Section 3.4.2, the TMI flow rate affects PL emission intensity. As presented in this section, InGaN indium content increases at higher InGaN growth rates when the ratio of TEG to TMI flow rates is held constant. This change in indium incorporation suggests that the optimizing the TMI flow may depend on InGaN growth rate. However, the work presented in this section has not attempted to study this variable, as TMI flow rate also may impact growth rate as well as indium content.

Overall, our experimental results indicate that very slow InGaN growth rates (e.g., 0.16 Å/s) are problematic in achieving long wavelength emission. Slow InGaN growth rate requires lower growth temperature to achieve emission wavelengths comparable to faster

InGaN growth rates at higher growth temperatures. Samples grown with very slow InGaN growth rate at low temperature have not produced comparably long emission wavelengths. Assuming InGaN growth rate changes by approximately the same factor as TEG and TMI flow rates, the goal of decreasing the growth temperature for slow InGaN growth rates is to match the indium composition achieved by faster growth rates. This suggests that it is not inherently the higher indium content that is problematic, but that the low growth temperature and/or slow InGaN growth rate is preventing the successful growth of structures that can be achieved with faster InGaN growth rates.

Lower growth temperatures are problematic because they lead to decreased adatom diffusion and desorption that can result in a breakdown of surface morphology, growth errors, and increased impurity incorporation. [10], [11] Lower growth temperatures also impact growth because they reduce the thermal energy available for overcoming kinetic barriers to defect formation. On the other hand, slower InGaN growth rates increase adatom diffusion lengths, which can enable 2D step flow growth. However, it is also possible that low growth rates may become problematic as they promote faceting, which has been correlated with defect formation.[35]

3.4.4 Barrier Growth Rate

The QB growth rate was found to have a significant impact on emission wavelength. Faster QB growth rates produced red-shifted emission. [30] We hypothesize that faster QB growth rates helped retain indium in the InGaN QW during barrier growth by burying the InGaN QW more quickly, since indium exposed at the surface may desorb. Similarly, the faster QB growth rate may also have affected the InGaN/GaN interface abruptness. Figures

3.16(a) and 3.16(b) show FLM images comparing samples with faster and slower QB growth rates, respectively. The samples were grown on $(20\bar{2}1)$ bulk GaN substrates. The sample structure consisted of an *n*-type GaN layer, an undoped 5× GaN/InGaN MQW stack, and an *n*-type GaN capping layer. The samples both had 80 second QWs grown with TEG = 25 sccm and TMI =165 sccm, with TEG = 25 sccm corresponding to a GaN growth rate of 0.50 Å/s. The sample depicted in Fig. 3.16(a) had a faster GaN QB growth rate than the sample depicted in Fig. 3.16(b), with TEG = 25 sccm for 10 minutes and TEG = 45 sccm for 5.5 minutes, respectively. The QB growth times were scaled to produce QBs of the same thickness in both samples. Additionally, the sample in Fig. 3.16(a) was grown 5 °C hotter than the sample in Fig. 3.16(b). Despite the higher temperature, the sample with the faster QB growth rate produced longer wavelength PL emission with a peak at 585 nm compared to the PL peak emission of 560 nm for the sample with the slower QB growth rate. The effect of the slightly increased growth temperature was overcome by the effect of the faster GaN QB growth rate to produce longer wavelength emission as compared to the sample with a slower QB growth rate.

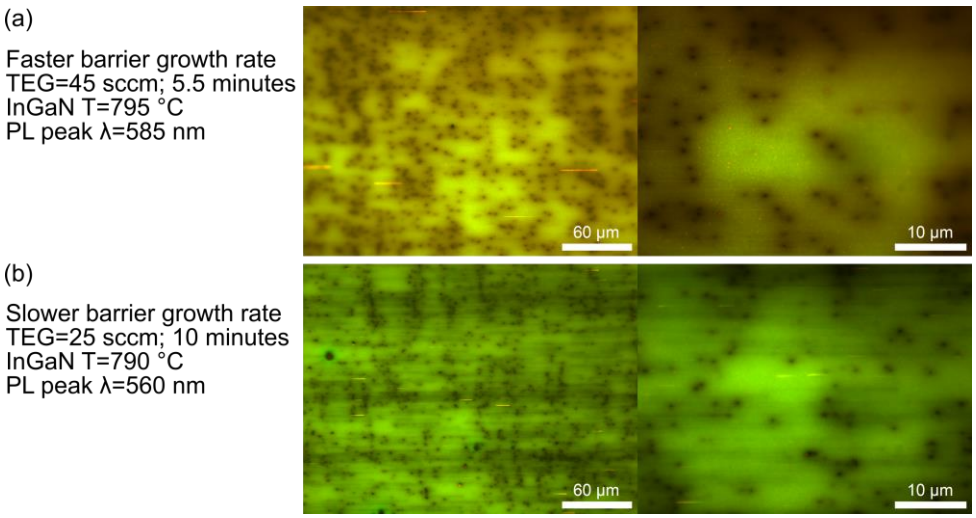

Figure 3.16. (a) and (b) show FLM images of samples with faster and slower QB growth rates, respectively. Faster growth rate resulted in red-shifted emission. Slower growth rate did not prevent formation of nonradiative defects in the QWs.

The FLM images in Fig. 3.16 show that for both the slower and faster QB growth rates, there are nonradiative defects in the QWs like those examined in Fig. 3.5. Although slower growth rate enables longer adatom surface diffusion lengths, slower QB growth rate did not prevent the formation of these defects.

3.4.5 Barrier Carrier Gas and Growth Temperature

Improved PL emission intensity is expected if conditions are developed that prevent the formation of nonradiative defects in the QWs like those examined in Fig. 3.5. QB carrier gas and growth temperature were explored as variables that might affect the formation of these defects. Work on *c*-plane MQW devices has demonstrated improved results by growing QBs at a higher temperature and in H_2/N_2 instead of N_2 carrier gas. [24], [31], [32] Both high temperature and the presence of H_2 are favorable for GaN growth on *c*-plane because they increase adatom surface mobility. [33] However, lower growth temperatures and N_2 may are often used for QB growth because these conditions are required for InGaN

growth. Low temperatures decrease indium desorption from the growth surface, and InGaN is grown in N_2 because H_2 acts to etch indium from the growth surface, which prevents indium incorporation. [34]

Growth on *c*-plane is affected by the formation of V-defects on preexisting threading dislocations. These defects form during low temperature III-nitride growth by MOCVD and then propagate outward, increasing in size. [35] Using higher growth temperatures and H_2/N_2 carrier gas for QB growth increases adatom surface mobility, which effectively allows for V-defects to be filled in and for smooth surface morphology to be recovered during the QB growth. [24], [31], [32] Although growth on semipolar planes does not form V-defects, the nonradiative defects in the QWs like those examined in Fig. 3.5 do produce features on the surface, as also seen in Figs. 3.6 and 3.11, and TEM has shown that large voids are associated with these defects. QB carrier gas and growth rate were considered as variables that might allow smooth surface morphology to be recovered during QB growth, especially because the QB were very thick. The thick QBs were suspected to be contributing to the growth of these nonradiative defects, which were seen to increase in size with increasing number of QWs in the MQW stack.

Figure 3.17 compares two samples, one with the QBs grown in H_2/N_2 and one with the QBs grown in N_2. The sample grown in N_2 had only N_2 flowing into the reactor during QB growth. The sample with QBs grown in N_2 was the control, as most samples for our experiments had QBs grown in N_2. The sample grown in H_2/N_2 had a mixture of H_2 and N_2 flowing into the reactor during QB growth. These carrier gases are flowed through the subflow and the lines used to pick up and deliver the MO precursors, as well as through the line for silane and ammonia. Unfortunately, changing the QBs to be grown in H_2/N_2 instead

of N_2 did not prevent the formation of defects in the QWs, as can be seen in Figs. 3.17(a) and 3.17(b), which show FLM images of the samples with QBs grown in H_2/N_2 and N_2, respectively. Additionally, Fig. 3.17(c) shows the PL emission spectra of these samples, and while the samples have similar PL wavelength, the sample grown in N_2 has a higher PL emission intensity. The reason for this difference has not been explained. The PL spectra in Fig. 3.17(c) were obtained using a 405 nm laser as an excitation source, and the emission peaks at 500 nm resulted from emission from the top $(20\bar{2}1)$ QW, which was blue-shifted due to the *n*-type GaN layer grown directly above it (as discussed in Section 3.3.5).

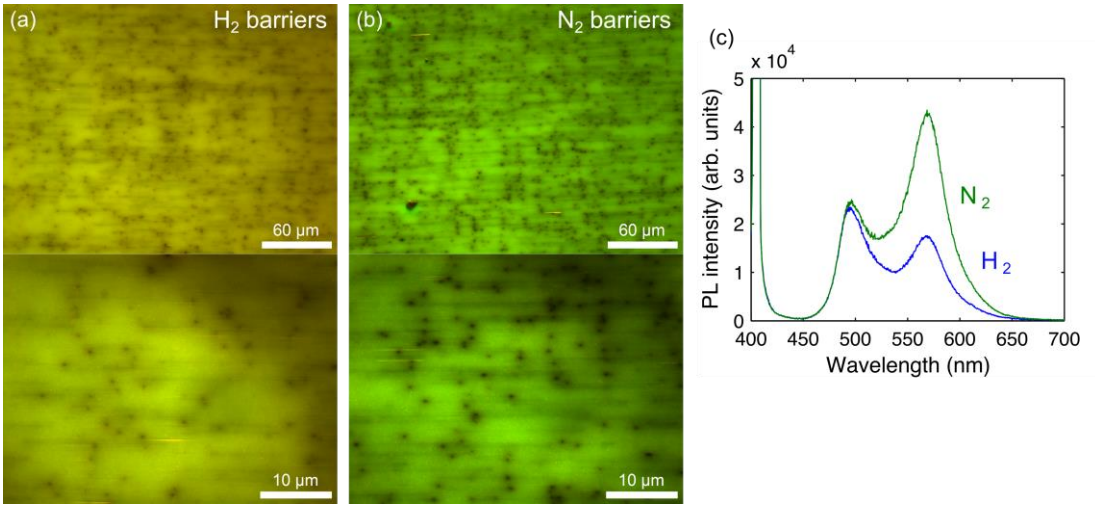

Figure 3.17. (a) and (b) show FLM images of samples with QBs grown in H_2/N_2 and N_2, respectively. Growth in H_2/N_2 did not prevent formation of nonradiative defects in the QWs. (c) shows the corresponding PL spectra.

The samples depicted in Fig. 3.17 were grown on $(20\bar{2}1)$ bulk GaN substrates, and the sample structure consisted of an *n*-type GaN layer, an undoped 5× GaN/InGaN MQW stack, and an *n*-type GaN capping layer. The QW growth conditions were identical. The QBs grown in N_2 were grown for 10 minutes with TEG = 25 sccm, which corresponded to a growth rate of 0.50 Å/s. The QBs grown in H_2/N_2 were initially grown for 2 minutes with TEG = 25 sccm in N_2 before H_2 was introduced to the reactor for an additional 8 minutes of

QB growth. This 2-step growth process caps the InGaN to protect the QW before H_2 is introduced to the reactor, as exposing the InGaN to H_2 decreases the InGaN indium content. [24], [31], [32] After QB growth, the carrier gas was then changed back from H_2/N_2 to N_2 and growth was paused for 2 minutes to ensure that H_2 had been completely removed from the reactor prior to the growth of InGaN.

Although growing the QBs in H_2/N_2 instead of N_2 did not eliminate the nonradiative defects in the QWs like those examined in Fig. 3.5, AFM did reveal a change in the surface morphology. Figure 3.18 shows the surfaces of a variety of MQW samples grown in N_2. These samples or areas of these samples were selected because they are free of large defects on the surface. Figure 3.6 shows AFM images of defects on the surface, which are associated with nonradiative defects in the QWs. However, the areas between these samples are smooth, as is also captured by the TEM images in Fig. 3.5. The AFM images in Fig. 3.18 better show what surface morphology looks like by either measuring between defects or measuring samples with shorter emission wavelengths where there were fewer defects. Samples with fewer defects and shorter wavelength emission have been confirmed to have similar surface morphology as the areas between defects on samples with longer emission wavelengths. As can be seen in Fig. 3.18, the surface morphology of these samples can vary between samples and between different areas on the same sample, but overall, samples surfaces are smooth.

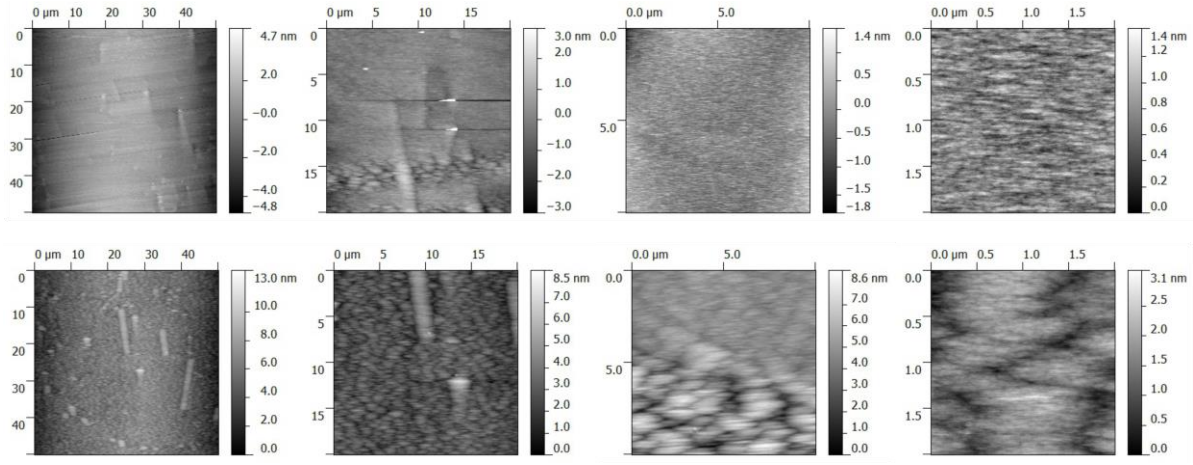

Figure 3.18. AFM of MQW samples with QBs grown in N_2 show smooth surfaces, though the surface morphology varies in appearance between samples and between different areas on the same sample.

Figure 3.19 shows an AFM image of a MQW sample grown in H_2/N_2, with the 2-step QB growth process described above where an initial GaN capping layer was grown in N_2 to protect the InGaN QW from exposure to H_2. While samples with QBs grown in N_2 and H_2/N_2 are both smooth, as shown in Figs. 3.18 and 3.19, respectively, the surface morphology of samples with QBs grown in H_2/N_2 looks different than samples grown in N_2. The surface of the sample with QBs grown in H_2/N_2 appears to have a more striated pattern, with the striations running along the *a*-direction.

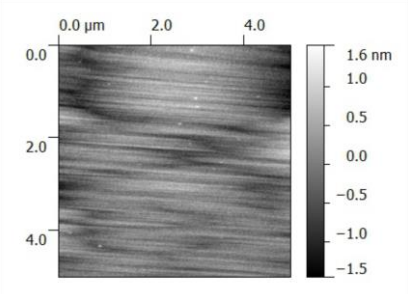

Figure 3.19. AFM of a MQW sample with QBs grown in H_2/N_2.

In addition to exploring QB growth in H_2/N_2 versus N_2, the effect of high temperature QBs was also considered. Experiments compared MQW stacks in which QBs were grown at the same temperature as the InGaN QWs and in which QBs were grown at

elevated temperature compared to the InGaN QWs. The sample with low temperature QBs was the control, as most samples for our experiments had low temperature QBs. For the high temperature QBs, the growth procedure had no growth pause after the QW, and GaN was grown during a fast ramp to a higher temperature. After growth of the QB, growth was paused to allow the temperature to cool down to InGaN growth temperature. The samples in which QBs were grown at higher temperatures had decreased PL intensity compared to the samples in which QBs were grown at the same temperature as the InGaN QWs. This agrees well with previous work that has shown high temperature growth steps can degrade high indium content InGaN. [21], [22]

A more complete study of the effect of high temperatures was performed on optically pumped QWs situated in a *p*-*i*-*n* structure. As discussed in Sections 2.2.2 and 3.3.5, *p*-*i*-*n* structures can be used to red-shift emission from optically pumped QWs. Typically *p*-type GaN for electrically injected devices is grown at high temperature to ensure adequate *p*-type conductivity. Therefore, it was of interest to investigate whether *p*-type GaN grown after optically pumped, high indium content InGaN QWs could be grown at high temperature. Table 3.1 summarizes the results. The samples were grown on $(20\bar{2}1)$ bulk GaN substrates. The sample structure consisted of an *n*-type GaN layer, an undoped GaN layer, an undoped GaN/InGaN active region, and an *p*-type GaN capping layer. The GaN/InGaN active regions were grown at 805 °C and had 1, 2, or 5 InGaN QWs, with the MQWs separated by 35 nm GaN barriers. For symmetry, the structures had 35 nm undoped GaN barriers adjacent to both the *n*-type and *p*-type layers. The effect of high growth temperature was investigated by growing samples in which the *p*-type GaN capping layer was grown at either 805 °C, 905 °C, or 955 °C. As shown in Table 3.1, both the SQW and MQW samples produced long

wavelength PL emission when the *p*-type GaN was grown at the same temperature as the InGaN QWs. However, when the *p*-type GaN was grown 100 °C hotter than the active region, the MQW samples did not produce PL emission, though the SQW did produce long wavelength PL emission. When the *p*-type GaN was grown 150 °C hotter than the active region, the both the SQW and MQW samples did not produce PL emission. These experiments indicate that high temperature growth steps are detrimental InGaN QWs, especially in MQW stacks. This is similar to results from Kawaguchi *et al.*, which reported improved performance of red $(20\bar{2}1)$ InGaN LEDs with decreasing growth temperature of the *p*-type GaN layers. [36]

TABLE 3.1. PL emission from QWs grown at 805 °C with varying growth temperature of *p*-type GaN capping layer.

Number of QWs	p-type GaN growth temperature (°C)	PL emission wavelength (nm)
1	805	610
5	805	610
1	905	600
2	905	no PL
5	905	no PL
1	955	no PL

3.5 Future Work on Growth of QWs with Long Wavelength PL

For the most part, the results in this chapter focused on optimizing epitaxial design and growth conditions for long wavelength emission from optically pumped $(20\bar{2}1)$ InGaN QWs situated in an *n*-*i*-*n* structure, which has necessitated the use of relatively wide QWs in order to achieve long wavelength emission. However, as discussed in Sections 2.2.2 and 3.3.5, band engineering can be used to red-shift emission from optically pumped QWs. This

can enable lower indium content InGaN and/or thinner QWs to be used in achieving long wavelength emission, both of which are beneficial for crystal quality. [8] Future work on the growth of QWs for long wavelength PL should focus on exploring lower indium content InGaN and/or thinner QWs situated in a *p*-*i*-*n* junction.

One of the biggest challenges in the growth of optically pumped QWs for long wavelength emission in an *n*-*i*-*n* structure is the formation of nonradiative defects in the QWs, which limit the extent to which increasing the number of QWs results in increased emission intensity. At this time, the reason that these defects form has not been determined. They may be due to utilizing wide QWs, growing at low temperatures, and/or having high stress in the QWs due to the large lattice mismatch between high indium content InGaN and GaN. Therefore, it is possible that using a *p*-*i*-*n* structure to red-shift emission from a thinner QW may help to eliminate defects and realize structure with many QWs. Similarly, it is possible that using a *p*-*i*-*n* structure to red-shift emission from lower indium content InGaN grown at higher temperature may help to eliminate these defects. As discussed in Section 3.4.1, significant differences were observed in comparing MQW stacks with green and yellow emission. This suggests that improved results may be realized by using band engineering to red-shift emission from green QWs towards yellow or longer wavelength emission. While band engineering holds potential for realizing improved long wavelength emission from optically pumped MQW stacks, this area has not been systematically explored and is a priority for future work.

References

[1] T. Shioda, H. Yoshida, K. Tachibana, N. Sugiyama, and S. Nunoue, "Enhanced light output power of green LEDs employing AlGaN interlayer in InGaN/GaN MQW structure on sapphire (0001) substrate," *Phys. status solidi*, vol. 209, no. 3, pp. 473–476, Mar. 2012.

[2] S. Saito, R. Hashimoto, J. Hwang, and S. Nunoue, "InGaN Light-Emitting Diodes on c -Face Sapphire Substrates in Green Gap Spectral Range," *Appl. Phys. Express*, vol. 6, no. 11, p. 111004, Nov. 2013.

[3] J.-I. Hwang, R. Hashimoto, S. Saito, and S. Nunoue, "Development of InGaN-based red LED grown on (0001) polar surface," *Appl. Phys. Express*, vol. 7, no. 7, p. 071003, Jul. 2014.

[4] D. D. Koleske, A. J. Fischer, B. N. Bryant, P. G. Kotula, and J. J. Wierer, "On the increased efficiency in InGaN-based multiple quantum wells emitting at 530–590nm with AlGaN interlayers," *J. Cryst. Growth*, vol. 415, pp. 57–64, Apr. 2015.

[5] H. Sato, R. B. Chung, H. Hirasawa, N. Fellows, H. Masui, F. Wu, M. Saito, K. Fujito, J. S. Speck, S. P. DenBaars, and S. Nakamura, "Optical properties of yellow light-emitting diodes grown on semipolar (11-22) bulk GaN substrates," *Appl. Phys. Lett.*, vol. 92, no. 22, p. 221110, 2008.

[6] Y. Zhao, Q. Yan, C.-Y. Huang, S.-C. Huang, P. Shan Hsu, S. Tanaka, C.-C. Pan, Y. Kawaguchi, K. Fujito, C. G. Van de Walle, J. S. Speck, S. P. DenBaars, S. Nakamura, and D. Feezell, "Indium incorporation and emission properties of nonpolar and semipolar InGaN quantum wells," *Appl. Phys. Lett.*, vol. 100, no. 20, p. 201108, 2012.

[7] Y. Zhao, F. Wu, C.-Y. Huang, Y. Kawaguchi, S. Tanaka, K. Fujito, J. S. Speck, S. P. DenBaars, and S. Nakamura, "Suppressing void defects in long wavelength semipolar (20-2-1) InGaN quantum wells by growth rate optimization," *Appl. Phys. Lett.*, vol. 102, no. 9, p. 091905, 2013.

[8] A. E. Romanov, E. C. Young, F. Wu, A. Tyagi, C. S. Gallinat, S. Nakamura, S. P. DenBaars, and J. S. Speck, "Basal plane misfit dislocations and stress relaxation in III-nitride semipolar heteroepitaxy," *J. Appl. Phys.*, vol. 109, no. 10, p. 103522, 2011.

[9] F. Wu, Y. Zhao, A. Romanov, S. P. DenBaars, S. Nakamura, and J. S. Speck, "Stacking faults and interface roughening in semipolar (20-2-1) single InGaN quantum wells for long wavelength emission," *Appl. Phys. Lett.*, vol. 104, no. 15, p. 151901, Apr. 2014.

[10] R. a. Oliver, M. J. Kappers, C. J. Humphreys, and G. A. D. Briggs, "Growth modes in heteroepitaxy of InGaN on GaN," *J. Appl. Phys.*, vol. 97, no. 1, p. 013707, 2005.

[11] S. Kim, K. Lee, K. Park, and C.-S. Kim, "Effects of barrier growth temperature on the properties of InGaN/GaN multi-quantum wells," *J. Cryst. Growth*, vol. 247, no. 1–2, pp. 62–68, Jan. 2003.

[12] A. David and M. J. Grundmann, "Droop in InGaN light-emitting diodes: A differential carrier lifetime analysis," *Appl. Phys. Lett.*, vol. 96, no. 10, p. 103504, 2010.

[13] E. Kioupakis, Q. Yan, and C. G. Van de Walle, "Interplay of polarization fields and Auger recombination in the efficiency droop of nitride light-emitting diodes," *Appl. Phys. Lett.*, vol. 101, no. 23, p. 231107, 2012.

[14] S. Keller, R. M. Farrell, M. Iza, Y. Terao, N. Young, U. K. Mishra, S. Nakamura, S. P. DenBaars, and J. S. Speck, "Influence of the Structure Parameters on the Relaxation of Semipolar InGaN/GaN Multi Quantum Wells," *Jpn. J. Appl. Phys.*, vol. 52, no. 8S, p. 08JC10, Aug. 2013.

[15] M. T. Hardy, P. S. Hsu, F. Wu, I. L. Koslow, E. C. Young, S. Nakamura, A. E. Romanov, S. P. DenBaars, and J. S. Speck, "Trace analysis of non-basal plane misfit stress relaxation in (20-21) and (30-3-1) semipolar InGaN/GaN heterostructures," *Appl. Phys. Lett.*, vol. 100, no. 20, p. 202103, 2012.

[16] E. C. Young, C. S. Gallinat, A. E. Romanov, A. Tyagi, F. Wu, and J. S. Speck, "Critical Thickness for Onset of Plastic Relaxation in (11-22) and (20-21) Semipolar AlGaN Heterostructures," *Appl. Phys. Express*, vol. 3, no. 11, p. 111002, Oct. 2010.

[17] E. A. Fitzgerald, G. P. Watson, R. E. Proano, D. G. Ast, P. D. Kirchner, G. D. Pettit, and J. M. Woodall, "Nucleation mechanisms and the elimination of misfit dislocations at mismatched interfaces by reduction in growth area," *J. Appl. Phys.*, vol. 65, no. 6, p. 2220, 1989.

[18] P. S. Hsu, E. C. Young, A. E. Romanov, K. Fujito, S. P. DenBaars, S. Nakamura, and J. S. Speck, "Misfit dislocation formation via pre-existing threading dislocation glide in (11-22) semipolar heteroepitaxy," *Appl. Phys. Lett.*, vol. 99, no. 8, p. 081912, 2011.

[19] M. T. Hardy, F. Wu, P. Shan Hsu, D. a. Haeger, S. Nakamura, J. S. Speck, and S. P. DenBaars, "True green semipolar InGaN-based laser diodes beyond critical thickness limits using limited area epitaxy," *J. Appl. Phys.*, vol. 114, no. 18, p. 183101, 2013.

[20] M. T. Hardy, S. Nakamura, J. S. Speck, and S. P. DenBaars, "Suppression of relaxation in (20-21) InGaN/GaN laser diodes using limited area epitaxy," *Appl. Phys. Lett.*, vol. 101, no. 24, p. 241112, 2012.

[21] B. Van Daele, G. Van Tendeloo, K. Jacobs, I. Moerman, and M. R. Leys, "Formation of metallic in in InGaN/GaN multiquantum wells," *Appl. Phys. Lett.*, vol. 85, no. 19, pp. 4379–4381, 2004.

[22] M. T. Hardy, F. Wu, C.-Y. Huang, Y. Zhao, D. F. Feezell, S. Nakamura, J. S. Speck,

and S. P. DenBaars, “Impact of p-GaN Thermal Damage and Barrier Composition on Semipolar Green Laser Diodes,” *IEEE Photonics Technol. Lett.*, vol. 26, no. 1, pp. 43–46, Jan. 2014.

[23] Y.-H. Cho, J. J. Song, S. Keller, M. S. Minsky, E. Hu, U. K. Mishra, and S. P. DenBaars, “Influence of Si doping on characteristics of InGaN/GaN multiple quantum wells,” *Appl. Phys. Lett.*, vol. 73, no. 8, p. 1128, 1998.

[24] N. G. Young, R. M. Farrell, Y. L. Hu, Y. Terao, M. Iza, S. Keller, S. P. DenBaars, S. Nakamura, and J. S. Speck, “High performance thin quantum barrier InGaN/GaN solar cells on sapphire and bulk (0001) GaN substrates,” *Appl. Phys. Lett.*, vol. 103, no. 17, p. 173903, 2013.

[25] R. M. Farrell, C. J. Neufeld, S. C. Cruz, J. R. Lang, M. Iza, S. Keller, S. Nakamura, S. P. DenBaars, U. K. Mishra, and J. S. Speck, “High quantum efficiency InGaN/GaN multiple quantum well solar cells with spectral response extending out to 520 nm,” *Appl. Phys. Lett.*, vol. 98, no. 20, p. 201107, 2011.

[26] Jinn-Kong Sheu, Chih-Ciao Yang, Shang-Ju Tu, Kuo-Hua Chang, Ming-Lun Lee, Wei-Chih Lai, and Li-Chi Peng, “Demonstration of GaN-Based Solar Cells With GaN/InGaN Superlattice Absorption Layers,” *IEEE Electron Device Lett.*, vol. 30, no. 3, pp. 225–227, Mar. 2009.

[27] F. Jiang, R.-V. Wang, A. Munkholm, S. K. Streiffer, G. B. Stephenson, P. H. Fuoss, K. Latifi, and C. Thompson, “Indium adsorption on GaN under metal-organic chemical vapor deposition conditions,” *Appl. Phys. Lett.*, vol. 89, no. 16, p. 161915, 2006.

[28] S. Pereira, M. R. Correria, E. Pereira, K. P. O’Donnell, C. Trager-Cowan, F. Sweeney, and E. Alves, “Compositional pulling effects in InXGa(1-x)N/GaN layers: A combinated depth-resolved cathodoluminscence and Rutherford backscattering/channeling study,” *Phys. Rev. B*, vol. 64, p. 205311, Mar. 2001.

[29] S. Keller, B. P. Keller, D. Kapolnek, A. C. Abare, H. Masui, L. A. Coldren, U. K. Mishra, and S. P. Den Baars, “Growth and characterization of bulk InGaN films and quantum wells,” *Appl. Phys. Lett.*, vol. 68, no. 22, p. 3147, 1996.

[30] S. Keller, S. F. Chichibu, M. S. Minsky, E. Hu, U. K. Mishra, and S. P. DenBaars, “Effect of the growth rate and the barrier doping on the morphology and the properties of InGaN/GaN quantum wells,” *J. Cryst. Growth*, vol. 195, no. 1–4, pp. 258–264, Dec. 1998.

[31] Y.-L. Hu, R. M. Farrell, C. J. Neufeld, M. Iza, S. C. Cruz, N. Pfaff, D. Simeonov, S. Keller, S. Nakamura, S. P. DenBaars, U. K. Mishra, and J. S. Speck, “Effect of quantum well cap layer thickness on the microstructure and performance of InGaN/GaN solar cells,” *Appl. Phys. Lett.*, vol. 100, no. 16, p. 161101, 2012.

[32] S. M. Ting, J. C. Ramer, D. I. Florescu, V. N. Merai, B. E. Albert, A. Parekh, D. S.

Lee, D. Lu, D. V. Christini, L. Liu, and E. a. Armour, “Morphological evolution of InGaN/GaN quantum-well heterostructures grown by metalorganic chemical vapor deposition,” *J. Appl. Phys.*, vol. 94, no. 3, p. 1461, 2003.

[33] O. Schön, B. Schineller, M. Heuken, and R. Beccard, “Comparison of hydrogen and nitrogen as carrier gas for MOVPE growth of GaN,” *J. Cryst. Growth*, vol. 189–190, pp. 335–339, Jun. 1998.

[34] E. L. Piner, M. K. Behbehani, N. a El-Masry, F. G. McIntosh, J. C. Roberts, K. S. Boutros, and S. M. Bedair, “Effect of hydrogen on the indium incorporation in InGaN epitaxial films,” *Appl. Phys. Lett.*, vol. 70, no. 4, p. 461, 1997.

[35] X. H. Wu, C. R. Elsass, A. Abare, M. Mack, S. Keller, P. M. Petroff, S. P. DenBaars, J. S. Speck, and S. J. Rosner, “Structural origin of V-defects and correlation with localized excitonic centers in InGaN/GaN multiple quantum wells,” *Appl. Phys. Lett.*, vol. 72, no. 6, p. 692, 1998.

[36] Y. Kawaguchi, C. Huang, Y. Wu, Y. Zhao, S. P. DenBaars, and S. Nakamura, “Semipolar (20-21) Single-Quantum-Well Red Light-Emitting Diodes with a Low Forward Voltage,” *Jpn. J. Appl. Phys.*, vol. 52, no. 8S, p. 08JC08, Aug. 2013.

Chapter 4

Semipolar Quantum Well Devices for Polarized White Light Emission

4.1 Measurement Set-up

Devices were measured using a confocal optical microscope. [1] Figure 4.1 shows a schematic of the microscope. No illumination source was used, as the purpose of the measurement was to collect and quantify emission from the light-emitting device. The 20× objective lens was nonpolarizing with a numerical aperture of 0.45, which corresponds to a collection angle of 27° in air or 10° in GaN (using an index of refraction of 2.6 for GaN). Therefore, we assume that collected light is approximately normal to the surface.

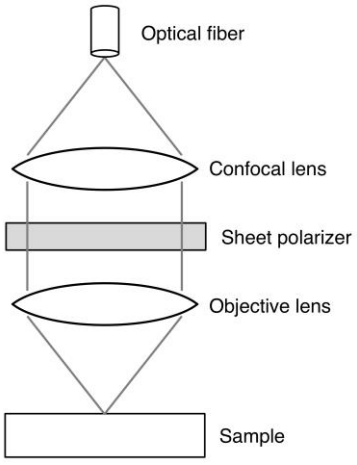

Figure 4.1. Schematic of confocal microscope used for measurements. Polarization measurements required the sheet polarizer, which was removed from the path of the light for measurements not reporting specific polarization data.

Collected light was collimated by the objective lens and passed through the rotational sheet polarizer (or analyzer) if measuring optical polarization. Filter cubes were removed from the path of the light. The collimated beam minimizes the influence of the anisotropy of the analyzer. The analyzer was aligned for polarization measurements by finding the orientation corresponding to maximum and minimum intensities passing through the polarizer. The orientations for maximum and minimum intensity differed by 90°, as expected.

In the confocal set-up, a pinhole was replaced by the optical fiber used to transmit light to a spectrometer. The optical fiber had a 50 μm diameter and a numerical aperture of 0.22 and was manually aligned to the confocal point. Proper alignment of the optical fiber is very important for the following results, and Appendix B provides details of the procedure used to align the optical fiber.

4.2 Double-sided Device

In Ref. [2], we reported the first demonstration of a double-sided device with polarized white light emission, which was achieved by monolithically incorporating electrically injected and optically pumped semipolar InGaN quantum wells (QWs), as described in Section 2.2.1. A blue light-emitting diode (LED) was grown on the $(20\bar{2}\bar{1})$ face of a bulk GaN substrate because previous work has demonstrated that blue LEDs with high power, low droop, and small wavelength shift can be grown on this plane. [3]–[5] The optically pumped InGaN QWs for yellow emission were subsequently grown on the $(20\bar{2}1)$ face. Growing the optically pumped QWs on the opposite side of the double-side-polished (DSP) substrate was advantageous because it allowed for the high indium content InGaN

QWs to be grown after the higher temperature growth of the blue LED, thus limiting the thermal budget to which the high indium content InGaN was subjected, as high temperature may degrade high indium content InGaN. [6], [7] Additionally, growing the QWs for long wavelength emission on the $(20\bar{2}1)$ face was favorable because prior work has demonstrated that this plane is ideal for growing high indium content QWs with long wavelength emission, [8]–[10] while stacking faults have been observed during the growth of high indium content layers on the $(20\bar{2}\bar{1})$ face. [11] Lastly, the $(20\bar{2}1)$ and $(20\bar{2}\bar{1})$ growth planes are appropriate for QWs with optically polarized emission, as discussed in Section 1.3.

The sample was homoepitaxially grown by atmospheric metal organic chemical vapor deposition (MOCVD) on a 7.5 mm × 7.5 mm free-standing, DSP $(20\bar{2}\bar{1})/(20\bar{2}1)$ substrate supplied by Mitsubishi Chemical Corporation. First, an LED was grown on the $(20\bar{2}\bar{1})$ face. The device structure consisted of a 1.5 μm Si-doped *n*-type GaN layer, a ten period InGaN/GaN Si-doped *n*-type superlattice (SL), a 30 nm undoped GaN layer, a 12 nm undoped InGaN single QW active region, a 30 nm undoped GaN layer, a Mg-doped AlGaN electron blocking layer, a 150 nm Mg-doped *p*-type GaN layer, and a Mg-doped p^{++}-type contact layer. Subsequently, high indium content MQWs were grown on the $(20\bar{2}1)$ face. The MQW structure consisted of a 700 nm Si-doped *n*-type GaN layer, a 40 nm undoped low temperature GaN barrier, a three period undoped MQW with 8 nm InGaN QWs and 40 nm GaN barriers, and a 25 nm Si-doped *n*-type GaN cap layer. The growth of the GaN barriers and *n*-type cap layer was performed at the same growth temperature as the growth of the InGaN QWs. A 0.1 mm^2 Pd/Ag/Ni/Au (3/2000/1000/3000 Å) contact was deposited by electron beam evaporation on the Mg-doped p^{++}-type contact layer of the $(20\bar{2}\bar{1})$ LED,

and a soldered indium dot was used as an *n*-contact. Light was collected from the $(20\bar{2}1)$ face.

Figure 4.2(a) shows a schematic of the epitaxial structure reported in this paper. This structure is very similar to the epitaxial structure of a semipolar blue LED grown on a $(20\bar{2}\bar{1})$ GaN substrate, which can be used to create white light by pumping a remote powdered phosphor and is illustrated in Fig. 4.2(b). An *n*-type SL is incorporated in the double-sided device to assist in lateral current conduction to the *n*-contact. [12], [13] Figure 4.3 shows an integrating sphere spectrum of white light emitted by combining the blue LED depicted in Fig. 4.2(b) with a powdered Ce-doped yttrium aluminum garnet (YAG:Ce) phosphor suspended in silicone. This can be compared to the emission from the double-sided device in Fig. 4.2(a), which is presented in Fig. 4.4. Figure 4.4(a) is a micrograph of the device fabricated using the epitaxial structure in Fig. 4.2(a) under electrical injection, and Fig. 4.4(b) shows the electroluminescence (EL) spectra normalized to the peak blue emission for light collected at different points, which are indicated in Fig. 4.4(a). Light extracted from the top-side was measured using a 0.45 numerical aperture 20× microscope objective. The experimental setup is detailed in Section 4.1. For the data presented in Fig. 4.4, no polarizer was in the optical path, and devices were operated under DC bias at room temperature. All spectra were obtained at 20 A/cm^2.

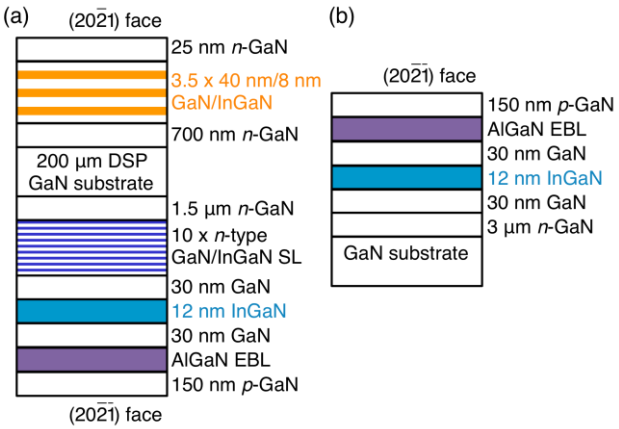

Figure 4.2. Cross-sectional schematics of the epitaxial structure of (a) a double-sided, electrically injected and optically pumped semipolar device and (b) a standard electrically injected semipolar blue LED.

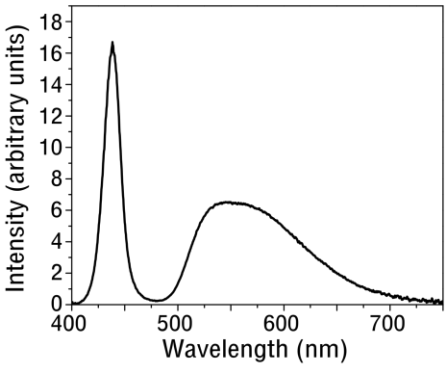

Figure 4.3. White light spectrum emitted by combining the blue LED depicted in Fig. 4.1(b) with a powdered YAG:Ce phosphor .

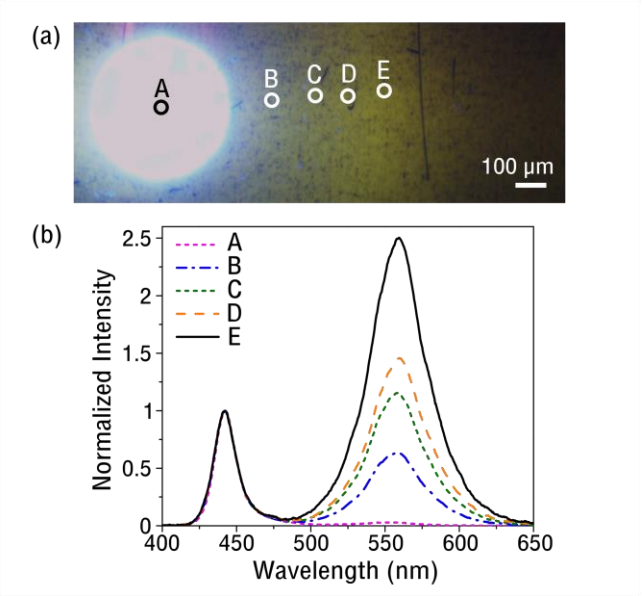

Figure 4.4. (a) Optical micrograph of an electrically injected device based on the epitaxial structure in Fig. 4.2(a) indicating measurement locations. (b) EL spectra at different locations normalized to the corresponding peak blue emission.

As can be seen in Fig. 4.4(b), the electrically injected LED produces a relatively narrow blue emission peak with a maximum intensity at 440 nm, while the optically pumped QWs produce a much broader peak with a maximum intensity at 560 nm. Overall, this is similar to the emission spectrum of the blue LED and yellow phosphor shown in Fig. 4.3. Though the phosphor emission peak is wider than that of the optically pumped QWs, future devices could incorporate additional optically pumped QWs with longer emission wavelengths to achieve a spectrum more comparable to the one produced by the phosphor.

Figure 4.4 also illustrates that the emission color of this sample is not uniform. When the microscope objective is centered directly above the *p*-contact, which is referred to as point A, the blue LED emission is dominant and the intensity is high. Blue light from the LED that has not been extracted or absorbed excites the optically pumped QWs away from the electrically injected area. The ratio of the intensity of the yellow peak to the blue peak increases moving to points B, C, D, and E, for which the microscope objective was centered

above the points indicated in Fig. 4.4(a) corresponding to 360 μm, 500 μm, 600 μm, and 725 μm away from the center of the *p*-contact, respectively. Figure 4.5 is a 1931 *Commission Internationale de l'Eclairage* (CIE) *x, y* chromaticity diagram, which indicates the locations of the spectra for Points A, B, C, D, and E. The CIE *x*- and *y*-chromaticity coordinates are (0.16, 0.03), (0.24, 0.21), (0.28, 0.29), (0.30, 0.33), and (0.33, 0.39) for points A, B, C, D, and E, respectively. Point C lies very close to the Planckian locus and corresponds to white light emission with a correlated color temperature (CCT) of 9859 K. (See Section 1.2 for the background on characterizing color.)

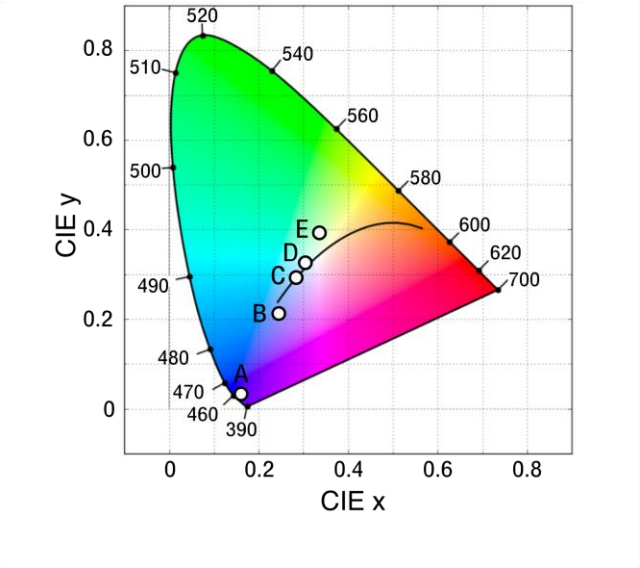

Figure 4.5. CIE *x, y* chromaticity diagram indicating the color at measurement locations indicated in Fig. 4.4(a).

In this case, color tuning was a result of non-uniform emission across the sample. This result illustrates the potential to achieve white light emission from this device design by combining emission from a $(20\bar{2}\bar{1})$ blue LED and yellow emission from $(20\bar{2}1)$ optically pumped QWs. Ongoing work is focused on increasing the intensity of the long wavelength emission from the optically pumped QWs relative to the blue emission from the LED in order to achieve uniform white light emission. The color uniformity can be improved by

increasing the yellow emission from the optically pumped QWs and/or reducing the amount of blue light that is extracted.

One way to increase yellow emission is to increase the radiative efficiency of the optically pumped QWs. The radiative efficiency of the optically pumped QWs can be increased by optimizing the growth conditions of the QWs. The growth of high indium content InGaN for long wavelength emission requires low growth temperatures to prevent desorption of indium from the surface. However, low growth temperatures can result in increased point defects and growth errors. Growth temperature, growth rate, and the ratio of the indium to gallium precursors can be optimized to realize improvements in the crystal quality of the high indium content InGaN QWs. The radiative efficiency of the optically pumped QWs can also be increased by growing thinner QWs, which would increase the overlap of the electron and hole wave functions.

This initial device could also be improved by increasing the absorption of blue light by the optically pumped QWs to convert more blue light to long wavelength emission. This would serve both to increase the yellow emission and decrease the amount of blue light that is extracted. Increasing the absorption of the optically pumped QWs can be achieved by growing more optically pumped QWs, by growing thinner QWs to increase the overlap of the electron and hole wave functions, and/or by incorporating a dichroic mirror to reflect blue light for additional passes, thus increasing the probability of absorption by the optically pumped QWs.

Besides demonstrating white light emission, this device also exhibits polarized white light emission from the electrically injected and optically pumped semipolar QWs. Figure 4.6 shows EL emission spectra with the polarizer aligned along $[1\bar{2}10]$ (x'-direction) and

with the polarizer aligned along $[10\bar{1}\bar{4}]$ (y'-direction) for light collected at point C. The optical polarization ratio, calculated using integrated intensities as defined in Section 1.3, is 0.40. As can be seen in Fig. 4.6, the blue emission from the $(20\bar{2}\bar{1})$ QW is more polarized than the yellow emission from the $(20\bar{2}1)$ QWs. Based on the measurements at point C, the blue emission resulting from the $(20\bar{2}\bar{1})$ LED has an optical polarization ratio of 0.60, and the yellow emission resulting from the $(20\bar{2}1)$ optically pumped layers has an optical polarization ratio of 0.33. Although the reason for this behavior is unknown, previous experimental results demonstrate significant differences in growth and performance of devices on $(20\bar{2}1)$ and $(20\bar{2}\bar{1})$, including significantly higher optical polarization ratios for $(20\bar{2}\bar{1})$ QWs compared to $(20\bar{2}1)$ QWs. [5], [14]–[17] These references also show that the optical polarization ratio increases with increasing InGaN indium content on $(20\bar{2}\bar{1})$, while the optical polarization ratio remains relatively constant on $(20\bar{2}1)$ as a function of InGaN indium content. Interestingly, the same trends were not observed for $(30\bar{3}\bar{1})$ and $(30\bar{3}1)$ QWs. [18]

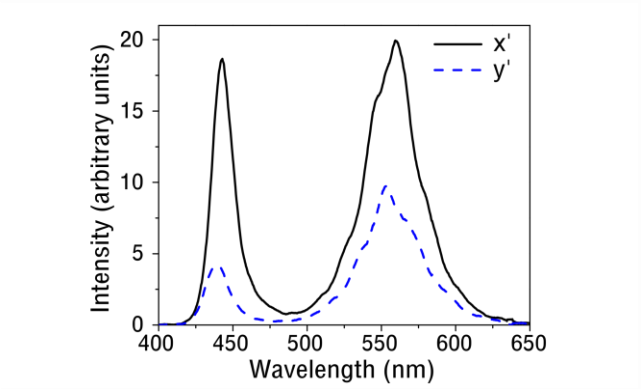

Figure 4.6. EL spectra with polarizer aligned along x'- and y'-directions for light collected at point C as indicated in Fig. 4.4(a).

Figure 4.7 summarizes optical polarization ratios as a function of the peak wavelengths of the dominant component. The blue and red points correspond to values

reported in the literature for electrically injected $(20\bar{2}1)$ and $(20\bar{2}\bar{1})$ InGaN QWs, respectively. [14], [15], [17] The yellow diamond points in Fig. 4.7 indicate the polarization ratios of the optically pumped $(20\bar{2}1)$ yellow QWs and electrically injected $(20\bar{2}\bar{1})$ blue QW, as determined from the measured data in Fig. 4.6. Fig. 4.7 shows that the polarization ratios of the blue and yellow peaks in Fig. 4.6 agree well with other experimental literature values. As an additional reference, Fig. 4.8 shows literature reported optical polarization ratios as a function of the peak wavelengths of the dominant component for (a) *m*-plane and (b) $(30\bar{3}1)$ and $(30\bar{3}\bar{1})$ in red and blue, respectively. [1], [18]–[20]

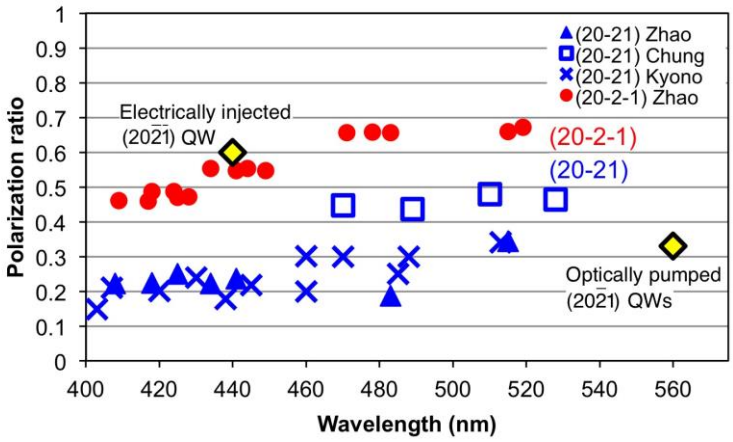

Figure 4.7 Optical polarization ratios as a function of the peak wavelengths of the dominant component for electrically injected InGaN QWs on $(20\bar{2}1)$ and $(20\bar{2}\bar{1})$ in blue and red, respectively. Yellow diamond points indicate the polarization ratios of the optically pumped $(20\bar{2}1)$ yellow QWs and electrically injected $(20\bar{2}\bar{1})$ blue QW from the measured data in Fig. 4.6.

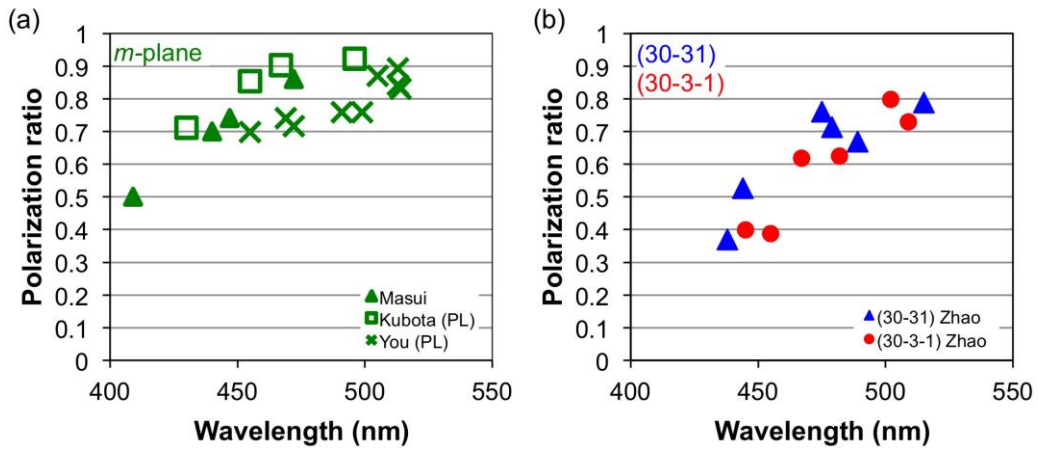

Figure 4.8. Literature reported optical polarization ratios as a function of the peak wavelengths of the dominant component for (a) *m*-plane and (b) in $(30\bar{3}1)$ and $(30\bar{3}\bar{1})$ blue and red, respectively.

According to theory, the strain profiles are identical for $(20\bar{2}1)$ and $(20\bar{2}\bar{1})$, [21] and the predicted separation between the top two valance bands (VBs) is identical for similar InGaN layers on these planes. [15] Therefore, comparable QWs on $(20\bar{2}1)$ and $(20\bar{2}\bar{1})$ should have the same optical polarization ratio. For coherent InGaN layers, a higher indium content increases the strain and should result in a greater VB separation and a higher optical polarization ratio for a QW with yellow emission as compared to a QW with less indium content for blue emission. In this case, a higher optical polarization ratio was observed for $(20\bar{2}\bar{1})$ blue emission compared to $(20\bar{2}1)$ yellow emission, which contradicts theoretical predictions. Zhao *et al*. proposed that the difference in optical polarization ratios on $(20\bar{2}1)$ versus $(20\bar{2}\bar{1})$ might be due to a difference in the indium compositional profile on these planes, [15] but subsequent atom probe tomography results did not a find significant difference between InGaN QWs on $(20\bar{2}1)$ versus $(20\bar{2}\bar{1})$. [22] At this time, understanding the reason for the plane dependence of the optical polarization ratio remains an area for future investigation.

Improving the extraction efficiency of this device while preserving the optical polarization ratio is also an area for future work. The extraction efficiency of LEDs typically is increased by surface roughening, but scattering results in a loss of optical polarization. In this case, one way to increase the extraction efficiency is to incorporate photonic crystals, which have been experimentally demonstrated on *m*-plane to increase extraction efficiency while maintaining optical polarization. [23]

In summary, we have grown and fabricated a novel device design and demonstrated polarized white light emission. By monolithically integrating a blue LED grown on the $(20\bar{2}\bar{1})$ face of a bulk GaN substrate with optically pumped high indium content InGaN QWs for yellow emission subsequently grown on the $(20\bar{2}1)$ face, emission peaks were observed at 440 nm and 560 nm. Emission with CIE *x*- and *y*-chromaticity coordinates of (0.28, 0.29) was reported with an optical polarization ratio of 0.40. This initial demonstration illustrates the potential of monolithic electrically injected and optically pumped devices for polarized white light emission, which has important applications in, for example, LED backlighting for LCDs.

4.3 Double-sided Device with Band Engineering

We report a double-sided device with polarized white light emission that was achieved by monolithically incorporating electrically injected and optically pumped semipolar InGaN QWs. The doping profile in this device was intentionally engineered to red-shift the emission of one of the optically pumped QWs by creating a built-in electric field in the QW that acts in the same direction as the polarization-induced electric field, as described in Section 2.2.2. A blue LED was first grown on the $(20\bar{2}\bar{1})$ face of a DSP bulk

GaN substrate because previous work has demonstrated that blue LEDs with high power, low electrical droop, and small wavelength shift can be grown on this plane. [3]–[5] High indium content InGaN QWs intended for optical pumping and long wavelength emission were subsequently grown on the $(20\bar{2}1)$ face. Growing the optically pumped QWs on the opposite side of the DSP substrate was advantageous because it allowed for the high indium content InGaN QWs to be grown after the higher temperature growth of the blue LED, thus limiting the thermal budget to which the high indium content InGaN was subjected, as high temperature may degrade high indium content InGaN. [6], [7]. Additionally, while $(20\bar{2}\bar{1})$ is a favorable growth plane for blue LEDs, stacking faults have been observed during the growth of high indium content layers on $(20\bar{2}\bar{1})$. [11] However, prior work has demonstrated that $(20\bar{2}1)$ is an ideal plane for growing high indium content QWs with long wavelength emission. [8]–[10] In addition, the $(20\bar{2}1)$ plane and other similar planes can be used to grow a structure in which the doping profile can be engineered to red-shift the emission from optically pumped QWs. [5], [24]–[26] To create a built-in electric field in the same direction as the polarization-induced electric field in an InGaN QW grown by MOCVD, the total polarization discontinuity in the growth direction must be antiparallel to that of *c*-plane (i.e. negative) because MOCVD *p*-type GaN must be grown after the QW to enable activation of the acceptors by removing the hydrogen from the Mg–H complex. The $(20\bar{2}1)$ plane is an appropriate orientation to achieve this because the total polarization discontinuity in $(20\bar{2}1)$ QWs is antiparallel to that of *c*-plane QWs. [5], [24] Lastly, the $(20\bar{2}1)$ and $(20\bar{2}\bar{1})$ growth planes are appropriate for QWs with optically polarized emission, as discussed in Section 1.3.

Samples were homoepitaxially grown by atmospheric pressure MOCVD on a 7.5 mm × 7.5 mm free-standing, DSP $(20\bar{2}\bar{1})/(20\bar{2}1)$ substrate supplied by Mitsubishi Chemical Corporation. First, an LED was grown on the $(20\bar{2}\bar{1})$ face. The device structure consisted of a 3 μm Si-doped *n*-type GaN layer, a 30 nm unintentionally doped (UID) GaN layer, a 12 nm UID InGaN single QW active region, a 30 nm UID GaN layer, a Mg-doped AlGaN electron blocking layer (EBL), a 150 nm Mg-doped *p*-type GaN layer, and a Mg-doped p^{++}-type contact layer. Subsequently, high indium content InGaN QWs were grown on the $(20\bar{2}1)$ face. The structure consisted of a 450 nm Si-doped *n*-type GaN layer, a 60 nm *n*-type GaN layer with [Si] = 7.5×10^{18} cm^{-3}, a 35 nm UID GaN barrier, a 6 nm UID InGaN QW, a 35 nm UID GaN barrier, a 110 nm *n*-type GaN layer with [Si] = 7.5×10^{18} cm^{-3}, a 35 nm UID GaN barrier, a 6 nm UID InGaN QW, a 35 nm UID GaN barrier, and a 60 nm *p*-type GaN layer with [Mg] = 1.0×10^{19} cm^{-3}. The QW situated in a *p*-*i*-*n* structure on $(20\bar{2}1)$ was grown at a growth temperature 10 °C colder than the QW situated in an *n*-*i*-*n* structure. A 0.1 mm^2 Pd/Ag/Ni/Au (3/2000/2000/3000 Å) circular contact was deposited by electron beam evaporation on the Mg-doped p^{++}-type contact layer of the $(20\bar{2}\bar{1})$ LED to form the *p*-contact. The *n*-contact was formed by scribing the $(20\bar{2}\bar{1})$ face and soldering indium to the exposed *n*-type layer of the LED. A schematic of the device structure is shown in Fig. 4.9.

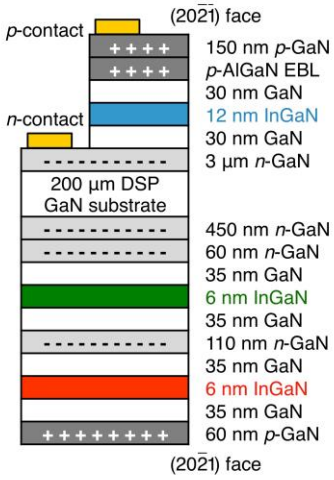

Figure 4.9 Cross-sectional schematic of the epitaxial structure of a double-sided, electrically injected, and optically pumped phosphor-free polarized white light-emitting semipolar device. The (20$\bar{2}$1) *n*-type (*p*-type) layers adjacent to UID barriers were doped with [Si] = 7.5 x 10^{18} cm^{-3} ([Mg] = 1.0 x 10^{19} cm^{-3}).

Figure 4.10 shows simulated energy band diagrams for the optically pumped (20$\bar{2}$1) QWs at a 0 V bias. The simulation was performed with commercial package SiLENSe version 5.8. [27] In Fig. 4.10(a), the QW in the *n*-*i*-*n* structure consisted of 6 nm of $In_{0.27}Ga_{0.73}N$, and the QW in the *p*-*i*-*n* structure consisted of 6 nm of $In_{0.29}Ga_{0.71}N$. The change in the InGaN indium content for the different QWs corresponds to the different growth temperatures used in growing the optically pumped QWs in the experimental sample. For all of the modeling work, the QWs were assumed to consist of 6 nm of InGaN, the *n*-type GaN layers were doped with [Si] = 7.5 × 10^{18} cm^{-3}, the *p*-type GaN layer was doped with [Mg] = 1.0 × 10^{19} cm^{-3}, and the UID GaN layers were assumed to have 1.0 x 10^{17} cm^{-3} donors. Table 4.1 summarizes the material properties used in the modeling. [28], [29] As can be seen in Fig. 4.10(a), the *p*-*i*-*n* built-in electric field acts in the same direction as the polarization-induced electric field in (20$\bar{2}$1) InGaN QWs, resulting in an increased electric field in the QW situated in a *p*-*i*-*n* structure compared to the QW in an *n*-*i*-*n* structure. This increased electric field is expected to red-shift the emission wavelength.

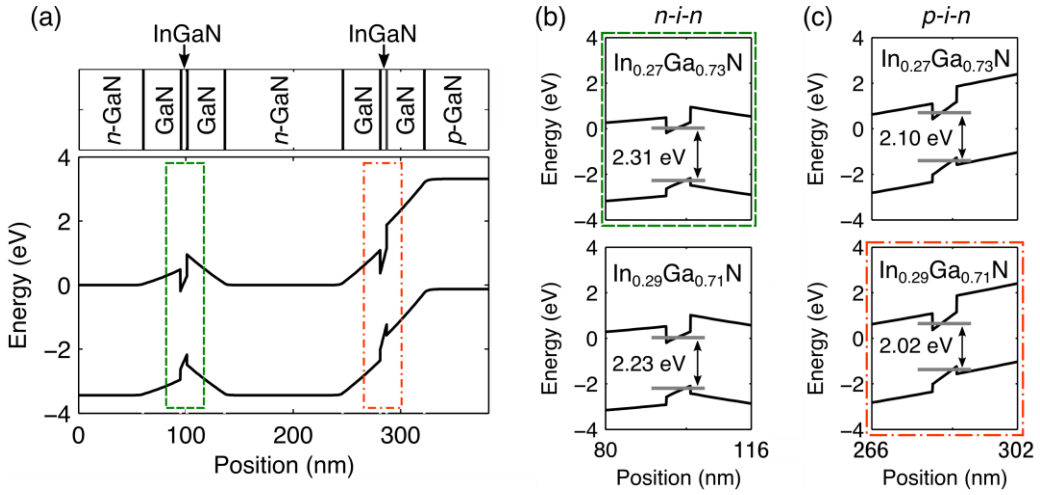

Figure 4.10. (a) Simulated band structure under 0 V bias showing $(20\bar{2}1)$ optically pumped QWs as indicated in Fig. 4.9. The QW in the *n-i-n* and *p-i-n* structures were $In_{0.27}Ga_{0.73}N$ and $In_{0.29}Ga_{0.71}N$, respectively. Simulated band diagrams of $In_{0.27}Ga_{0.73}N$ and $In_{0.29}Ga_{0.71}N$ QWs in (b) *n-i-n* and (c) *p-i-n* structures. The electron—heavy hole ground state transition energy is indicated.

TABLE 4.1. III-nitride materials properties for simulations. Data for effective masses are taken from Ref. [28]. Data for splitting parameters are taken from Ref. [29].

Material property	*InN*	*GaN*
Electron effective mass (m_0)	0.1	0.2
Heavy hole effective mass (m_0)	1.63	1.4
Light hole effective mass (m_0)	0.27	0.3
Split-off hole effective mass (m_0)	0.65	0.6
Crystal-field splitting (meV)	1	14
Spin-orbit splitting (meV)	41	19

Both the increased InGaN indium content and increased total electric field in the QW contributed to red-shifting the emission from the QW in the *p-i-n* structure as compared to the QW in the *n-i-n* structure. However, as both our experimental work and simulation results support, the change in the built-in electric field in these structures was more significant in red-shifting emission wavelength than the change in the alloy content. Figures 4.10(b) and 4.10(c) consider $In_{0.27}Ga_{0.73}N$ and $In_{0.29}Ga_{0.71}N$ QWs in either the *n-i-n* or *p-i-n* structures, respectively. The electron−heavy hole transitions are indicated on these band diagrams, and Table 4.2 shows the calculated energies for the electron−heavy hole, electron−light hole, and electron−split-off hole ground state transitions for the $In_{0.27}Ga_{0.73}N$

and $In_{0.29}Ga_{0.71}N$ QWs in either the *n-i-n* or *p-i-n* structures. These simulation results indicate that changing the QW composition from $In_{0.27}Ga_{0.73}N$ to $In_{0.29}Ga_{0.71}N$ results in a red-shift of the emission produced by the electron−heavy hole ground state transition of 19 nm (79 meV) or 24 nm (81 meV) for the 6 nm InGaN QW situated in an *n-i-n* or *p-i-n* structure, respectively. However, situating the 6 nm $In_{0.27}Ga_{0.73}N$ QW or 6 nm $In_{0.29}Ga_{0.71}N$ QW in the *p-i-n* structure instead of the *n-i-n* structure results in a 52 nm (204 meV) or 57 nm (206 meV) red-shift in the emission produced by the electron−heavy hole ground state transition, respectively. Thus, in the structure shown in Fig. 4.9, situating the $In_{0.29}Ga_{0.71}N$ QW in the *p-i-n* structure red-shifted the emission more than changing the InGaN alloy composition from $In_{0.27}Ga_{0.73}N$ to $In_{0.29}Ga_{0.71}N$.

TABLE 4.2. Calculated ground state transitions in eV (nm).

	QW in n-i-n structure		*QW in p-i-n structure*	
Transition	$In_{0.27}Ga_{0.73}N$	$In_{0.29}Ga_{0.71}N$	$In_{0.27}Ga_{0.73}N$	$In_{0.29}Ga_{0.71}N$
Electron—heavy hole	2.306 (538)	2.227 (557)	2.102 (590)	2.021 (614)
Electron—light hole	2.369 (523)	2.293 (541)	2.178 (569)	2.100 (590)
Electron—split-off hole	2.361 (525)	2.284 (543)	2.165 (573)	2.086 (594)

Figure 4.11(a) shows the normalized white light EL spectrum of the device from Fig. 4.9. Light emitted from the $(20\bar{2}\bar{1})$ face was collected using a 0.45 numerical aperture 20× microscope objective. The experimental setup is detailed in Section 4.1. For the data presented in Fig. 4.11(a), there was no polarizer in the optical path, and the device was operated at 10 A/cm^2 under DC bias at room temperature. Similar to the device reported in Section 4.2 and Ref. [2], the emission color was spatially non-uniform, making it possible to tune the color by changing the measurement location. To obtain white light emission shown in Fig. 4.9(a), the measurements were made 680 μm away from the center of the circular *p*-contact. Moving away from the center of the electrically injected device increased the

relative intensity of long wavelength emission from the optically pumped QWs compared to blue emission from the electrically injected QW because blue light that has not been extracted or absorbed can excite the optically pumped QWs away from the electrically injected area.

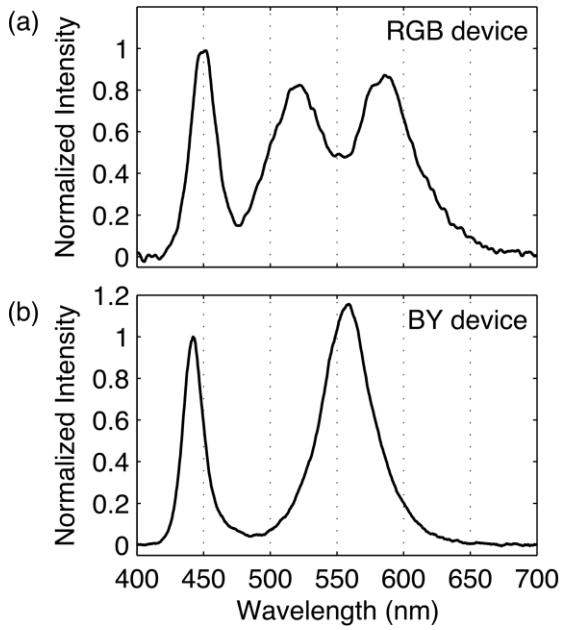

Figure 4.11. (a) EL spectrum for the device in Fig. 4.9 with a peak at 450 nm from the electrically injected LED and peaks at 520 nm and 590 nm from optically pumped QWs in *n*-*i*-*n* and *p*-*i*-*n* structures, respectively. (b) EL spectrum from the white light-emitting device reported in Section 4.2 with a peak at 440 nm from an electrically injected LED and a peak at 560 nm from optically pumped QWs.

In Fig. 4.11(a), the relatively narrow peak at 450 nm is emission from the electrically injected $(20\bar{2}\bar{1})$ LED. The peak at 520 nm is emission from the optically pumped $(20\bar{2}1)$ QW with slightly lower InGaN indium content in an *n*-*i*-*n* structure, and the peak at 590 nm is emission from the optically pumped $(20\bar{2}1)$ QW with slightly higher InGaN indium content in a *p*-*i*-*n* structure, corresponding to a 70 nm shift in wavelength relative to the QW in an *n*-*i*-*n* structure. As shown in Fig. 4.10 and Table 4.2, this red-shifted emission from the QW in the *p*-*i*-*n* structure compared to the QW in the *n*-*i*-*n* structure was due to increased indium content InGaN as well as the effect of the built-in electric field. The electron−heavy

hole ground state transitions indicated in Fig. 4.10 and Table 4.2 are of slightly lower energy than the emission peaks because the emission peaks are also composed of higher energy transitions. The simulation results agree well with the experimentally observed 70 nm red-shift in the emission wavelength from the higher indium content InGaN QW in the *p-i-n* structure compared the lower indium content InGaN QW in the *n-i-n* structure, with a 19 nm red-shift attributed to the increase in the indium content of the InGaN QW and a 57 nm red-shift attributed to the band engineering.

In Section 4.2 and Ref. [2], we demonstrated a similar white light-emitting device by combining emission from monolithic electrically injected and optically pumped QWs. The device combined blue emission from an electrically injected $(20\bar{2}\bar{1})$ QW and yellow emission from three optically pumped $(20\bar{2}1)$ QWs in an *n-i-n* structure. The EL spectrum from this device is shown again in Fig. 4.11(b) and can be compared to the emission spectrum in Fig. 4.11(a). To facilitate the comparison of the emission spectra from the optically pumped QWs in the two cases, each spectrum was normalized to the corresponding maximum of the blue emission peak. The device measured in Fig. 4.11(a) will be referred to as the red/green/blue (RGB) device, and the device measured in Fig. 4.11(b) will be referred to as the blue/yellow (BY) device.

The spectrum depicted in Fig. 4.11(a) from the RGB device has several advantages over the spectrum in Fig. 4.11(b) from the BY device for both general illumination and display technology. By producing light that is more widely distributed across the visible spectrum, the RGB device is able to render colors more faithfully than the BY device, which is important for general illumination. The RGB device would also be more energy efficient than the BY device for backlighting displays. Creating red, green, and blue emission peaks

would align the white light spectrum with the transmission spectra of display filters that are typically designed to transmit red, green, and blue light, resulting in less light being lost to absorption in the filters.

Figure 4.12 is a 1931 CIE *x*, *y* chromaticity diagram, which indicates the location of the spectrum shown in Fig. 4.11(a). The CIE *x*- and *y*-chromaticity coordinates are (0.33, 0.35). This point lies close to the Planckian locus and corresponds to white light emission with a CCT of 5604 K and a color rendering index (CRI) of 70. (See Section 1.2 for the background on characterizing color.) Table 4.3 shows a breakdown of the CRI test color samples coloring rendering indices. The color rendering of this emission spectrum would be greatly improved by longer wavelength red emission.

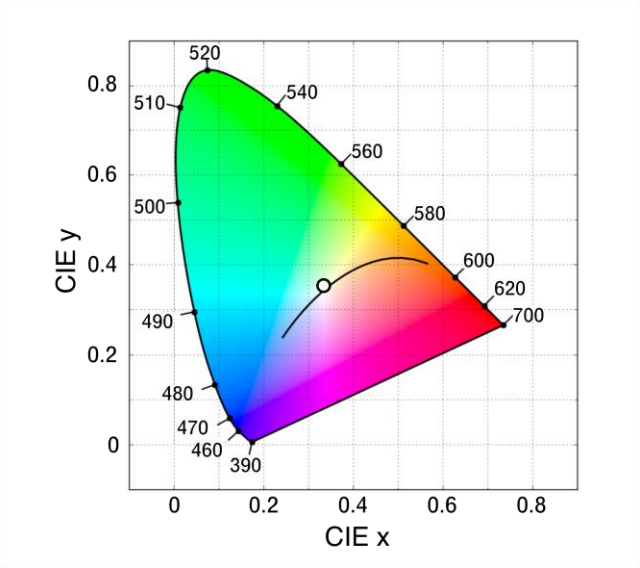

Figure 4.12. CIE *x*, *y* chromaticity diagram indicating the chromaticity coordinates corresponding to the spectrum in Fig. 4.11(a). The *x*- and *y*-chromaticity coordinates are (0.33, 0.35), the CCT is 5604 K, and the CRI is 70.

TABLE 4.3. CRI test color sample rendering indices for device in Fig. 4.7.

CRI test color sample	*Appearance under daylight*	*Rendering index*
TCS01	Light greyish red	60
TCS02	Dark greyish yellow	77
TCS03	Strong yellow green	94
TCS04	Moderate yellowish green	74
TCS05	Light bluish green	70
TCS06	Light blue	80
TCS07	Light violet	73
TCS08	Light reddish purple	28
TCS09	Strong red	-120
TCS10	Strong yellow	58
TCS11	Strong green	78
TCS12	Strong blue	55
TCS13	Light yellowish pink	64
TCS14	Moderate olive green	95

In addition to demonstrating white light emission, this device also exhibited polarized white light emission from the electrically injected and optically pumped semipolar QWs. Figure 4.13 shows EL emission spectra with the polarizer aligned along $[1\bar{2}10]$ (x'-direction) and with the polarizer aligned along $[10\bar{1}\bar{4}]$ (y′-direction). The optical polarization ratio, calculated using integrated intensities as defined in Section 1.3, is 0.30. Previous experimental results have demonstrated significant differences in growth and performance of devices on $(20\bar{2}1)$ and $(20\bar{2}\bar{1})$, including significantly higher optical polarization ratios for $(20\bar{2}\bar{1})$ QWs compared to $(20\bar{2}1)$ QWs. [5], [14]–[17] For the spectra shown in Fig. 4.13, the optical polarization ratio of the $(20\bar{2}\bar{1})$ QW emission is similar to the optical polarization of the $(20\bar{2}1)$ QWs. However, measurements at different locations revealed that the optical polarization ratio of the blue emission decreased as the measurement location was moved farther from the center of the *p*-contact. These results indicate that the blue emission was composed of an increasing proportion of scattered light

with increasing distance from the electrically injected area. This occurred because the intensity of the blue light that had maintained optically polarization and had an angle of incidence within the escape cone decreased with increasing distance from the *p*-contact and an increasing number of reflections.

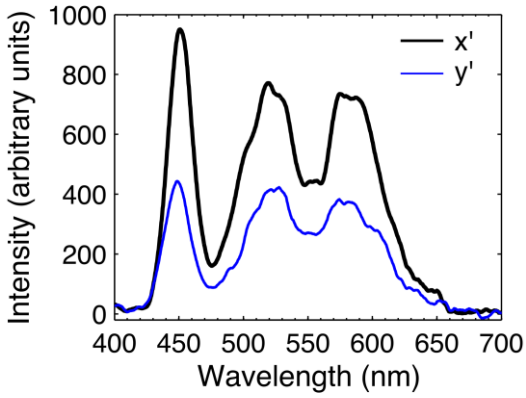

Figure 4.13. EL spectra with the polarizer aligned along $[1\bar{2}10]$ (x'-direction) and with the polarizer aligned along $[\bar{1}01\bar{4}]$ (y′-direction).

There are several additional considerations about why the polarization of the blue light from this device has a lower polarization ratio than expected. First, this device was measured with $(20\bar{2}\bar{1})$ facing up, while the previous device discussed in Section 4.2 and Ref. [2] was measured with $(20\bar{2}1)$ facing up. From additional measurements, we have confirmed that measuring a sample with $(20\bar{2}\bar{1})$ facing up instead of $(20\bar{2}1)$ facing up produces a significant decrease in the polarization ratio of the blue light emitted by the electrically injected QW. In order to measure white light from the $(20\bar{2}1)$ face of the sample reported in Figs. 4.9−4.13, we deposited a 0.1 mm^2 circular 200 nm Al mirror on the $(20\bar{2}1)$ face aligned to the *p*-contact on the $(20\bar{2}\bar{1})$ face. This served to reflect blue light that would have been extracted directly above the *p*-contact. Figure 4.14 shows measurements made with $(20\bar{2}1)$ facing up. The measurements in Fig. 4.14 were made at a point 1000 μm away from the center of the electrically injected LED, but a different device on this sample was

measured than was measured for Figs. 4.11(a) and 4.13, so the white light emission spectrum was different due to a shift in the emission wavelengths. Figure 4.14(a) shows the EL emission spectrum, Fig. 4.14(b) shows the corresponding CIE diagram, and Fig. 4.14(c) shows EL emission spectra with the polarizer aligned along $[1\bar{2}10]$ (x'-direction) and with the polarizer aligned along $[10\bar{1}\bar{4}]$ (y′-direction). The optical polarization ratio, calculated using integrated intensities as defined in Section 1.3, is 0.40. The polarization ratio of the blue peak is 0.58, and the polarization ratio of the longer wavelength emission peaks is 0.29. These values agree well with the results reported in Section 4.2 and Ref. [2]. These additional measurements show that this device emits optically polarized light with polarization ratios comparable to those reported in the literature. However, for our device, the polarization ratio is affected by the measurement location and orientation. This is an area of ongoing investigation.

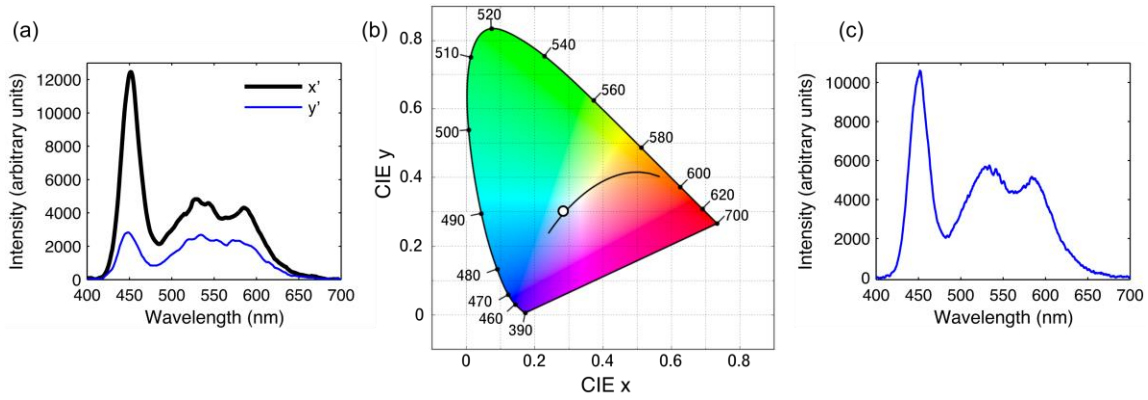

Figure 4.14. (a) EL spectrum for the device in Fig. 4.9 measured with $(20\bar{2}1)$ facing up. (b) CIE *x*, *y* chromaticity diagram indicating the chromaticity coordinates corresponding to the spectrum in (a). The *x*- and *y*-chromaticity coordinates are (0.28, 0.28). (c) EL spectra with the polarizer aligned along $[1\bar{2}10]$ (x'-direction) and with the polarizer aligned along $[\bar{1}01\bar{4}]$ (y′-direction).

We also suspect that surface roughness contributed to a decreased polarization ratio of the blue light that was reported in Fig. 4.13. Figure 4.15 is an optical micrograph showing the measurement location for the emission spectra in Figs. 4.11(a) and 4.13. This optical

micrograph shows the sample under illumination by a fluorescence filter cube. As can be seen in Fig. 4.15, approximately 200 μm away was surface roughness visible that was with the optical microscope, which appears to have been caused by the surface being dirty prior to the growth of the optically pumped QWs.

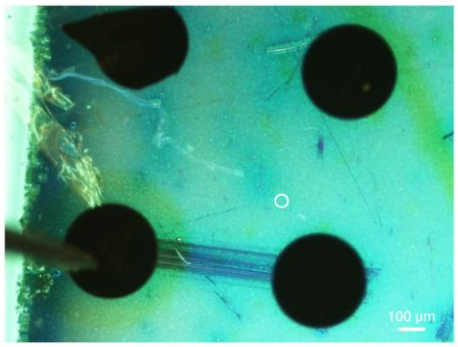

Figure 4.15. Optical micrograph under fluorescence excitation of sample measured in Figs. 4.11(a) and 4.13 shows surface roughness on $(20\bar{2}1)$. The white circle indicates the measurement location. The probe can be seen on the circular contact on the bottom left of this image, which was the electrically injected device.

Lastly, if the blue electrically injected $(20\bar{2}\bar{1})$ QW relaxed, it would produce blue light was a lower polarization ratio than expected from a coherent QW. [30] Although misfit dislocations were not visible by fluorescence microscopy after growth of the blue LED, it is possible that the QW relaxed when brought to high temperature again for the growth of the $(20\bar{2}1)$ optically pumped QWs. It is difficult to see the blue optically pumped QW by fluorescence microscopy after the growth of longer wavelength QWs, which appear very bright in fluorescence microscopy.

Based on the observed dependence of the optical polarization ratio on measurement position, it is expected that efforts to improve color uniformity and extraction efficiency should also improve the optical polarization ratio of the emission. Further improvements in device performance could be achieved by increasing the number of optically pumped QWs to increase the relative intensity of long wavelength emission to blue emission, by

depositing a dichroic mirror with high reflectance of blue light and high transmittance of longer wavelengths to better control the color, and/or by incorporating a photonic crystal to increase extraction efficiency while preserving the optical polarization.

In summary, we have grown and fabricated a polarized white light-emitting device that monolithically integrates a blue LED grown on the $(20\bar{2}\bar{1})$ face of a bulk GaN substrate with optically pumped high indium content InGaN QWs for long wavelength emission grown on the $(20\bar{2}1)$ face. The doping profile was intentionally engineered to red-shift the emission of one of the optically pumped QWs by creating a built-in electric field in the QW that acted in the same direction as the polarization-induced electric field. Emission peaks were observed at 450 nm from the electrically injected QW and at 520 nm and 590 nm from the optically pumped QWs, which were grown in *n*-*i*-*n* and *p*-*i*-*n* structures, respectively. Modeling work supported that band engineering red-shifted the emission from the QW in the *p*-*i*-*n* structure more significantly than the red-shift attributed to the change in InGaN alloy composition produced by the QW in the *p*-*i*-*n* structure being grown 10 °C colder than the QW in the *n*-*i*-*n* structure. Emission with CIE *x*- and *y*-chromaticity coordinates of (0.33, 0.35) and an optical polarization ratio of 0.30 was reported. This monolithic electrically injected and optically pumped device produced polarized white light with an emission spectrum that would be desirable for either general illumination or display technology.

4.4 Tunnel Junction Device

We report a device in which a tunnel junction is used to monolithically integrate an electrically injected blue light-emitting diode (LED) and optically pumped InGaN quantum wells (QWs) with yellow emission. This device employs optically pumped QWs for long

wavelength emission because optically pumping offers several advantages over electrically injecting InGaN QWs for long wavelength emission. This device design employs a tunnel junction, which allows for electrical injection of the blue LED when it is buried below the subsequently grown optically pumped QWs for long wavelength emission. This is advantageous because higher indium content InGaN QWs for long wavelength emission are grown at low temperature and may be damaged by high temperature growth steps, which are required in the growth of a blue LED. [6], [7] In this device design, contact is made to the *n*-side of the LED and the *n*-side of the tunnel junction, allowing for electrical injection of the blue QWs. There is no *p*-type contact, which is beneficial because no metal with an appropriate work function exists for making ohmic contact to *p*-type GaN. [31], [32] And the *n*-type GaN above the tunnel junction is used for current spreading, which is advantageous because GaN has less absorbance than TCOs or metal contacts. [33]

The tunnel junction in this initial device was grown by NH_3 molecular beam epitaxy (MBE), while the light-emitting layers were grown by MOCVD. As discussed in Section 2.2.3, use of MBE enabled the growth of activated buried *p*-type GaN layers and a tunnel junction, while use of MOCVD enabled InGaN with high radiative efficiency. [34]–[36], [33] This device demonstration was grown on $(20\bar{2}1)$ because prior work has demonstrated that $(20\bar{2}1)$ is an ideal plane for growing high indium content InGaN QWs with long wavelength emission, [8]–[10] while stacking faults have been observed during the growth of high indium content layers on $(20\bar{2}\bar{1})$ or *m*-plane. [11], [37] Additionally, $(20\bar{2}1)$ is an appropriate growth plane for QWs with optically polarized emission, as discussed in Section 1.3.

Samples were homoepitaxially grown on a 7.5 mm × 7.5 mm free-standing $(20\bar{2}1)$ bulk GaN substrate supplied by Mitsubishi Chemical Corporation. First, an LED was grown by MOCVD. The device structure consisted of a 1.4 μm Si-doped *n*-type GaN layer, a 6 nm undoped GaN layer, a 3 period 3 nm/4 nm InGaN/GaN nm MQW active region, a 10 nm undoped GaN layer, a 12 nm Mg-doped AlGaN electron blocking layer (EBL), a 145 nm Mg-doped *p*-type GaN layer, and a 13 nm Mg-doped p^{++}-type contact layer. The sample was removed from the MOCVD, exposed to ambient, and the *p*-type GaN was activated by annealing at 600 °C before molecular beam epitaxy (MBE) was used to a 20 nm n^{+}-type layer above the p^{+}-GaN layer to form a tunnel junction. A 100 nm *n*-type GaN capping layer was also grown by MBE. The sample was removed from the MBE and exposed to ambient before MOCVD was used to grow the optically pumped multiple QWs. The structure consisted of a 440 nm Si-doped *n*-type GaN layer, a 35 nm unintentionally doped GaN barrier, a 2.5 period 6 nm/35 nm InGaN/GaN MQW stack, a 35 nm unintentionally doped GaN barrier, and a 23 nm *n*-type GaN. The growth of the optically pumped QWs stack was performed at a constant temperature after the higher temperature growth of the first 200 nm of *n*-type GaN. Devices were fabricated by etching a 1.8 μm deep mesa to define a 0.1 mm^2 circular injection area and expose the *n*-type GaN below the blue LED. The etched area was a ring such that the optically pumped QWs were not etched in the field between the electrically injected devices. A separate 300 nm deep etch exposed the *n*-type GaN above the tunnel junction. The etched area was a circle which had a radius of 32 μm and which was positioned at the center of the 0.1 mm^2 mesa. A Ti/Al/Ni/Au (200/1000/2000/3000 Å) metal stack was deposited by electron-beam evaporation to make contact to the *n*-side of the LED and the *n*-side of the tunnel junction. The contact to the *n*-side of the LED was a ring

surrounding the mesa. The contact to the *n*-side of the tunnel junction was a circle with a radius of 25 μm. The *n*-contact metal stack was annealed at 450 °C in nitrogen. The backside of the device was polished to an optically smooth surface to prevent scattering and preserve the optical polarization of light emitted by strained InGaN QWs. A schematic of the device structure is shown in Fig. 4.16.

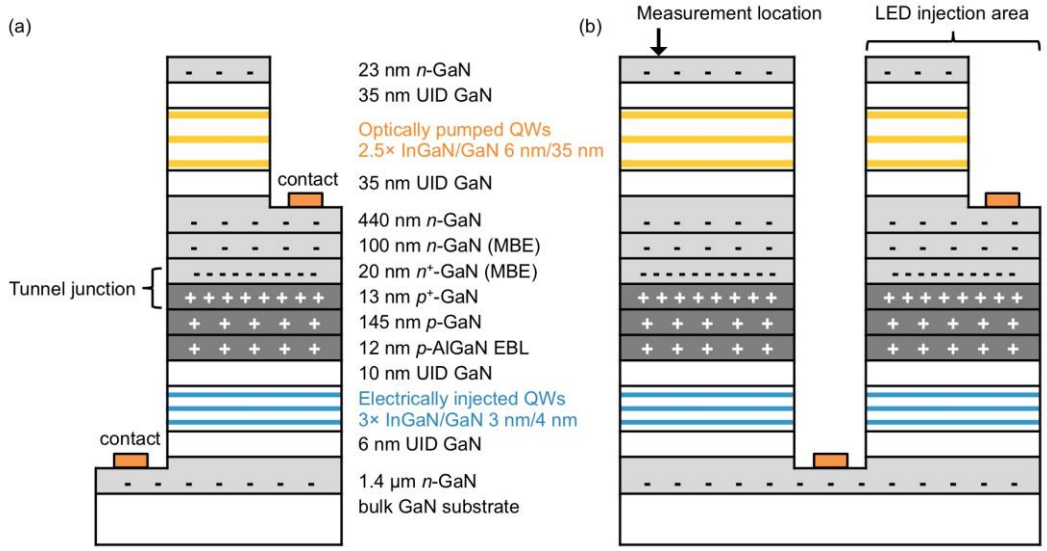

Figure 4.16. Cross-sectional schematic of a device grown on $(20\bar{2}1)$ that used a tunnel junction to incorporate optically pumped QWs above electrically injected QWs. The tunnel junction was grown by MBE. (a) shows a singulated device. (b) shows the device used for our measurements, where the emission spectra were measured away from the electrically injected device.

Figure 4.17 shows the current−voltage characteristics for the device in Fig. 4.16. Devices were operated under DC bias at room temperature. Though measurements of the contacts made to the *n*-side of the LED indicate that the contacts were ohmic, we expect that improved electrical characteristics could be achieved by optimizing the *n*-contacts and tunnel junction. Young *et al.* have published lower turn-on voltages for diodes grown by our hybrid MOCVD/MBE growth technique, though their work did not involve a second MOCVD regrowth. [35]

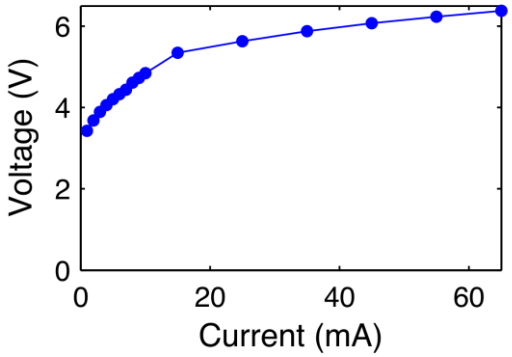

Figure 4.17. Current−voltage characteristics of the device in Fig. 4.16.

Figure 4.18 shows optical micrographs of the tunnel junction device under electrical injection. These images illustrate the injection uniformity of the tunnel junction device and confirm that we achieved current spreading in the *n*-type GaN layer. However, current is not spreading all the way to the edges of the mesa, which defines the injection area and is indicated by the dotted line circles that were added to the micrographs in Fig. 4.18. Figures 4.18(a) and 4.18(b) were taken with a lower power objective lens, while a higher power objective lens was used to take Fig. 4.18(c) at higher magnification. Figure 4.18(a) was taken with a longer exposure time, which allows the probes to be seen, while Figs. 4.18(b) and 14.8(c) were taken with a shorter exposure times to better image the current injection without saturating the camera.

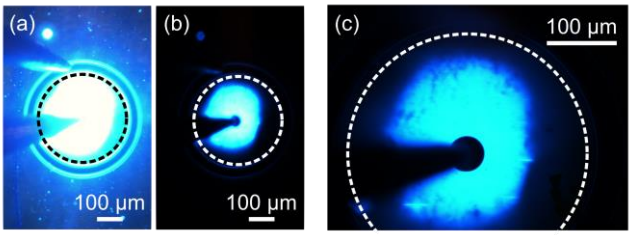

Figure 4.18. Optical micrographs of the device in Fig. 4.16 under electrical injection show current spreading achieved by the tunnel junction. Dashed line circles indicate mesa area. (a) and (b) are images at a lower a magnification, with (a) having a shorter exposure time than (b) and showing probe tips contacting the sample. (c) is an image at higher magnification.

Figure 4.19 shows the EL emission spectrum of the device from Fig. 4.16. The spectral measurements were made with the device operating at 60 A/cm^2. The relatively

narrow peak at 450 nm is emission from the electrically injected LED, and the peak at 560 nm is emission from the optically pumped QWs. Light emitted from the $(20\bar{2}1)$ face was collected using a 0.45 numerical aperture 20× microscope objective. The experimental setup is detailed in Section 4.1. For the data presented in Fig. 4.19, no polarizer was in the optical path. Similar to the device reported in Section 4.2 and Ref. [2], the emission color was spatially non-uniform. Blue light that has not been extracted or absorbed can excite the optically pumped QWs away from the electrically injected area. Thus, moving away from the center of the electrically injected device increased the relative intensity of yellow emission from the optically pumped QWs compared to blue emission. For the data presented in Figs. 4.19 and 4.20, the measurements were made 2.8 mm away from the center of the circular LED.

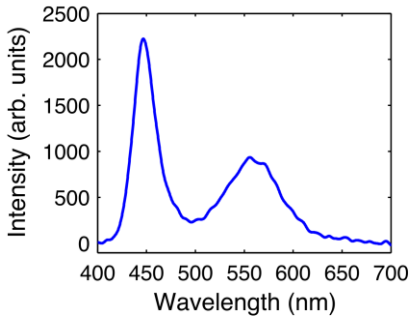

Figure 4.19. EL emission spectrum for the device in Fig. 4.16 with a peak at 450 nm from the electrically injected LED and a peak at 560 nm optically pumped QWs.

Figure 4.18 shows the EL emission spectra with the polarizer aligned along $[1\bar{2}10]$ (x'-direction) and with the polarizer aligned along $[\bar{1}01\bar{4}]$ (y′-direction). The optical polarization ratio, calculated using integrated intensities as defined in Section 1.3, is 0.28. Thus, this initial device demonstrates optically polarized emission from this semipolar optically pumped and electrically injected tunnel junction device design. Figure 4.19 summarizes optical polarization ratios as a function of the peak wavelengths of the dominant

component. The blue and red points correspond to values reported in the literature for electrically injected $(20\bar{2}1)$ and $(20\bar{2}\bar{1})$ InGaN QWs, respectively. [14], [15], [17] As determined from the measured data in Fig. 4.20, the yellow diamond points in Fig. 4.21 indicate the polarization ratios of the optically pumped yellow QWs and electrically injected blue QWs of the $(20\bar{2}1)$ tunnel junction device. Fig. 4.21 shows that the polarization ratios of the blue and yellow peaks in Fig. 4.20 agree well with other experimental literature values. However, because measurements were made very far away from the LED injection area, we suspect that the polarization ratio was decreased due to the contribution of scattered light. We expect the contribution of scattered light to have a larger impact on the blue emission polarization ratio because the blue light is emitted from the injection area, while the optically pumped QWs can be excited away from the injection area by blue light that has not been absorbed or extracted. Although long wavelength light is emitted away from the injection area, the long wavelength emission still decreases with increasing distance from the electrically injected LED. Therefore, the polarization ratio of the long wavelength emission may also be affected by measuring very far away from the LED injection area, though likely to a lesser extent.

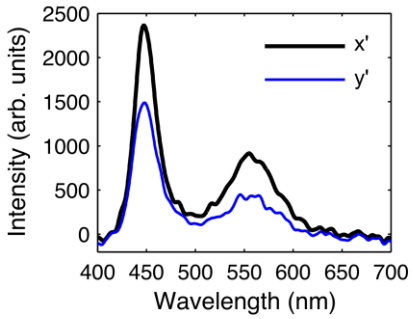

Figure 4.20. EL emission spectra with the polarizer aligned along $[1\bar{2}10]$ (x'-direction) and with the polarizer aligned along $[\bar{1}01\bar{4}]$ (y′-direction).

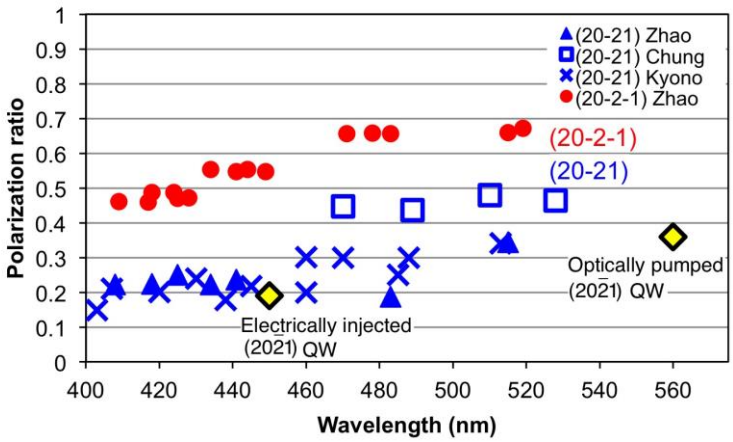

Figure 4.21. Optical polarization ratios as a function of the peak wavelengths of the dominant component for electrically injected InGaN QWs on $(20\bar{2}1)$ and $(20\bar{2}\bar{1})$ in blue and red, respectively. Yellow diamond points indicate the polarization ratios of the optically pumped yellow QWs and electrically injected blue QWs from the $(20\bar{2}1)$ tunnel junction device measured in Fig. 4.18.

Overall, the emission peaks in Fig. 4.19 are similar to the emission peaks from commercial phosphor converted LEDs for white light, which combine a blue LED pumping a yellow phosphor. The emission spectrum for a phosphor converted LED consists of a narrow blue peak, which is emission from the blue LED, and a broad yellow peak, which is emission from the phosphor. However, because the ratio of blue to yellow light is too high, the emission spectrum in Fig. 4.19 does not correspond to white light. As shown in the 1931 CIE *x*, *y* chromaticity diagram in Fig. 4.22, the emission spectrum in Fig. 4.19 corresponds to a point at (0.23, 0.21) and the lies at the end of the Planckian locus. By increasing the ratio of yellow to blue emission compared to the spectrum in Fig. 4.19, future devices can produce spatially uniform phosphor-free polarized white light.

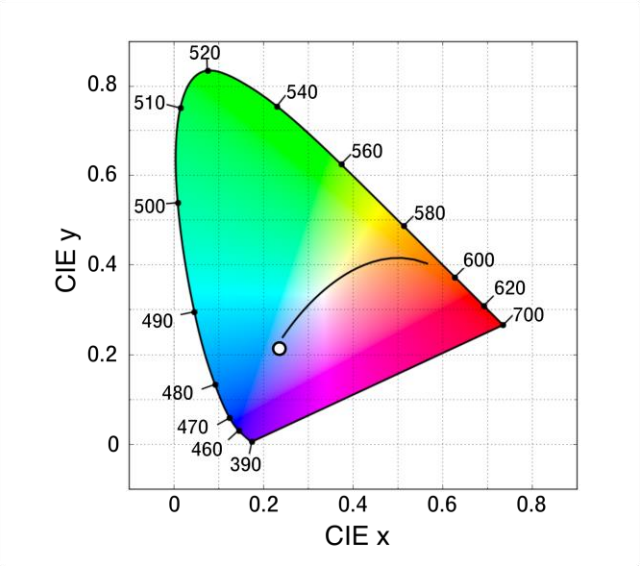

Figure 4.22. CIE *x*, *y* chromaticity diagram indicating the chromaticity coordinates corresponding to the spectrum in Fig. 4.19.

Polarized white light has important applications in, for example, liquid crystal displays (LCDs). Increasing the absorbance, radiative efficiency, and/or number of optically pumped QWs will increase the ratio of yellow to blue emission. Incorporating a dichroic coating with high blue reflectance and high yellow transmittance also will allow for control over the ratio of yellow to blue emission. Extraction engineering may also improve the efficiency of future devices. For example, a photonic crystal can increase extraction while preserving optical polarization. [23]

In summary, we have grown and fabricated a $(20\bar{2}1)$ III-nitrides device in which a tunnel junction is used to monolithically incorporate optically pumped QWs for long wavelength emission and an electrically injected blue LED, which is used as the excitation source for the optically pumped QWs. The use of a tunnel junction allows the optically pumped, high indium content InGaN QWs to be grown after the blue LED and to never be exposed to high growth temperatures, which have been shown to degrade high indium content InGaN. Use of NH_3 MBE enabled the growth of the tunnel junction in this device

demonstration, while use of MOCVD enabled the growth of InGaN with high radiative efficiency. [34], [35] Our initial device produced emission peaks at 450 nm from the electrically injected QWs and at 560 nm from optically pumped QWs. Optically polarized emission was measured, with a polarization ratio of 0.28. By increasing the ratio of yellow to blue emission, future devices can be used to produce phosphor-free polarized white light, which has important applications in, for example, LCDs.

References

[1] H. Masui, H. Yamada, K. Iso, S. Nakamura, and S. P. DenBaars, "Optical polarization characteristics of m -oriented InGaN/GaN light-emitting diodes with various indium compositions in single-quantum-well structure," *J. Phys. D. Appl. Phys.*, vol. 41, no. 22, p. 225104, Nov. 2008.

[2] S. J. Kowsz, C. D. Pynn, S. H. Oh, R. M. Farrell, J. S. Speck, S. P. DenBaars, and S. Nakamura, "Demonstration of phosphor-free polarized white light emission from monolithically integrated semipolar InGaN quantum wells," *Appl. Phys. Lett.*, vol. 107, no. 10, p. 101104, Sep. 2015.

[3] C.-C. Pan, S. Tanaka, F. Wu, Y. Zhao, J. S. Speck, S. Nakamura, S. P. DenBaars, and D. Feezell, "High-Power, Low-Efficiency-Droop Semipolar (20-2-1) Single-Quantum-Well Blue Light-Emitting Diodes," *Appl. Phys. Express*, vol. 5, no. 6, p. 062103, Jun. 2012.

[4] Y. Zhao, S. Tanaka, C.-C. Pan, K. Fujito, D. Feezell, J. S. Speck, S. P. DenBaars, and S. Nakamura, "High-Power Blue-Violet Semipolar (20-2-1) InGaN/GaN Light-Emitting Diodes with Low Efficiency Droop at 200 A/cm2," *Appl. Phys. Express*, vol. 4, no. 8, p. 082104, Jul. 2011.

[5] D. F. Feezell, J. S. Speck, S. P. DenBaars, and S. Nakamura, "Semipolar (20-2-1) InGaN/GaN Light-Emitting Diodes for High-Efficiency Solid-State Lighting," *J. Disp. Technol.*, vol. 9, no. 4, pp. 190–198, Apr. 2013.

[6] B. Van Daele, G. Van Tendeloo, K. Jacobs, I. Moerman, and M. R. Leys, "Formation of metallic in in InGaN/GaN multiquantum wells," *Appl. Phys. Lett.*, vol. 85, no. 19, pp. 4379–4381, 2004.

[7] M. T. Hardy, F. Wu, C.-Y. Huang, Y. Zhao, D. F. Feezell, S. Nakamura, J. S. Speck, and S. P. DenBaars, "Impact of p-GaN Thermal Damage and Barrier Composition on Semipolar Green Laser Diodes," *IEEE Photonics Technol. Lett.*, vol. 26, no. 1, pp. 43–46, Jan. 2014.

[8] Y. Kawaguchi, C. Huang, Y. Wu, Y. Zhao, S. P. DenBaars, and S. Nakamura, "Semipolar (20-21) Single-Quantum-Well Red Light-Emitting Diodes with a Low Forward Voltage," *Jpn. J. Appl. Phys.*, vol. 52, no. 8S, p. 08JC08, Aug. 2013.

[9] S. Yamamoto, Y. Zhao, C.-C. Pan, R. B. Chung, K. Fujito, J. Sonoda, S. P. DenBaars, and S. Nakamura, "High-Efficiency Single-Quantum-Well Green and Yellow-Green Light-Emitting Diodes on Semipolar (20-21) GaN Substrates," *Appl. Phys. Express*, vol. 3, no. 12, p. 122102, Nov. 2010.

[10] Y. Enya, Y. Yoshizumi, T. Kyono, K. Akita, M. Ueno, M. Adachi, T. Sumitomo, S. Tokuyama, T. Ikegami, K. Katayama, and T. Nakamura, "531 nm Green Lasing of InGaN Based Laser Diodes on Semi-Polar {20-21} Free-Standing GaN Substrates,"

Appl. Phys. Express, vol. 2, no. 8, p. 082101, Jul. 2009.

[11] F. Wu, Y. Zhao, A. Romanov, S. P. DenBaars, S. Nakamura, and J. S. Speck, "Stacking faults and interface roughening in semipolar (20-2-1) single InGaN quantum wells for long wavelength emission," *Appl. Phys. Lett.*, vol. 104, no. 15, p. 151901, Apr. 2014.

[12] J. Xu, X. Zhang, H. Yang, H. Guo, Y. Zheng, D. Zhou, and Y. Cui, "Enhancement of performance of GaN-based light-emitting diodes by insertion and optimization of n-InGaN / GaN composite current-spreading layers and optimization of n-InGaN / GaN composite current-spreading layers," vol. 022101.

[13] H. Y. Ryu and W. J. Choi, "Optimization of InGaN/GaN superlattice structures for high-efficiency vertical blue light-emitting diodes," *J. Appl. Phys.*, vol. 114, no. 17, 2013.

[14] R. B. Chung, Y.-D. Lin, I. Koslow, N. Pfaff, H. Ohta, J. Ha, S. P. DenBaars, and S. Nakamura, "Electroluminescence Characterization of (20-21) InGaN/GaN Light Emitting Diodes with Various Wavelengths," *Jpn. J. Appl. Phys.*, vol. 49, no. 7, p. 070203, Jul. 2010.

[15] Y. Zhao, S. Tanaka, Q. Yan, C.-Y. Huang, R. B. Chung, C.-C. Pan, K. Fujito, D. Feezell, C. G. Van de Walle, J. S. Speck, S. P. DenBaars, and S. Nakamura, "High optical polarization ratio from semipolar (20-2-1) blue-green InGaN/GaN light-emitting diodes," *Appl. Phys. Lett.*, vol. 99, no. 5, p. 051109, 2011.

[16] S. Marcinkevičius, R. Ivanov, Y. Zhao, S. Nakamura, S. P. DenBaars, and J. S. Speck, "Highly polarized photoluminescence and its dynamics in semipolar (20-2-1) InGaN/GaN quantum well," *Appl. Phys. Lett.*, vol. 104, no. 11, p. 111113, Mar. 2014.

[17] T. Kyono, Y. Yoshizumi, Y. Enya, M. Adachi, S. Tokuyama, M. Ueno, K. Katayama, and T. Nakamura, "Optical Polarization Characteristics of InGaN Quantum Wells for Green Laser Diodes on Semi-Polar (20-21) GaN Substrates," *Appl. Phys. Express*, vol. 3, no. 1, p. 011003, Jan. 2010.

[18] Y. Zhao, Q. Yan, D. Feezell, K. Fujito, C. G. Van de Walle, J. S. Speck, S. P. DenBaars, and S. Nakamura, "Optical polarization characteristics of semipolar (30-31) and (30-3-1) InGaN/GaN light-emitting diodes," *Opt. Express*, vol. 21, no. S1, p. A53, Jan. 2013.

[19] M. Kubota, K. Okamoto, T. Tanaka, and H. Ohta, "Temperature dependence of polarized photoluminescence from nonpolar m-plane InGaN multiple quantum wells for blue laser diodes," *Appl. Phys. Lett.*, vol. 92, no. 1, p. 011920, 2008.

[20] S. You, T. Detchprohm, M. Zhu, W. Hou, E. a. Preble, D. Hanser, T. Paskova, and C. Wetzel, "Highly Polarized Green Light Emitting Diode in m-Axis GaInN/GaN," *Appl. Phys. Express*, vol. 3, no. 10, p. 102103, Oct. 2010.

[21] A. E. Romanov, E. C. Young, F. Wu, A. Tyagi, C. S. Gallinat, S. Nakamura, S. P. DenBaars, and J. S. Speck, "Basal plane misfit dislocations and stress relaxation in III-nitride semipolar heteroepitaxy," *J. Appl. Phys.*, vol. 109, no. 10, p. 103522, 2011.

[22] R. Shivaraman, Y. Kawaguchi, S. Tanaka, S. P. DenBaars, S. Nakamura, and J. S. Speck, "Comparative analysis of (20-21) and (20-2-1) semipolar GaN light emitting diodes using atom probe tomography," *Appl. Phys. Lett.*, vol. 102, no. 25, p. 251104, 2013.

[23] E. Matioli, S. Brinkley, K. M. Kelchner, Y.-L. Hu, S. Nakamura, S. DenBaars, J. Speck, and C. Weisbuch, "High-brightness polarized light-emitting diodes," *Light Sci. Appl.*, vol. 1, no. 8, p. e22, Aug. 2012.

[24] A. E. Romanov, T. J. Baker, S. Nakamura, and J. S. Speck, "Strain-induced polarization in wurtzite III-nitride semipolar layers," *J. Appl. Phys.*, vol. 100, no. 2, p. 023522, 2006.

[25] P. S. Hsu, K. M. Kelchner, A. Tyagi, R. M. Farrell, D. a. Haeger, K. Fujito, H. Ohta, S. P. DenBaars, J. S. Speck, and S. Nakamura, "InGaN/GaN Blue Laser Diode Grown on Semipolar (30\bar31) Free-Standing GaN Substrates," *Appl. Phys. Express*, vol. 3, no. 5, p. 052702, Apr. 2010.

[26] H. Shen, M. Wraback, H. Zhong, A. Tyagi, S. P. DenBaars, S. Nakamura, and J. S. Speck, "Determination of polarization field in a semipolar (11-22) InGaN⁄GaN single quantum well using Franz–Keldysh oscillations in electroreflectance," *Appl. Phys. Lett.*, vol. 94, no. 24, p. 241906, 2009.

[27] M. V. Bogdanov, K. a. Bulashevich, I. Y. Evstratov, and S. Y. Karpov, "Coupled Modeling of Current Spreading, Thermal Effects, and Light Extraction in Ill-Nitride Light-Emitting Diodes," in *2007 International Conference on Numerical Simulation of Optoelectronic Devices*, 2007, vol. 125023, pp. 23–24.

[28] Y.-N. Xu and W. Y. Ching, "Electronic, optical, and structural properties of some wurtzite crystals," *Phys. Rev. B*, vol. 48, no. 7, pp. 4335–4351, Aug. 1993.

[29] I. Vurgaftman, J. R. Meyer, and L. R. Ram-Mohan, "Band parameters for III–V compound semiconductors and their alloys," *J. Appl. Phys.*, vol. 89, no. 11, p. 5815, 2001.

[30] I. L. Koslow, M. T. Hardy, P. Shan Hsu, P.-Y. Dang, F. Wu, A. Romanov, Y.-R. Wu, E. C. Young, S. Nakamura, J. S. Speck, and S. P. DenBaars, "Performance and polarization effects in (11-22) long wavelength light emitting diodes grown on stress relaxed InGaN buffer layers," *Appl. Phys. Lett.*, vol. 101, no. 12, p. 121106, 2012.

[31] Y. Koide, H. Ishikawa, S. Kobayashi, S. Yamasaki, S. Nagai, J. Umezaki, M. Koike, and M. Murakami, "Dependence of electrical properties on work functions of metals contacting to p-type GaN," *Appl. Surf. Sci.*, vol. 117–118, no. 3, pp. 373–379, Jun. 1997.

[32] Q. Z. Liu and S. S. Lau, “A review of the metal–GaN contact technology,” *Solid. State. Electron.*, vol. 42, no. 5, pp. 677–691, May 1998.

[33] J. T. Leonard, E. C. Young, B. P. Yonkee, D. a. Cohen, T. Margalith, S. P. DenBaars, J. S. Speck, and S. Nakamura, “Demonstration of a III-nitride vertical-cavity surface-emitting laser with a III-nitride tunnel junction intracavity contact,” *Appl. Phys. Lett.*, vol. 107, no. 9, p. 091105, Aug. 2015.

[34] M. Malinverni, D. Martin, and N. Grandjean, “InGaN based micro light emitting diodes featuring a buried GaN tunnel junction,” *Appl. Phys. Lett.*, vol. 107, no. 5, p. 051107, Aug. 2015.

[35] E. C. Young, B. P. Yonkee, F. Wu, S. H. Oh, S. P. DenBaars, S. Nakamura, and J. S. Speck, “Hybrid tunnel junction contacts to III–nitride light-emitting diodes,” *Appl. Phys. Express*, vol. 9, no. 2, p. 022102, Feb. 2016.

[36] B. P. Yonkee, E. C. Young, C. Lee, J. T. Leonard, S. P. DenBaars, J. S. Speck, and S. Nakamura, “Demonstration of a III-nitride edge-emitting laser diode utilizing a GaN tunnel junction contact,” *Opt. Express*, vol. 24, no. 7, p. 7816, Apr. 2016.

[37] A. M. Fischer, Z. Wu, K. Sun, Q. Wei, Y. Huang, R. Senda, D. Iida, M. Iwaya, H. Amano, and F. A. Ponce, “Misfit Strain Relaxation by Stacking Fault Generation in InGaN Quantum Wells Grown on m -Plane GaN,” *Appl. Phys. Express*, vol. 2, no. 4, p. 041002, Apr. 2009.

Chapter 5

Conclusion and Future Work

5.1 Demonstration of Semipolar Devices for Polarized White Light

In conclusion, we have grown and fabricated a novel device design and demonstrated polarized white light emission. By monolithically integrating a blue light-emitting diode (LED) grown on the $(20\bar{2}\bar{1})$ face of a bulk GaN substrate with optically pumped high indium content InGaN quantum wells (QWs) for yellow emission subsequently grown on the $(20\bar{2}1)$ face, emission peaks were observed at 440 nm and 560 nm. Emission with *Commission Internationale de l'Eclairage* (CIE) *x*- and *y*-chromaticity coordinates of (0.28, 0.29) was reported with an optical polarization ratio of 0.40. [1] This initial demonstration illustrates the potential of monolithic electrically injected and optically pumped devices for polarized white light emission, which has important applications in, for example, LED backlighting for LCDs.

We have also grown and fabricated a polarized white light-emitting device that monolithically integrates a blue LED grown on the $(20\bar{2}\bar{1})$ face of a bulk GaN substrate with optically pumped high indium content InGaN QWs for long wavelength emission grown on the $(20\bar{2}1)$ face, where the doping profile was intentionally engineered to red-shift the emission of one of the optically pumped QWs by creating a built-in electric field in the QW that acted in the same direction as the polarization-induced electric field. Emission

peaks were observed at 450 nm from the electrically injected QW and at 520 nm and 590 nm from the optically pumped QWs, which were grown in *n*-*i*-*n* and *p*-*i*-*n* structures, respectively. Modeling work supported that band engineering red-shifted the emission from the QW in the *p*-*i*-*n* structure more significantly than the red-shift attributed to the change in InGaN alloy composition produced by the QW in the *p*-*i*-*n* structure being grown 10 °C colder than the QW in the *n*-*i*-*n* structure. Emission with CIE *x*- and *y*-chromaticity coordinates of (0.33, 0.35) and an optical polarization ratio of 0.30 was reported. This monolithic electrically injected and optically pumped device produced polarized white light with an emission spectrum that would be desirable for either general illumination or display technology.

Finally, we have grown and fabricated a $(20\bar{2}1)$ III-nitrides device in which a tunnel junction is used to monolithically incorporate optically pumped QWs for long wavelength emission and an electrically injected blue LED, which is used as the excitation source for the optically pumped QWs. The use of a tunnel junction allows the optically pumped, high indium content InGaN QWs to be grown after the blue LED and to never be exposed to high growth temperatures, which have been shown to degrade high indium content InGaN. Use of NH_3 MBE enabled the growth of the tunnel junction in this device demonstration, while use of MOCVD enabled the growth of InGaN with high radiative efficiency. Our initial device produced emission peaks at 450 nm from the electrically injected QWs and at 560 nm from optically pumped QWs. Optically polarized emission was measured, with a polarization ratio of 0.28. By increasing the ratio of yellow to blue emission, future devices can be used to produce phosphor-free polarized white light.

5.2 Future Work

In the semipolar devices for polarized white light that we have demonstrated, color tuning was a result of non-uniform emission across the sample. Therefore, ongoing work is focused on increasing the intensity of the long wavelength emission from the optically pumped QWs relative to the blue emission from the LED in order to achieve spatially uniform white light emission. The color uniformity can be improved by increasing the yellow emission from the optically pumped QWs and/or reducing the amount of blue light that is extracted. The goal of achieving spatially uniform white light emission can be addressed by optimizing device design, growth conditions, and/or extraction engineering.

These initial devices could also be improved by increasing their efficiencies. At this time, the efficiencies of these devices have not been measured because quantifying efficiencies requires the devices to be measured in an integrating sphere, where all the emitted light is collected. A single device mounted on header with spatially uniform white light emission is appropriate for measuring in the integrating sphere. Therefore, achieving a device with uniform white light emission is also a priority so that efficiency can be measured and used as a metric in improving device performance. After achieving devices with uniform white light emission, device design, growth conditions, and/or extraction engineering can contribute to improving efficiency.

5.2.1 Device Design and Growth Conditions

One way to realize devices with uniform white light emission is to increase long wavelength emission from the optically pumped QWs by increasing the radiative efficiency of the optically pumped QWs. In addition to enabling uniform white light emission,

increasing radiative efficiency also would increase the efficiency of the device. The radiative efficiency of the optically pumped QWs can be increased by optimizing the growth conditions of the QWs. The growth of high indium content InGaN for long wavelength emission requires low growth temperatures to prevent desorption of indium from the surface. However, low growth temperatures can result in increased point defects and growth errors. Growth temperature, growth rate, and the ratio of the indium to gallium precursors can be optimized to realize improvements in the crystal quality of the high indium content InGaN QWs. The radiative efficiency of the optically pumped QWs can also be increased by increasing the overlap of the electron and hole wave functions. As discussed in Section 3.5, there is room for future work investigating the use of thinner and/or lower indium content InGaN QWs in which long wavelength emission is enabled by band engineering. Although simulation work can examine the effect band engineering has on wavefunction overlap, growing thinner and/or lower indium content InGaN QWs may also influence defect formation and, as a result, nonradiative recombination. Therefore, experimental work is necessary to explore whether thinner and/or low indium content InGaN QWs with band engineering can produce increased PL emission intensity at long emission wavelengths.

The initial devices could also be improved by increasing the absorption of blue light by the optically pumped QWs to convert more blue light to long wavelength emission, thus enabling uniform white light emission. This would serve both to increase the long wavelength emission and decrease the amount of blue light that is extracted. Increasing the absorption of the optically pumped QWs can be achieved by growing more optically pumped QWs and/or by increasing the overlap of the electron and hole wave functions. Again, as discussed in Section 3.5, band engineering enables the use of thinner and/or low

indium content InGaN QWs for long wavelength emission. In addition to impacting radiative efficiency, QW thickness and InGaN indium content will similarly affect absorption. Additionally, if thinner and/or lower indium content InGaN QWs can be used for long wavelength emission and do not produce nonradiative defects in the QWs like those discussed in Chapter 3, then band engineering may also enable growth of a greater number of QWs.

Overall, the fabrication of these devices has not been optimized, and the efficiency of devices will benefit from optimized ohmic contacts with high reflectivity. Epitaxial device designs may also incorporate highly doped layers to which contact is made. Improved contacts will increase efficiency by decreasing light absorbed in the contacts as well as by decreasing operating voltages.

In addition to improving the fabrication process, tunnel junction devices can be improved by further optimizing the tunnel junction growth and growth of optically pumped QWs above tunnel junction. Variables of interest include: activation procedure, surface treatments prior to tunnel junction growth and prior to growth of optically pumped QWs, growth conditions for the tunnel junction and the optically pumped QWs, and capping layer above the tunnel junction. Overall, it would be preferred to grow the tunnel junction by metalorganic chemical vapor deposition (MOCVD), as this would simplify the growth process. Growth of tunnel junctions by MOCVD remains an area for future work.

5.2.2 Extraction Engineering

The semipolar devices for polarized white light that we have demonstrated are double-side polished devices and, thus, have low extraction efficiency. Intentionally

engineering extraction can enable uniform white light emission and improve efficiency. Additionally, extraction engineering will be required to achieve optically polarized emission from singulated devices because emission directed towards the sidewalls is expected not to have the desired polarization. In particular, incorporating a photonic crystal and reflective coatings can affect extraction for improved devices.

Incorporating a photonic crystal can improve the extraction efficiency of this device while preserving the optical polarization ratio is also an area for future work. The extraction efficiency of LEDs typically is increased by surface roughening, but scattering results in a loss of optical polarization. In this case, one way to increase the extraction efficiency is to incorporate a photonic crystal, which has been experimentally demonstrated on *m*-plane to increase extraction efficiency while maintaining optical polarization. [2]

Incorporating a dichroic mirror with high blue reflectance and high transmittance of long visible wavelengths is a technique by which extraction engineering can enable uniform white light emission. A dichroic mirror would reflect blue light for additional passes, thus increasing the probability of absorption by the optically pumped QWs. This is especially important because growing multiple QW (MQW) stacks with large numbers of optically pumped QWs for long wavelength emission remains a challenge. Dichroic mirrors enable uniform white light emission using fewer QWs. Even if nonradiative defects in the QWs, which were discussed in Chapter 3, can be suppressed, MQW stacks may remain a challenge because the first high indium content InGaN QWs in a MQW stack first may suffer from decreased radiative efficiency compared to QWs grown later in a MQW stack because the first QWs have been held at elevated temperature. The effect of thermal damage due to QWs being held at growth temperature for too long of a time may limit the number of optically

pumped QWs for long wavelength emission. In this case, dichroic mirrors may be necessary for efficient and uniform white light emission.

Optical coatings can be accurately simulated, and the design requirements for dichroic mirrors for these devices are achievable. Table 5.1 shows an example of an eight period SiO_2/Ta_2O_5 coating designed for high reflectance of blue light between 420 nm and 460 nm and high transmittance of long wavelength emission between 530 nm and 590 nm. SiO_2 and Ta_2O_5 are commonly deposited by ion beam deposition for laser facet coatings and have been well characterized. Figure 5.1 shows the simulated reflectance for the dichroic mirror stack defined in Table 5.1. The blue line shows reflectance for normal incidence light, and the red line shows cone average reflectance for light with angles of incidence between 0° and 25°. The simulation was performed with the software package TFCalc.

TABLE 5.1. Example of dichroic mirror coating designed for high reflectance between 420 nm and 460 nm and high transmittance between 530 nm and 590 nm.

Material	*Thickness (nm)*
Air	
Ta_2O_5	17.76
SiO_2	83.45
Ta_2O_5	65.08
SiO_2	71.71
Ta_2O_5	60.45
SiO_2	55.06
Ta_2O_5	62.13
SiO_2	69.64
Ta_2O_5	61.26
SiO_2	63.09
Ta_2O_5	60.45
SiO_2	68.05
Ta_2O_5	53.49
SiO_2	93.53
Ta_2O_5	34.12
SiO_2	58.21
GaN	

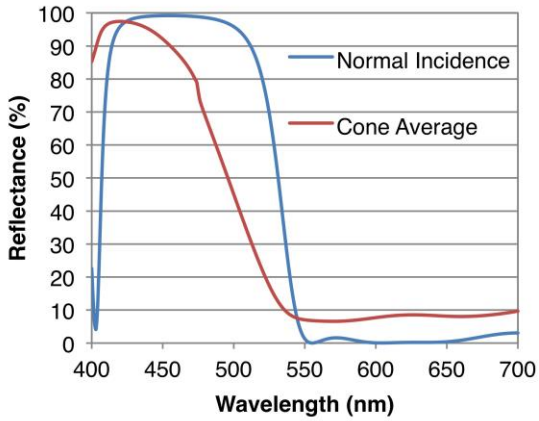

Figure 5.1. TFCalc simulated reflectance for the dichroic mirror stack defined in Table 5.1. Blue line shows reflectance for normal incidence light, and red line shows cone average reflectance for light with angles of incidence between 0° and 25°.

Lastly, sidewall emission presents an additional complication that will need to be addressed in future work for efficient devices with polarized white light emission. The design of a device measured in the integrating sphere needs to consider sidewall emission, which may not have the desired polarization or the same ratio of blue to long wavelength emission as light extracted from the top surface of the device. There are many factors to consider regarding sidewall emission. First, light produced by recombination of electrons and holes in the second valence is directed towards the sidewalls and polarized with the electric field perpendicular to the *a*-direction. Second, singulating devices by dicing produces rough sidewalls will scatter light. Third, due to the geometry of singulated devices, a significant amount of blue light from the LED may reach the sidewalls without ever having passed through the optically pumped QWs. Likely blue light emitted by the LED will need to be reflected back from the sidewalls in order to increase the probability that it is absorbed by the optically pumped QWs. Overall, future work will be required to measure the contribution of sidewall emission, and after better understanding sidewall emission,

appropriate optical coatings can be designed to reflect, absorb, or transmit light directed towards the sidewalls of the device.

References

[1] S. J. Kowsz, C. D. Pynn, S. H. Oh, R. M. Farrell, J. S. Speck, S. P. DenBaars, and S. Nakamura, "Demonstration of phosphor-free polarized white light emission from monolithically integrated semipolar InGaN quantum wells," *Appl. Phys. Lett.*, vol. 107, no. 10, p. 101104, Sep. 2015.

[2] E. Matioli, S. Brinkley, K. M. Kelchner, Y.-L. Hu, S. Nakamura, S. DenBaars, J. Speck, and C. Weisbuch, "High-brightness polarized light-emitting diodes," *Light Sci. Appl.*, vol. 1, no. 8, p. e22, Aug. 2012.

Appendix A

SiLENSe Simulations of Optically Pumped Quantum Wells

A.1 Simulation Inputs

Typically our group uses SiLENSe for simulating devices under electric injection. SiLENSe can simulate photoluminescence (PL). This requires inputs for the absorption coefficient of GaN and InN, as well as an excitation wavelength and excitation power density. The values that we used for variables relevant to the PL simulations are given in Table A.1. For an example, if we consider a 450 nm light-emitting diode (LED) with 90% internal quantum efficiency operating at 20 A/cm^2, we calculate the density of total output power of 6.5 W/cm^2, according to:

$$\frac{20\ A}{cm^2}\frac{C/s}{A}\frac{6.242\times10^{18}\ electrons}{C}\frac{0.9\ photons}{electrons}\frac{450\ nm}{photon}\frac{eV}{1240\ nm}\frac{1.602\times10^{-19}\ J}{eV}$$

This calculation is only meant to give an estimate of a power density that can be used as an input for the model. Determining the actual power density is more complicated. For example, some light will escape from the chip or be absorbed before passing through the optically pumped QWs.

TABLE A.1. Variables used for SiLENSe PL simulations. (InN absorption coefficient from Refs. [1]–[3].)

Variable	*Input*
Absorption coefficient GaN (1/cm)	1
Absorption coefficient InN (1/cm)	10^5
Excitation wavelength (nm)	450
Excitation direction	From bottom (*n*-side)
Top (*p*-side) mirror reflectivity	0.8
Bottom (*n*-side) mirror reflectivity	0.8
Excitation power (W/cm^2)	Between 0.1 and 100

Table A.2 gives values for materials parameters that we used in our SiLENSe simulations. This table only reports materials properties for which the input was changed from the values specified by SiLENSe for InN and GaN. This work changed the values given by SiLENSe for the effective masses and splitting parameters to the values reported in Table A.2 (which were also reported in Table 4.1). The materials parameters provided by SiLENSe did not produce the valence band splitting that is expected and has been reported previously in theoretical and experimental literature. Changing the effective masses and splitting parameters produced results with reasonable valence band splitting, which is reflected, for example, in the calculated bound states reported in Table 4.2.

TABLE A.2. III-nitride materials properties used for SiLENSe simulations. Data for effective masses are taken from Ref. [4]. Data for splitting parameters are taken from Ref. [5].

Material property	*InN*	*GaN*
Electron effective mass (m_0)	0.1	0.2
Heavy hole effective mass (m_0)	1.63	1.4
Light hole effective mass (m_0)	0.27	0.3
Split-off hole effective mass (m_0)	0.65	0.6
Crystal-field splitting (meV)	1	14
Spin-orbit splitting (meV)	41	19

Although SiLENSe can simulate PL emission spectra, we have several concerns about the accuracy of these simulations because the calculation makes several simplifying

assumptions and because we are not confident in several of the inputs required for the calculations, including: the Shockley-Read-Hall coefficient, the absorption coefficients, and the excitation power density. However, these inputs about which we are less certain do not significantly affect calculations of bound states or the band diagram. In particular, we are unsure of the Shockley-Read-Hall A coefficient for the optically pumped QWs. We expect that the A coefficient for the optically pumped QWs with long wavelength emission may be higher than the value assumed for blue QWs due to the challenges in achieving high indium content InGaN QWs. Because we do not have an accurate estimate of the A coefficient for our QWs, we did not change this value. We are also not confident in the absorption coefficients given for GaN and InN, which are difficult to measure and may be different for our material as compared to literature. As discussed above, the excitation power density is also not accurately known. Lastly, SiLENSe does not consider alloy fluctuations, which are important in considering optically pumped QWs with long wavelength emission. [6], [7] Alloy fluctuations are particularly significant for high indium content InGaN that is required for long wavelength emission and for low carrier densities, which are relevant for optically pumped QWs.

References

[1] Q. Guo and A. Yoshida, “Temperature Dependence of Band Gap Change in InN and AlN,” *Jpn. J. Appl. Phys.*, vol. 33, no. Part 1, No. 5A, pp. 2453–2456, May 1994.

[2] J. W. Trainor and K. Rose, “Some properties of InN films prepared by reactive evaporation,” *J. Electron. Mater.*, vol. 3, no. 4, pp. 821–828, Nov. 1974.

[3] N. Puychevrier and M. Menoret, “Synthesis of III–V semiconductor nitrides by reactive cathodic sputtering,” *Thin Solid Films*, vol. 36, no. 1, pp. 141–145, Jul. 1976.

[4] Y.-N. Xu and W. Y. Ching, “Electronic, optical, and structural properties of some wurtzite crystals,” *Phys. Rev. B*, vol. 48, no. 7, pp. 4335–4351, Aug. 1993.

[5] I. Vurgaftman, J. R. Meyer, and L. R. Ram-Mohan, “Band parameters for III–V compound semiconductors and their alloys,” *J. Appl. Phys.*, vol. 89, no. 11, p. 5815, 2001.

[6] P. M. McBride, Q. Yan, and C. G. Van de Walle, “Effects of In profile on simulations of InGaN/GaN multi-quantum-well light-emitting diodes,” *Appl. Phys. Lett.*, vol. 105, no. 8, p. 083507, Aug. 2014.

[7] D. A. Browne, B. Mazumder, Y.-R. Wu, and J. S. Speck, “Electron transport in unipolar InGaN/GaN multiple quantum well structures grown by NH3 molecular beam epitaxy,” *J. Appl. Phys.*, vol. 117, no. 18, p. 185703, May 2015.

Appendix B

Optical Fiber Alignment on the Confocal Microscope

B.1 Optical Fiber Alignment Procedure

As shown in Fig. 4.1, the optical fiber needs to be aligned such that it is at the focal point of the confocal lens. The optical cable on the microscope has a 50 μm core and can be seen in Fig. B.1, where it is the blue cable emerging from the top port of the microscope. The optical cable on the microscope transmits light to a spectrometer. In order to align the optical fiber on the microscope, we used another optical fiber with a 50 μm core, which is the orange cable that can be seen in Fig. B.1. One end of the orange optical cable used for alignment was positioned below the objective lens and pointing directly up, to the best of our ability. The other end of the orange optical cable used for alignment was positioned under a lamp so that light shines through the cable.

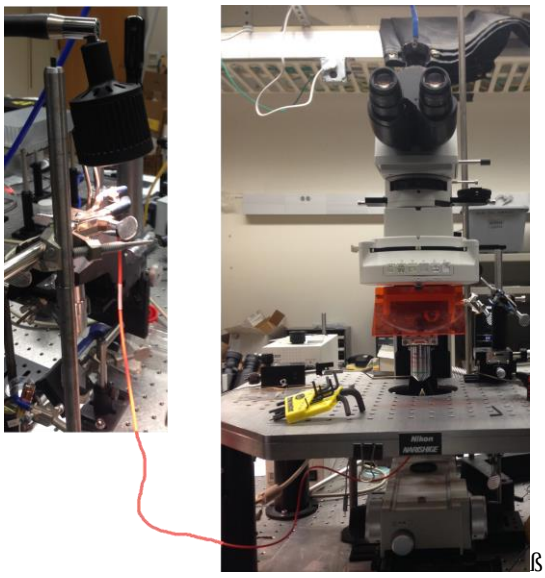

Figure B.1. Set-up for optical fiber alignment on the confocal microscope. The blue optical cable attached at the top port of the microscope needs to be aligned to the focal point of the confocal lens. The orange optical cable positioned below the objective lens is used for alignment. The other end of the orange optical cable is positioned below a lamp such that light shines into the optical fiber.

Looking through the microscope, the end of the orange optical fiber was brought into focus and centered in the field of view. Next the position of the blue optical fiber on the microscope was adjusted until the spectrometer counts were maximized. The *x* and *y* position of optical fiber was adjusted using adjustment screws, which are shown Fig. B.2. The *z* position of optical fiber could be adjusted by adding or subtracting spacers, which are also shown Fig. B.2. (At first, it was helpful to remove the optical cable positioner piece from the microscope in order to look at where the light was using a piece of paper held above the port. By adjusting the *x* and *y* position screws, the spot of light could be approximately centered.)

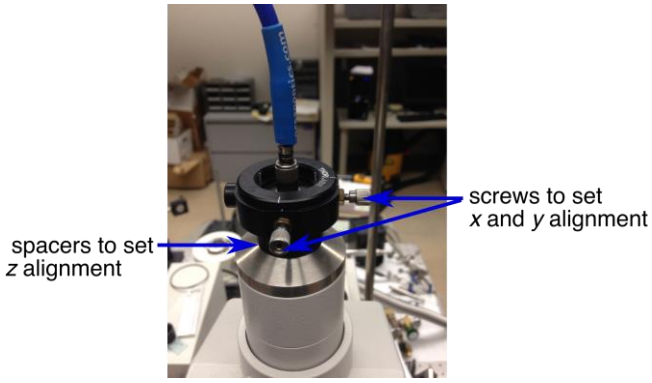

Figure B.2. Photograph of the blue optical cable connected to the top port of the microscope. Adjustment screws are used to set the *x* and *y* alignment. Spacers are used to set the *z* alignment.

The optical fiber was aligned to the focal point of the confocal lens for the system with use of the 20× objective lens. However, this position of the optical fiber did not result in correct alignment when changing to use the other objective lens on the microscope. Additionally, when the system is set up to use the 20× objective lens, the objective can move around to some degree. In order for the measurement location to be aligned with what is seen in the center of the field of view, the objective lens must be in the same location as it was for the alignment procedure. It is important to pay attention to this and, for example, push the objective lens as far back and the left as possible every time it is used.